

---

# Accelerating LLM Pre-Training through Flat-Direction Dynamics Enhancement

---

Shuchen Zhu<sup>\*1</sup> Rizhen Hu<sup>\*1</sup> Mingze Wang<sup>§1</sup> Mou Sun<sup>2</sup> Xue Wang<sup>3</sup> Kun Yuan<sup>†1</sup> Zaiwen Wen<sup>1</sup>

## Abstract

Pre-training Large Language Models requires immense computational resources, making optimizer efficiency essential. The optimization landscape is highly anisotropic, with loss reduction driven predominantly by progress along flat directions. While matrix-based optimizers such as Muon and SOAP leverage fine-grained curvature information to outperform AdamW, their updates tend toward isotropy—relatively conservative along flat directions yet potentially aggressive along sharp ones. To address this limitation, we first establish a unified Riemannian Ordinary Differential Equation (ODE) framework that elucidates how common adaptive algorithms operate synergistically: the preconditioner induces a Riemannian geometry that mitigates ill-conditioning, while momentum serves as a Riemannian damping term that promotes convergence. Guided by these insights, we propose **LITE**, a generalized acceleration strategy that enhances training dynamics by applying larger Hessian damping coefficients and learning rates along flat trajectories. Extensive experiments demonstrate that LITE significantly accelerates both Muon and SOAP across diverse architectures (Dense, MoE), parameter scales (130M–1.3B), datasets (C4, Pile), and learning-rate schedules (cosine, warmup-stable-decay). Theoretical analysis confirms that LITE facilitates faster convergence along flat directions in anisotropic landscapes, providing a principled approach to efficient LLM pre-training. The code is available at <https://github.com/SHUCHENZHU/LITE>.

## 1. Introduction

Large language models (LLMs) have revolutionized artificial intelligence with exceptional capabilities, yet the pre-

<sup>\*</sup>Equal contribution <sup>§</sup>Project lead <sup>1</sup>Peking University <sup>2</sup>Zhejiang Lab, Zhejiang <sup>3</sup>Meituan, Beijing. <sup>†</sup>Correspondence to: Kun Yuan <kunyan@pku.edu.cn>.

Preprint. February 27, 2026.

training procedure is computationally intensive due to massive model and data scales. Improving pre-training efficiency is essential for continued scaling, and the optimizer choice is crucial. Currently, AdamW (Kingma & Ba, 2014; Loshchilov & Hutter, 2017) serves as the standard in most LLM pre-training pipelines, favored for its simplicity and efficiency. However, it uses coordinate-wise scaling, which acts as a diagonal preconditioner and ignores parameter correlations within the Hessian, limiting the ability to navigate complex optimization landscapes.

To address the limitation of the diagonal preconditioning, algorithms like Shampoo (Gupta et al., 2018; Shi et al., 2023) and KFAC (Martens & Grosse, 2015) introduce matrix-based preconditioners to capture richer geometric structures, demonstrating superior convergence over AdamW in traditional deep learning tasks. Advancing this paradigm to the scale of LLM pre-training, a new wave of matrix-based optimizers, such as Muon (Jordan et al., 2024) and SOAP (Vyas et al., 2025), has emerged, achieving significant performance gains over AdamW. Notably, Muon has already achieved validated success in industrial-scale training scenarios (Liu et al., 2025a; Team, 2025). These methods signify a paradigm shift towards exploiting matrix-level curvature information to accelerate convergence.

Despite the empirical success of these advanced optimizers, significant limitations remain:

- 1. Preconditioner-induced isotropic update magnitudes.** Although adaptive methods correct descent directions by effective preconditioners, prior studies (Staib et al., 2019; Zhou et al., 2020; Liu et al., 2025a; Lu et al., 2025; Wang et al., 2025b) suggest that the *update magnitudes* often tend towards *isotropic*, i.e., of comparable scale across different Hessian eigen-directions. This behavior is sub-optimal in the ill-conditioned landscape, which is too cautious along flat directions while potentially aggressive along sharp ones.
- 2. Inadequate momentum mechanisms for non-convexity.** Constrained by the simple linear nature of Exponential Moving Average (EMA), which inherently imposes an isotropic damping effect, existing momentum schemes inadequately exploit second-order information, leaving them susceptible to ill-conditioned curvature. While tech-

niques like Nesterov acceleration implicitly incorporates Hessian-driven damping (Shi et al., 2021), the design is largely inherited from convex optimization paradigms, rendering them insufficient for effectively accelerating convergence along non-convex directions.

Addressing these limitations, however, presents a fundamental challenge: the lack of a unified theoretical framework that provides a comprehensive understanding of *how preconditioning and momentum jointly influence training dynamics in anisotropic loss landscapes*. Such a framework remains elusive, as current analyses typically treat these components in isolation, failing to elucidate their synergistic mechanisms in non-convex optimization. Bridging this theoretical gap is essential for designing superior optimizers that can simultaneously rectify update magnitudes and leverage curvature-aware momentum. These issues motivate the following questions:

- Can we establish a unified theoretical understanding of the synergistic roles of the momentum and preconditioner in adaptive optimization algorithms?
- Leveraging this foundation, how can we rectify the inadequate isotropic update and refine the momentum mechanism to achieve superior efficiency in pre-training LLMs?

**Our contributions** are as follows:

- We propose a **unified Riemannian ODE framework** that encapsulates prevalent adaptive optimizers for LLM pre-training (e.g. AdamW, Lion, Muon, SOAP) as well as their Nesterov-accelerated counterparts. This framework elucidates the synergistic mechanism between preconditioning and momentum from a continuous time manifold optimization perspective: the preconditioner induces a Riemannian geometry that mitigates the landscape’s ill-conditioning, while momentum functions as a *Riemannian damping* to foster optimization within this metric.
- Building on this framework, we propose **LITE**, a generalized strategy for accelerating adaptive optimizers in LLM pre-training. Leveraging our ODE analysis, LITE applies *larger Hessian damping coefficients and learning rates in the flat directions*, which enhances momentum accumulation and amplifies update magnitudes therein. This approach is designed to **accelerate training dynamics along the flat directions** that dominate loss reduction within the ill-conditioned landscape, thereby enhancing the pre-training performance.
- We conduct **extensive empirical evaluations** on the acceleration performance of LITE across diverse LLM pre-training settings, spanning different base optimizers (Muon and SOAP), model architectures (LLaMA and

QwenMoE), datasets (C4 and Pile), and learning rate schedules (cosine and warmup-stable-decay), with model sizes ranging from 0.13B to 1.3B parameters. Our results demonstrate that LITE-accelerated optimizers achieve remarkable loss reductions and exhibit more favorable scaling laws over standard baselines, notably attaining a  $2\times$  speedup in long-horizon training (Figure 1). This indicates the potential of LITE for superior scalability to larger models and extended token budgets.

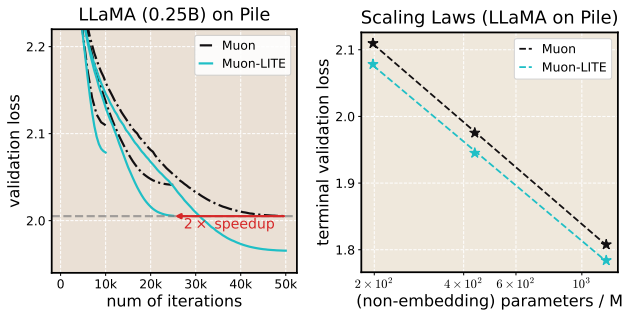


Figure 1. MUON-LITE exhibits superior scaling behavior across varying token budgets (left) and model sizes (right) compared to Muon.

- We provide a **theoretical analysis** of the training dynamics of LITE within anisotropic landscapes, showing that it boosts dynamics in flat directions and facilitates optimization, thereby supporting our design intuition.

## 2. Related Work

**Accelerated Optimizers for LLM pre-training.** Adaptive optimizers serve as the cornerstone of modern LLM pre-training. One stream of research focuses on refining the preconditioner: moving beyond simple element-wise scaling of AdamW (Loshchilov & Hutter, 2017), methods like (Liu et al., 2024; Wang et al., 2025a) incorporate explicit curvature estimation, while matrix-based approaches (Jordan et al., 2024; Vyas et al., 2025; Pethick et al., 2025; Liu et al., 2025b; Lau et al., 2026) leverage richer geometric structures to better approximate the curvature. Complementing these geometric improvements are refinements to the momentum mechanism, spanning multi-timescale momentum (Pagliardini et al., 2025), Nesterov-type acceleration (Xie et al., 2024; Yuan et al., 2025), and various momentum correction schemes (Huang et al., 2025; Liang et al., 2025).

**Training Dynamics and Loss Landscape in Deep Learning.** Prior studies (Ghorbani et al., 2019; Yao et al., 2020; Zhang et al., 2024; Su, 2025) elucidate the *ill-conditioned and anisotropic* nature of the deep learning loss landscape. Specifically, the Hessian spectrum is dominated by a massive bulk of near-zero and negative eigenvalues (referred to as *flat directions*), while the large positive eigenvalues

are significantly greater in magnitude but sparse in number (referred to as *sharp directions*), as schematically illustrated in Figure 2 (left). Recent investigations (Song et al., 2025; Cohen et al., 2025; Wen et al., 2025; Wang et al., 2025a) into the training dynamics of gradient-based algorithms on this landscape have led to the consensus that the anisotropic landscape induces a distinct *time-scale separation* in the training dynamics (Figure 2 (right)): **1) Fast dynamics:** Along *sharp* directions, the dynamics exhibit rapid but non-divergent oscillations, which dictate training stability yet contribute minimally to loss reduction. **2) Slow dynamics:** Along *flat* directions, the dynamics evolves steadily but slowly, dominating total loss reduction.

Leveraging these insights, our LITE approach is designed to accelerate training by boosting the slow training dynamics along flat directions (see schematic in Figure 2 (right)). More related works are deferred to Appendix A.

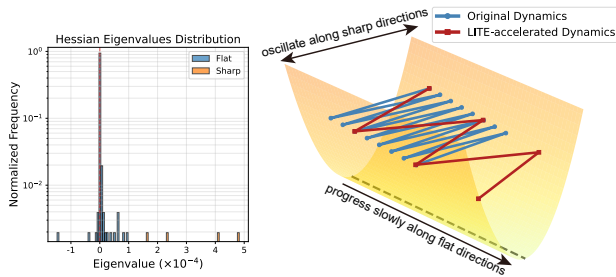


Figure 2. (left) Hessian eigenvalue distribution of an `up_proj` FFN block in a toy LLaMA model; (right) Schematic illustration of the time-scale separation property and the acceleration mechanism of the LITE approach.

### 3. Preliminary

**Notations.** Let  $v_k$  denote the  $k$ -th component of a vector  $v$ . For a positive semi-definite matrix  $F$ , we define the induced inner product and norm as  $\langle u, v \rangle_F = u^\top F v$  and  $\|u\|_F = \sqrt{u^\top F u}$  respectively, omitting the subscript when  $F = I$ . Given a matrix-valued function  $F : \mathbb{R}^p \rightarrow \mathbb{R}^{p \times p}$ , its directional derivative is written as  $\nabla F(w)[v] = \lim_{\epsilon \rightarrow 0} (F(w + \epsilon v) - F(w))/\epsilon$ . We distinguish between Riemannian operators ( $\text{grad}$ ,  $\text{Hess}$ ) and their Euclidean counterparts ( $\nabla$ ,  $\nabla^2$ ). The symbol  $\odot$  represents the element-wise product, and  $\otimes$  denotes the Kronecker product. A subscript or superscript  $F$  is occasionally attached to geometric operators (e.g.  $\nabla^F$ ) to emphasize they are induced by the Riemannian metric  $F$ .

#### 3.1. Manifold Optimization

Manifold optimization deals with variables constrained to a Riemannian manifold. In this work, we consider a special case: the variable (parameter) space  $\mathbb{R}^p$  not as a standard Euclidean space, but as a Riemannian manifold  $\mathcal{M} = (\mathbb{R}^p, F)$  equipped with metric  $F(w) \in \mathbb{R}^{p \times p}$  at each  $w \in \mathbb{R}^p$ . This

geometric perspective allows us to analyze the optimization landscape through the lens of local curvature defined by  $F$ . Detailed discussions are provided in Appendix F.

**Tangent and Cotangent Spaces.** At any point  $w \in \mathcal{M}$ , the tangent space  $T_w \mathcal{M} \cong \mathbb{R}^p$  represents the vector space of all possible directional velocities (or parameter perturbations). The Riemannian metric induces a norm  $\|\cdot\|_{F(w)}$  on the tangent space. The cotangent space  $T_w^* \mathcal{M}$  is defined as the dual space to  $T_w \mathcal{M}$ , which is equipped with the norm  $\|\cdot\|_{F(w)^{-1}}$  and is also isomorphism to  $\mathbb{R}^p$ . The metric induces linear isomorphisms  $F(w)^{-1} : T_w^* \mathcal{M} \rightarrow T_w \mathcal{M}$  and  $F(w) : T_w \mathcal{M} \rightarrow T_w^* \mathcal{M}$ . While the Euclidean gradient  $\nabla f(w)$  naturally resides in  $T_w^* \mathcal{M}$ , the Riemannian gradient is obtained by mapping it back to the tangent space via  $\text{grad} f(w) = F(w)^{-1} \nabla f(w)$ . It gives the steepest descent steps in the local geometry:

$$-F(w)^{-1} \nabla f(w) = \lim_{\epsilon \rightarrow 0} \underset{\|h\|_{F(w)} \leq \epsilon}{\text{argmin}} \frac{f(w+h) - f(w)}{\epsilon}.$$

**Levi-Civita Connection.** Levi-Civita connection  $\nabla_{(\cdot)}(\cdot)$  provides a rigorous tool for differentiating vector fields on Riemannian manifolds, generalizing the concept of directional derivatives from Euclidean space to curved geometries. For vector fields  $u, v$ ,  $\nabla_u v$  yields a vector field that quantifies how  $v$  twists or deviates from a parallel field as it moves along  $u$ . Levi-Civita connection is essential for defining the Riemannian Hessian, which is given by  $\text{Hess} f(w)[u] = \nabla_u \text{grad} f(w)$  for any vector field  $u$ .

#### 3.2. ODE Perspective of Momentum-based Algorithms

Continuous-time modeling via ODEs constitutes a rigorous and principled paradigm for analyzing momentum-based algorithms, offering *deep theoretical insights and clear intuitions* into their underlying dynamics. (Su et al., 2016) proposed a second-order inertial system that characterizes the continuous-time limit to Nesterov accelerated gradient (momentum) method. Further, (Shi et al., 2021; Attouch et al., 2022) introduced an inertial system with Hessian damping (ISHD) that can depict the momentum-based algorithms in higher resolution, which takes the form

$$\ddot{w}_t + \alpha_t \dot{w}_t + \beta_t \nabla^2 f(w_t) \dot{w}_t + \gamma_t \nabla f(w_t) = 0, \quad (1)$$

where  $\alpha_t, \beta_t, \gamma_t \geq 0$  denote the coefficients for momentum decay, Hessian damping, and the gradient driving force, respectively. Discretizing this system recovers various momentum methods: specifically, setting  $\beta_t = 0$  yields Heavy Ball momentum, while  $\beta_t > 0$  corresponds to Nesterov-type momentum. Crucially, the Hessian damping term  $\nabla^2 f(w_t) \dot{w}_t$  and its discretized counterpart  $\nabla f(w_k) - \nabla f(w_{k-1})$  serves to mitigate oscillations, thereby enhancing the stability of standard Heavy Ball dynamics. Further details on discretization, equivalent formulations, and the role of Hessian damping are provided in Section E.

## 4. A Unified Riemannian ODE Framework for Understanding Adaptive Algorithms

Adaptive optimizers synergize momentum with preconditioners, leveraging momentum-induced acceleration while simultaneously adapting step sizes anisotropically for efficient convergence. In this section, we interpret the mechanics of these algorithms by modeling them as inertial systems (ODEs) with Hessian damping on a Riemannian manifold (RISHD) equipped with preconditioner-induced metrics.

### 4.1. A Unified Discrete Formulation

Formally, the update rules of most adaptive optimizers can be encapsulated within a single unified formulation:

$$\begin{cases} m_k = (1 - \alpha)m_{k-1} + \nabla f(w_k), \\ w_{k+1} = w_k - \eta_k F(w_k)^{-1}(m_k + \beta \nabla f(w_k)), \end{cases} \quad (2)$$

where  $w_k$  denotes the parameters,  $m_k$  is the momentum<sup>1</sup>,  $F(w_k)^{-1}$  serves as the preconditioner, and the term  $\beta \nabla f(w_k)$  yields a Nesterov-type momentum.

In the context of neural network training, the **design of the preconditioner**  $F^{-1}$  is typically guided by: 1) *Block-Diagonal Structure*: To manage computational complexity,  $F$  is generally treated as a block-diagonal matrix, where each block corresponds to the parameter tensor of a specific layer; 2) *EMA Estimation*: Instead of computing exact curvature, EMA is commonly used to estimate  $F(w)$  to suppress stochastic noise from mini-batch gradients and stabilize the estimation of the local curvature; 3) *Fisher-type Approximation*: Fundamentally, most adaptive algorithms aim to approximate the Fisher-type metric  $\hat{F}(w) = (\mathbb{E}[gg^\top])^{\frac{1}{2}}$ , where  $g$  is the stochastic gradient of a specific block.

By varying the structure of  $F$  and the momentum coefficient  $\beta$ , **the formulation (2) subsumes a broad family of adaptive methods**, including N-AdamW, Muon, and Soap. See Table 1 and Appendix I for further details.

**Optimizers using Hessian Damping** Several recent optimizers, including Lion, MARS (Yuan et al., 2025), and Muon, incorporate Nesterov-style momentum to surpass the performance of vanilla Heavy Ball momentum. The key step is preconditioning  $m_k + \beta g_k$  as in (2) rather than the standard momentum  $m_k$ . As discussed in Appendix E, the  $\beta g_k$  term induces an implicit Hessian damping effect by  $\nabla f(w_k) - \nabla f(w_{k-1}) \approx \nabla^2 f(w_k)(w_k - w_{k-1})$ , crucial for reducing oscillations on ill-conditioned landscapes.

### 4.2. The Riemannian ODE Framework

**Continuous-time Viewpoint.** Now we interpret the generalized form (2) as a approximated discretization of a Rie-

mannian ODE. Leveraging Levi-Civita connection  $\nabla_{(\cdot)}^F(\cdot)$  to generalize the Euclidean derivatives to the covariant derivatives, we can extend the Euclidean ISHD (1) to the Riemannian ISHD (RISHD) on  $(\mathcal{M}, F)$ :

$$\nabla_{\dot{w}_t}^F \dot{w}_t + \alpha_t \dot{w}_t + \beta_t \text{Hess}_F(w_t) \dot{w}_t + \gamma_t \text{grad}_F f(w_t) = 0. \quad (3)$$

where  $\text{Hess}_F$  and  $\text{grad}_F$  denote  $F$ -induced Riemannian Hessian and gradient respectively.

**First-order Tangent-Cotangent Formulation.** We can introduce the momentum variable  $m_t$  tracking the velocity  $\dot{w}_t$  to decouple (3) into a first order system that evolves in the tangent space (T) and cotangent space (C) respectively:

**Proposition 4.1** (Adapted from Proposition G.2). *If  $\alpha_t = \alpha - \dot{\eta}_t/\eta_t$ ,  $\beta_t = \beta\eta_t$ ,  $\gamma_t = \eta_t(\alpha\beta + 1)$ , (3) is equivalent to*

$$\begin{cases} \dot{w}_t = -\eta_t F(w_t)^{-1}(m_t + \beta \nabla f(w_t)), & \text{(T)} \\ \dot{m}_t = -\alpha m_t + \nabla f(w_t) + R_t, & \text{(C)} \end{cases}$$

where the Riemannian correction term  $R_t$  is defined in (53).

The term  $R_t$  mainly depends on  $\eta_t$  and  $\nabla F(w_t)$ . It is typically negligible compared to  $\nabla f(w_t)$  and  $m_t$  due to the small step size  $\eta_t$  and the stable preconditioner (implying a small  $\nabla F(w_t)$ ). Thus we can ignore  $R_t$  for brevity.

The decoupled formulation in (T) and (C) elucidate the nature of RISHD in (3): Momentum evolves in the cotangent space, while the preconditioner  $F^{-1}$  maps it to the tangent space to drive the parameter update. This form also naturally gives the specific form in which modern adaptive methods incorporate momentum: the preconditioner is applied to the momentum accumulated from raw gradients, rather than accumulating preconditioned gradients by EMA. Furthermore, this Riemannian ODE framework is readily extensible to higher-order cases, enabling the characterization of complex momentum schemes such as the multi-timescale momentum in AdEMAMix (Pagliardini et al., 2025) (Appendix E.3).

**Joint effect of the preconditioner and momentum.** The continuous-time ODE framework (3) is instrumental and intuitive in elucidating the joint mechanism of preconditioning and momentum, which remains opaque in discrete formulations. Assuming  $F(w)$  is a slowly varying Hessian approximation, the induced Riemannian metric effectively mitigates ill-conditioning, as it yields a Riemannian Hessian  $\text{Hess}_F f(w) \approx F^{-1}(w) \nabla^2 f(w)$  which exhibits a much better condition number than the Euclidean Hessian  $\nabla^2 f(w)$ . Leveraging this improved geometry, the damping term  $-(\alpha_t + \beta_t \text{Hess} f(w)) \dot{w}_t$ , which encapsulates the momentum effect in the continuous dynamics, then acts to further accelerate convergence.

**Connection with the Discrete Formulation.** Compared to the original second-order system (3), the equivalent first-order coupled system offers a more direct path for numerical

<sup>1</sup>The missing coefficient  $\alpha$  of  $\nabla f$  can be absorbed in  $\eta_k$ .

Table 1. Update forms (matrix and vector) and their corresponding approximations of the metric  $F$  (up to a constant scaling factor) for common adaptive optimizers.  $m$  denotes the EMA-type momentum,  $g$  represents the stochastic gradient, and  $M_\beta = M + \beta G$ . Capital letters denote the matrix forms corresponding to their vector counterparts (lowercase). For AdamW, we present its Nesterov-accelerated variant (N-AdamW). See Appendix I for further discussions and details.

Algorithms	Matrix Form	Vector Form	$F$ (up to a constant factor)
N-AdamW	$\frac{M+\beta g}{\sqrt{V}}$	$\text{diag } v^{-\frac{1}{2}}(m + \beta g)$	$(\text{diag } \mathbb{E}[gg^\top])^{\frac{1}{2}}$
Muon	$M_\beta(M_\beta^\top M_\beta)^{-\frac{1}{2}}$	$((M_\beta^\top M_\beta) \otimes I)^{-\frac{1}{2}}(m + \beta g)$	$(\mathbb{E}[G^\top G])^{\frac{1}{2}} \otimes I$
SOAP	$Q_i \frac{Q_i^\top M Q_r}{\sqrt{V_{\text{rot}}}} Q_r^\top$	$(Q_r \otimes Q_i)(\text{diag } v_{\text{rot}})^{-\frac{1}{2}}(Q_r^\top \otimes Q_i^\top)m$	$(Q_r \otimes Q_i)(\text{diag } \mathbb{E}[g_{\text{rot}}g_{\text{rot}}^\top])^{\frac{1}{2}}(Q_r^\top \otimes Q_i^\top)$

implementation. Applying a semi-implicit Euler discretization scheme to (T) and (C) with step size  $h = 1$  and  $R_t \approx 0$  yields the discrete formulation (2).

## 5. The LITE Approach

In this section, we introduce LITE, an acceleration strategy grounded in the characteristics of the loss landscape and the theoretical insights regarding the synergistic role of momentum and preconditioning established in Section 4.2.

As discussed in Section 2, the trajectory along sharp directions exhibits significant fluctuations, and the efficiency of traversal along flat directions becomes the critical determinant of the final loss. Motivated by this, our strategy aims to **selectively accelerate optimization along flat directions while preserving stability in sharp directions**. To implement this, we adopt a decoupled tuning scheme: we anchor the hyper-parameters governing the sharp directions in (2) to maintain stability, while adaptively adjusting those corresponding to the flat directions. In the following discussion, we derive a heuristic adjustment scheme for the flat-direction hyper-parameters from the perspective of continuous-time dynamics in Section 4.

### 5.1. Acceleration Methods from the ODE Perspective

We begin by analyzing the role of momentum through the lens of the continuous-time limit in (1), focusing initially on the Euclidean case of (3) for clarity. Intuitively, the system models the dynamics of a particle moving within a potential field defined by  $f$ . The particle at  $w_t$  is subject to the combined effects of a driving force  $-\gamma_t \nabla f(w_t)$  and a curvature-adaptive damping (drag force)  $-(\alpha_t I + \beta_t \nabla^2 f(w_t)) \dot{w}_t$  opposing its velocity  $\dot{w}_t$ , with its acceleration  $\ddot{w}_t$  governed by Newton’s Second Law. Along flat directions, we can enhance the accumulation of velocity by increasing the driving force coefficient  $\gamma_t$  while minimizing the effective damping (*i.e.* reducing the eigenvalues of  $\alpha_t I + \beta_t \nabla^2 f(w_t)$ ). Since flat directions are often characterized by non-convexity, our strategy is **increasing  $\gamma_t$  and  $\beta_t$  in the flat directions**.<sup>2</sup>

<sup>2</sup>Regarding damping, we do not tune  $\alpha_t$  for the sake of simplicity. While  $\alpha_t$  offers a similar mechanism for reducing damping,

### Algorithm 1 LITE Strategy

- 1: **Input:**  $w_0, m_0, \{\eta_k\}, \alpha, \chi \geq 1, \beta_2 \geq \beta_1 \geq 0$ .
  - 2: **for**  $k = 0$  **to**  $K$  **do**
  - 3:   Update momentum  $m_k = (1 - \alpha)m_{k-1} + \nabla f(w_k)$ .
  - 4:   Estimate projection  $Q_k$  onto the flat direction.
  - 5:   Estimate the update direction
- $$u_k = (I - Q_k)F(w_k)^{-1}(m_k + \beta_1 \nabla f(w_k)) + \chi Q_k F(w_k)^{-1}(m_k + \beta_2 \nabla f(w_k)).$$
- 6:   Update parameters  $w_{k+1} = w_k - \eta_k u_k$ .
  - 7: **end for**

The above discussion, framed in terms of damping and motion in Euclidean space, can be naturally extended to Riemannian manifolds (curved spaces). The corresponding physical background shifts from Newtonian mechanics to Lagrangian mechanics (Arnold, 1989), yet the same conclusions hold. For sharp directions, the coefficients remain unchanged to maintain stability conditions. Given the relationships  $\gamma_t = (1 + \alpha\beta)\eta_t$  and  $\beta_t = \beta\eta_t$  in (3), we can amplify  $\gamma_t$  and  $\beta_t$  by increasing  $\beta$  and  $\eta_t$ . Finally, assuming well-aligned top eigenspaces between  $F$  and the Hessian, the accelerated dynamics is given by:

$$\begin{cases} \dot{w}_t = -\eta_t F(w_t)^{-1} P_t(m_t + \beta_1 \nabla f(w_t)) \\ \quad - \chi \eta_t F(w_t)^{-1} Q_t(m_t + \beta_2 \nabla f(w_t)), \\ \dot{m}_t = -\alpha m_t + \nabla f(w_t), \end{cases} \quad (4)$$

where  $P_t$  is the projection to the sharp subspace,  $Q_t = I - P_t$ , and  $\chi \geq 1, \beta_2 \geq \beta_1 \geq 0$  are hyper-parameters. Discretizing (4) like (2) yields the accelerated algorithms framework LITE (Algorithm 1), where we simply notations for brevity. This formulation naturally yields amplified update magnitudes along flat directions, facilitating faster traversal through these slow-progressing regimes. An illustrative theoretical analysis of the LITE acceleration mechanism on a quadratic function is provided in Appendix H.

$\beta_t$  is preferred as it provides curvature adaptivity.

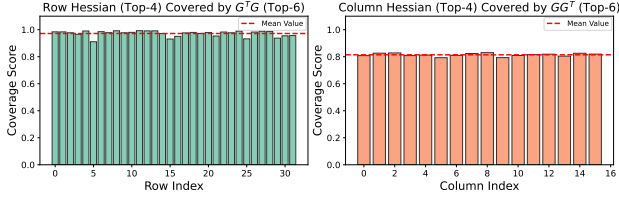


Figure 3. Coverage of the top eigenspaces of row (column) Hessians by those of  $G^T G$  ( $GG^T$ ) for the `up_proj` block of an FFN layer. A higher score indicates a greater degree of containment.

## 5.2. Practical Implementation of LITE

In this section, we present practical execution strategies for implementing LITE (Algorithm 1) in LLM-pretraining. Our approach specifically targets the anisotropic landscape inherent to each parameter block. The core objective is to efficiently identify the flat (or sharp) directions within each parameter block.

**Efficiently approximating the flat directions** Prior research (Martens, 2020; Morwani et al., 2025) demonstrates that the Fisher matrix and Shampoo-like preconditioners effectively approximate the Gauss-Newton component, the dominant term in the Hessian. Since Muon and SOAP adopt Shampoo-like methods to approximate the square root of the Fisher matrix via Kronecker factorization, we hypothesize that *the top eigenspaces of their preconditioners and the Hessian are highly aligned*.

To verify this hypothesis, we conducted experiments on a toy LLaMA-2 model (see experimental details in Appendix C.1). Figure 2 (left) confirms that the landscape within each block is ill-conditioned, with sharp directions accounting for only a small proportion of the spectrum. Besides, Figure 3 indicate that for a small dimension  $d_s = 4$  (4/32 and 4/16), the top- $d_s$  eigenspaces of the Hessian (for rows/columns) can be effectively covered by a subspace of  $G^T G$  ( $GG^T$ ) of dimension only slightly larger than  $d_s$ , where  $G$  denotes the stochastic gradient matrix. Consequently, by taking the orthogonal complement, we can obtain a reliable approximation of the flat directions. Since preconditioners of Muon and SOAP are constructed from  $G^T G$  ( $GG^T$ ), we propose the following acceleration schemes tailored for them.

**Accelerating Muon (MUON-LITE)** At iteration  $k$ , let  $G_k \in \mathbb{R}^{m \times n}$  ( $m \geq n$ ) represent the stochastic gradient for a given parameter block. The update process begins with the momentum accumulation  $M_k = (1 - \alpha)M_{k-1} + G_k$ , followed by the Nesterov correction  $\widetilde{M}_k = M_k + G_k / (1 - \alpha)$ <sup>3</sup>. Recognizing that  $\widetilde{M}_k^T \widetilde{M}_k$  acts as a robust proxy for the expected covariance  $\mathbb{E}[G_k^T G_k]$  (Appendix I.1), we utilize

<sup>3</sup>We adopt the Nesterov formulation consistent with (Jordan et al., 2024).

it to characterize the landscape geometry. Specifically, we construct the projection matrix  $P_k \in \mathbb{R}^{n \times n}$  onto the top- $d_s$  eigenspace of  $\widetilde{M}_k^T \widetilde{M}_k$ , where  $d_s$  specifies the dimension of the sharp subspace. A numerically efficient, optimizer state-free method for estimating  $P_k$  is detailed in Appendix B.1. Consequently, the update direction is formulated as:

$$U_k = \widetilde{M}_k (\widetilde{M}_k^T \widetilde{M}_k)^{-\frac{1}{2}} (P_k + \chi(I_n - P_k)) + G_k (G_k^T G_k)^{-\frac{1}{2}} (\beta_1 P_k + \chi \beta_2 (I_n - P_k)), \quad (5)$$

where  $\beta_2 \geq \beta_1$  are the Hessian damping coefficients, and  $\chi \geq 1$  denotes the amplification ratio of the learning rate in flat directions relative to sharp ones. Setting  $\chi = 1$  and  $\beta_{1,2} = 0$  recovers the original Muon baseline. Here we use the precondition  $(G_k^T G_k)^{-\frac{1}{2}}$  instead of  $(\widetilde{M}_k^T \widetilde{M}_k)^{-\frac{1}{2}}$  to the gradient term, since it has superior numerical stability and efficiency of applying NS iterations, and  $G_k^T G_k$  itself serves as a valid instantaneous estimator of  $\mathbb{E}[G_k^T G_k]$ .

**Accelerating SOAP (SOAP-LITE)** We retain the notation established above. As detailed in Table 1, the SOAP preconditioner explicitly provides the eigenvalues ( $V$ ) and eigenvectors ( $Q_r \otimes Q_l$ ) of the curvature estimation. Consequently, we can identify the sharp directions directly in the  $(Q_r \otimes Q_l)$ -rotated eigenspace by selecting the top- $d_s$  ( $d_s \leq mn$ ) elements of  $V$ . Let  $P_k \in \mathbb{R}^{m \times n}$  denote the mask matrix indicating the sharp directions at iteration  $k$ , and let  $Q_k = 1_m 1_n^T - P_k$  represent the flat directions. The update direction for accelerating SOAP is given by:

$$U_k = Q_l \left( V_k^{-\frac{1}{2}} \odot (\beta_1 P_k + \chi \beta_2 Q_k) \odot (Q_l^T G_k Q_r) \right) Q_r^T + Q_l \left( V_k^{-\frac{1}{2}} \odot (P_k + \chi Q_k) \odot (Q_l^T M_k Q_r) \right) Q_r^T,$$

where, similar to MUON-LITE, the SOAP baseline is recovered when  $\chi = 1$  and  $\beta_{1,2} = 0$ . In practice, to enhance training stability, we implement  $P_k$  using a soft transition scheme (smoothly changing from 0 to 1) rather than a hard binary cutoff. See Appendix B.2 for implementation details.

## 6. Experiments

We evaluate LITE in accelerating Muon and SOAP on a wide range of LLM pre-training scenarios. Experimental details are provided in Appendix B and C.

### 6.1. Results on Dense Models

**Main Results.** Figures 4 and 5 compare the performance of MUON-LITE and SOAP-LITE against vanilla Muon and SOAP across a range of LLaMA model sizes on both the C4 and Pile datasets. The values of  $\{\chi, \beta_{1,2}\}$  in LITE were determined via a search on the 0.25B model experiments and were then used uniformly for other experiments.

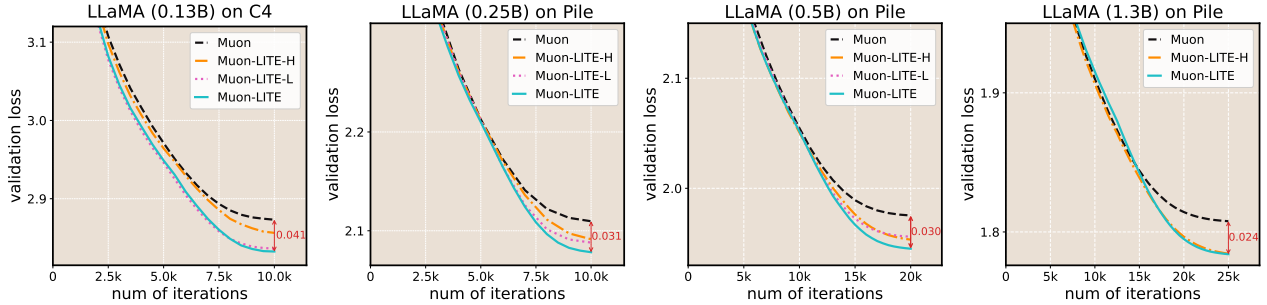


Figure 4. Performance comparison of Muon and MUON-LITE on LLM pre-training tasks. We evaluate LLaMA2 models across various sizes and datasets using a  $\cos$  learning rate schedule. The suffixes L and H denote two ablation variants of LITE: in flat directions, L increases only the learning rate ratio  $\chi \geq 1$ , while H increases only the Hessian damping coefficient  $\beta_2$ . The token batch size is approximately 2M for the 1.3B model, and 1M for others.

Across all experimental settings, MUON-LITE and SOAP-LITE consistently achieve lower terminal losses than their respective well-tuned baselines. Besides, LITE outperforms both LITE-L and LITE-H, validating the effectiveness of simultaneously increasing  $\chi$  and  $\beta_2$ . To further assess scalability, we visualize the scaling laws of MUON-LITE versus Muon in Figure 1 (right). The performance gains yielded by MUON-LITE remain consistent across a wide range of model scales, indicating its potential scalability. Further downstream analyses are provided in Appendix D.

We subsequently investigate the acceleration efficacy of LITE over extended training horizons, increasing the training token budget from  $40\times$  (10k iterations) the parameter count to  $100\times$  (25k) and  $200\times$  (50k). Figure 1 (left) indicates that the loss reduction gains yielded by MUON-LITE persist across these extended regimes. Notably, at the  $100\times$  setting, MUON-LITE achieves an approximate  $2\times$  speedup over Muon. This demonstrates the sustained scalability of MUON-LITE with respect to the number of training tokens.

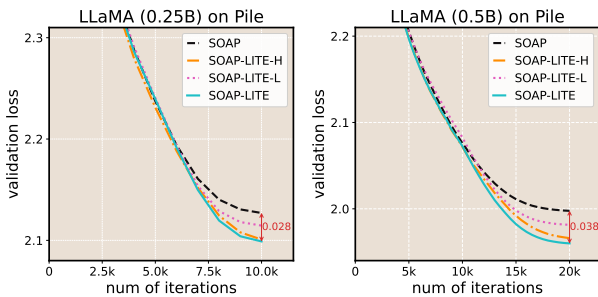


Figure 5. Performance comparison of SOAP and SOAP-LITE on LLM pre-training tasks. Same experimental setup and notations are employed as in Figure 4.

**Ablation Studies.** We demonstrate that the acceleration strategy for flat directions is detrimental when applied to sharp directions. Under the experimental setting for the 0.25B model in Figure 4, we tested applying uniform damping coefficients  $\beta_{1,2} = 0.5$  and  $\beta_{1,2} = 1.0$ . Despite these values being smaller than the coefficient used for flat direc-

tions in MUON-LITE-H ( $\beta_2 = 2.0$ ), they yielded terminal losses of 2.113 and 2.129 respectively, both even inferior to the vanilla Muon baseline (2.110). The results validate our design choice of maintaining hyper-parameters along sharp directions when selectively accelerating the flat ones.

### 6.2. Results on MoE Models

Mixture-of-experts (MoE) architectures have emerged as a critical paradigm for modern LLMs. By selectively activating a subset of experts for each token, MoE models achieve superior scaling efficiency over their dense counterparts.

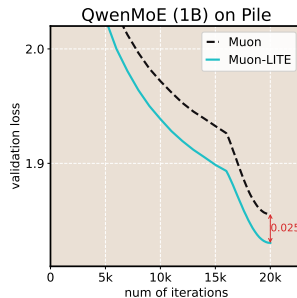


Figure 6. MUON-LITE outperforms Muon in QwenMoE pre-training tasks.

We evaluate MUON-LITE against the Muon baseline on a 1B-parameter QwenMoE model, utilizing a  $\cos$  learning rate schedule. The results demonstrate that MUON-LITE consistently outperforms Muon throughout the entire training trajectory, ultimately achieving a significantly lower terminal loss (Figure 6).

Furthermore, we observe that the performance gap between MUON-LITE and Muon progressively widens as iterations proceed during the stable phase. This trend suggests that the efficiency gains offered by MUON-LITE are likely to persist or even amplify at larger data scales.

### 7. Theoretical Analysis to Training Dynamics

In this section, we provide a theoretical characterization of the acceleration mechanism of LITE. We adopt and extend the *River-Valley* landscape framework recently proposed by (Wen et al., 2025), which models the pre-training loss landscape as a deep valley with a flat river at its bottom.

We generalize this framework to high-dimensional settings, and analyze the dynamics (4) corresponding to LITE (Algorithm 1). Our analysis demonstrates that LITE effectively accelerates the training dynamics along the River, which dictates the terminal loss. In the following, we introduce the assumptions required for our theoretical derivation.

**Assumption 7.1** (River Structure). Fix an integer  $d_s \in \mathbb{Z}_+$  and an open set  $U \subset \mathbb{R}^p$ . Let  $P_s(w)$  denote the Euclidean projection onto the top  $d_s$  eigenspace of the Hessian  $\nabla^2 f(w)$ . We assume that  $P_s(w)$  varies smoothly with respect to  $w$ , and that the set (referred to as *River*)

$$\mathcal{R} = \{w \in U : P_s(w)\nabla f(w) = 0\} \quad (6)$$

constitutes a  $(p - d_s)$ -dimensional manifold. Furthermore, we assume that within the sharp subspace  $\text{Range}(P_s(w))$ , the Hessian  $\nabla^2 f(w)$  and the preconditioner  $F(w)$  share a common eigen-basis. Finally, the ODE

$$\frac{d}{dt}\psi_t(w) = -P_s(\psi_t(w))F^{-1}(\psi_t(w))\nabla f(\psi_t(w)), \quad (7)$$

initialized at any  $\psi_0(w) = w \in U$  is assumed to remain and converge within  $U$  as  $t \rightarrow \infty$ .

Under Assumption 7.1, we define the ‘‘projection’’ map to River  $\Phi : U \rightarrow \mathcal{R}$  via the limit of the flow:  $\Phi(w) := \lim_{t \rightarrow \infty} \psi_t(w)$ . This ensures  $\Phi(w) \in \mathcal{R}$  since the stationarity of the flow implies  $P_s\nabla f = 0$ .

**Assumption 7.2** (Regularity, Smoothness and Conservation). Given the domain  $U$  in Assumption 7.1, we assume:

1.  $f$  is analytic in  $U$ . Let  $(\cdot)|_s$  denote the restriction of an operator to the sharp subspace  $\text{Range}(P_s(w))$ . For all  $w \in U$ , the eigenvalues of  $\nabla^2 f(w)$ ,  $F(w)$ ,  $F(w)|_s$ ,  $(F^{-\frac{1}{2}}(w)\nabla^2 f(w)F^{-\frac{1}{2}}(w))|_s$  lie in  $[-L, L]$ ,  $[\lambda_F, \rho]$ ,  $[\lambda_{F_s}, \rho]$  and  $[\lambda_{H_{F,s}}, L_{H_{F,s}}]$ , respectively.
2. There exist constants  $\delta, \delta_F, \varepsilon \geq 0$  with  $\max\{\delta, \delta_F\} \leq \varepsilon$ , such that for any  $w \in U$ ,  $\|\nabla f(w)\|_{F(w)^{-1}} \leq G$ ,  $\|\nabla P_s(w)\|_{\text{op}} \leq \delta/G$  and  $\|\nabla F(w)\|_{\text{op}} \leq \delta_F/G$ . See (75) for detailed definition of the operator norm  $\|\cdot\|_{\text{op}}$ .
3. There exists a time horizon  $T_{\max} > 0$ , dependent on the hyper-parameters  $(\alpha, \beta_1, \{\eta_t\}_{t \geq 0}, \chi, \beta_2)$ , such that for any initialization  $w_0 \in U$  with initial momentum  $m_0 = 0$ , the trajectory  $w_t$  generated by the dynamics (4) remains strictly within  $U$  for all  $t \in [0, T_{\max}]$ .

**Theorem 7.3.** Suppose Assumptions 7.1 and 7.2 hold. Define the decay rate  $\iota_t = \min\{\alpha/2, \lambda_{H_{F,s}}\beta_1\eta_t\}$  and the forgetting kernel  $K(t) = \exp\left(-\int_0^t \iota_s ds\right)$ . Assuming  $\dot{\eta}_t \leq 0$ , there exists a constant  $\varepsilon_0 > 0$  (dependent on  $f$  and the hyper-parameters in (4)) such that for all  $\varepsilon \leq \varepsilon_0$ , the trajectory  $w_t$  governed by (4) satisfies the attraction bound:

$$\|w_t - \Phi(w_t)\|_2^2 \lesssim K(t) + \varepsilon, \quad (8)$$

and the ‘‘projected’’ trajectory  $z_t = \Phi(w_t)$  follows the coupled dynamics:

$$\begin{cases} \dot{z}_t = -\eta_t(\chi P_{\mathcal{R}}(z_t)F(z_t)^{-1}(s_t + \beta_2\nabla f(z_t)) + \epsilon_{z,t}), \\ \dot{s}_t = -\alpha s_t + \nabla f(z_t), \end{cases} \quad (9)$$

with  $s_0 = 0$ , where  $\epsilon_{z,t}$  denotes a perturbation term. Finally, defining  $b_t = \|P_{\mathcal{R}}(z_t)F(z_t)^{-1}\nabla f(z_t)\|_{F(z_t)}^2 + \|P_{\mathcal{R}}(z_t)F(z_t)^{-1}s_t\|_{F(z_t)}^2$ , the perturbation error satisfies:

$$\|\epsilon_{z,t}\|_{F(z_t)}^2 \lesssim K(t) + \varepsilon^2 b_t + \varepsilon \int_0^t K(\tau - t)b_\tau d\tau. \quad (10)$$

The proof is in Lemmas J.6 and J.11. We treat  $\varepsilon$  as a small constant to enforce a slowly varying  $\mathcal{R}$ . Inspired by (Atouch et al., 2022), we can take  $\eta_t \equiv \eta$ ,  $\alpha = 2\lambda_{F_{H,s}}^{1/2}\eta$ ,  $\beta_1 = \lambda_{F_{H,s}}^{-1/2}$  to achieve a fast decay  $K(t) = \exp(-\eta\lambda_{F_{H,s}}^{1/2}t)$  (i.e. fast convergence on sharp directions). In this case, Theorem 7.3 indicates that the dynamics (4) first converge to the  $\mathcal{O}(\varepsilon^{1/2})$  neighborhood of  $\mathcal{R}$  after a  $\Theta(\eta^{-1}\lambda_{F_{H,s}}^{-1/2}\log(\varepsilon^{-1}))$  interval, then faithfully track the decoupled acceleration dynamics on  $\mathcal{R}$  closely, where the tracking error exhibits a fading memory property, driven predominantly by the immediate history of the underlying dynamics. Next we clarify how  $\chi$  and  $\beta_2$  influence the convergence of the decoupled dynamics in  $\mathcal{R}$ , where the detailed proof is in Lemma J.12.

**Theorem 7.4.** Suppose Assumptions 7.1, 7.2 hold and  $\dot{\eta}_t \leq 0$ . Let  $\Delta_f = f(z_0) - \inf f$ . For the unperturbed dynamics in (9) with  $\epsilon_{z,t} \equiv 0$ , there exists a constant  $\varepsilon_1$  (depending on  $f$  and hyper-parameters in (4)), such that for any  $\varepsilon \leq \varepsilon_1$  and any  $T \leq T_{\max}$ , the trajectory  $z_t$  satisfies

$$\begin{aligned} \int_0^T \eta_t \|P_{\mathcal{R}}(z_t)F(z_t)^{-1}\nabla f(z_t)\|_{F(z_t)}^2 dt &\leq \frac{2\Delta_f}{\chi\beta_2}, \\ \int_0^T \eta_t \|s_t\|_{F(z_t)}^2 dt &\leq \frac{2\Delta_f}{\chi\alpha}. \end{aligned}$$

Theorem 7.4 demonstrates that increasing both  $\chi \geq 1$  and  $\beta_2$  yields a tighter integral bound for the Riemannian gradient on  $\mathcal{R}$  (i.e.  $P_{\mathcal{R}}(z_t)F(z_t)^{-1}\nabla f(z_t)$ ) and the momentum  $s_t$ . This theoretical result validates the effectiveness of the strategy employed in LITE.

## 8. Conclusion

We propose LITE, a generalized strategy to accelerate LLM pre-training by enhancing training dynamics along flat directions. Experimentally, LITE significantly enhances state-of-the-art optimizers such as Muon and SOAP. Our results indicate that LITE consistently achieves lower terminal loss and exhibits superior scaling behavior compared to corresponding baselines across various LLM pre-training tasks. For future work, we plan to explore adaptive mechanisms for dynamic hyper-parameter tuning within LITE, and extending its integration with other emerging optimizers.

## Impact Statement

This paper presents work whose goal is to advance the field of Machine Learning, with a focus on understanding and improving the pre-training of LLMs. There are many potential societal consequences of our work, none which we feel must be specifically highlighted here.

## References

- Amsel, N., Persson, D., Musco, C., and Gower, R. M. The polar express: Optimal matrix sign methods and their application to the muon algorithm, 2025. URL <https://arxiv.org/abs/2505.16932>.
- Arnold, V. I. *Mathematical Methods of Classical Mechanics*. Springer-Verlag, New York, 2nd edition, 1989. ISBN 978-1-4757-2063-1.
- Attouch, H., Chbani, Z., Fadili, J., and Riahi, H. First-order optimization algorithms via inertial systems with Hessian driven damping. *Mathematical Programming*, 193(1): 113–155, 2022.
- Bernstein, J. and Newhouse, L. Old optimizer, new norm: An anthology, 2024. URL <https://arxiv.org/abs/2409.20325>.
- Cohen, J., Damian, A., Talwalkar, A., Kolter, J. Z., and Lee, J. D. Understanding optimization in deep learning with central flows. In *The Thirteenth International Conference on Learning Representations*, 2025.
- Falconer, K. J. Differentiation of the limit mapping in a dynamical system. *Journal of the London Mathematical Society*, s2-27(2):356–372, 1983.
- Frans, K., Levine, S., and Abbeel, P. A stable whitening optimizer for efficient neural network training, 2025. URL <https://arxiv.org/abs/2506.07254>.
- Gao, L., Biderman, S., Black, S., Golding, L., Hoppe, T., Foster, C., Phang, J., He, H., Thite, A., Nabeshima, N., et al. The pile: An 800gb dataset of diverse text for language modeling. *arXiv preprint arXiv:2101.00027*, 2020.
- Ghorbani, B., Krishnan, S., and Xiao, Y. An investigation into neural net optimization via hessian eigenvalue density. In *Proceedings of the 36th International Conference on Machine Learning*, volume 97 of *Proceedings of Machine Learning Research*, pp. 2232–2241. PMLR, 09–15 Jun 2019.
- Gupta, V., Koren, T., and Singer, Y. Shampoo: Preconditioned stochastic tensor optimization. In *Proceedings of the 35th International Conference on Machine Learning*, volume 80 of *Proceedings of Machine Learning Research*, pp. 1842–1850. PMLR, 10–15 Jul 2018.
- Hägele, A., Bakouch, E., Kosson, A., Von Werra, L., Jaggi, M., et al. Scaling laws and compute-optimal training beyond fixed training durations. *Advances in Neural Information Processing Systems*, 37:76232–76264, 2024.
- Hoffmann, J., Borgeaud, S., Mensch, A., Buchatskaya, E., Cai, T., Rutherford, E., Casas, D. d. L., Hendricks, L. A., Welbl, J., Clark, A., et al. Training compute-optimal large language models. *arXiv preprint arXiv:2203.15556*, 2022.
- Hu, S., Tu, Y., Han, X., He, C., Cui, G., Long, X., Zheng, Z., Fang, Y., Huang, Y., Zhao, W., et al. Minicpm: Unveiling the potential of small language models with scalable training strategies. *arXiv preprint arXiv:2404.06395*, 2024.
- Huang, T., Hu, H., Zhang, Z., Jin, G., Li, X., Shen, L., Chen, T., Liu, L., Wen, Q., Wang, Z., and Liu, S. Stable-spam: How to train in 4-bit more stably than 16-bit adam, 2025. URL <https://arxiv.org/abs/2502.17055>.
- Jordan, K., Jin, Y., Boza, V., You, J., Cesista, F., Newhouse, L., and Bernstein, J. Muon: An optimizer for hidden layers in neural networks, 2024. URL <https://kellerjordan.github.io/posts/muon/>.
- Kingma, D. P. and Ba, J. Adam: A method for stochastic optimization. *arXiv preprint arXiv:1412.6980*, 2014.
- Lau, T. T.-K., Long, Q., and Su, W. Polargrad: A class of matrix-gradient optimizers from a unifying preconditioning perspective, 2026. URL <https://arxiv.org/abs/2505.21799>.
- Lee, J. M. *Introduction to Riemannian Manifolds*, volume 176. Springer, New York, NY, 2 edition, 2018.
- Liang, K., Chen, L., Liu, B., and Liu, Q. Cautious optimizers: Improving training with one line of code, 2025. URL <https://arxiv.org/abs/2411.16085>.
- Liu, H., Li, Z., Hall, D. L. W., Liang, P., and Ma, T. Sophia: A scalable stochastic second-order optimizer for language model pre-training. In *The Twelfth International Conference on Learning Representations*, 2024.
- Liu, J., Su, J., Yao, X., Jiang, Z., Lai, G., Du, Y., Qin, Y., Xu, W., Lu, E., Yan, J., et al. Muon is scalable for llm training. *arXiv preprint arXiv:2502.16982*, 2025a.
- Liu, L., Xu, Z., Zhang, Z., Kang, H., Li, Z., Liang, C., Chen, W., and Zhao, T. Cosmos: A hybrid adaptive optimizer for memory-efficient training of llms, 2025b. URL <https://arxiv.org/abs/2502.17410>.
- Loshchilov, I. and Hutter, F. Decoupled weight decay regularization. *arXiv preprint arXiv:1711.05101*, 2017.

- Lu, Y., Wang, L., and Liu, J. Understanding soap from the perspective of gradient whitening, 2025. URL <https://arxiv.org/abs/2509.22938>.
- Martens, J. New insights and perspectives on the natural gradient method. *Journal of Machine Learning Research*, 21(146):1–76, 2020.
- Martens, J. and Grosse, R. Optimizing neural networks with kronecker-factored approximate curvature. In *Proceedings of the 32nd International Conference on Machine Learning*, volume 37 of *Proceedings of Machine Learning Research*, pp. 2408–2417. PMLR, 07–09 Jul 2015.
- Morwani, D., Shapira, I., Vyas, N., Eran Malach, Kakade, S. M., and Janson, L. A new perspective on shampoo’s preconditioner. In *The Thirteenth International Conference on Learning Representations*, 2025.
- Pagliardini, M., Ablin, P., and Grangier, D. The adEMAMix optimizer: Better, faster, older. In *The Thirteenth International Conference on Learning Representations*, 2025.
- Pethick, T., Xie, W., Antonakopoulos, K., Zhu, Z., Silveti-Falls, A., and Cevher, V. Training deep learning models with norm-constrained LMOs. In *Forty-second International Conference on Machine Learning*, 2025.
- Raffel, C., Shazeer, N., Roberts, A., Lee, K., Narang, S., Matena, M., Zhou, Y., Li, W., and Liu, P. J. Exploring the limits of transfer learning with a unified text-to-text transformer. *The Journal of Machine Learning Research*, 21(1):5485–5551, 2020.
- Shi, B., Du, S. S., Jordan, M. I., and Su, W. J. Understanding the acceleration phenomenon via high-resolution differential equations. *Mathematical Programming*, 195(1-2), 2021.
- Shi, H.-J. M., Lee, T.-H., Iwasaki, S., Gallego-Posada, J., Li, Z., Rangadurai, K., Mudigere, D., and Rabbat, M. A distributed data-parallel pytorch implementation of the distributed shampoo optimizer for training neural networks at-scale, 2023. URL <https://arxiv.org/abs/2309.06497>.
- Song, M., Ahn, K., and Yun, C. Does SGD really happen in tiny subspaces? In *The Thirteenth International Conference on Learning Representations*, 2025.
- Staib, M., Reddi, S., Kale, S., Kumar, S., and Sra, S. Escaping saddle points with adaptive gradient methods. In *Proceedings of the 36th International Conference on Machine Learning*, volume 97 of *Proceedings of Machine Learning Research*, pp. 5956–5965. PMLR, 09–15 Jun 2019.
- Su, J., Ahmed, M., Lu, Y., Pan, S., Bo, W., and Liu, Y. Roformer: Enhanced transformer with rotary position embedding. *Neurocomputing*, 568:127063, 2024.
- Su, W. Isotropic curvature model for understanding deep learning optimization: Is gradient orthogonalization optimal?, 2025. URL <https://arxiv.org/abs/2511.00674>.
- Su, W., Boyd, S., and Candès, E. J. A differential equation for modeling nesterov’s accelerated gradient method: Theory and insights. *Journal of Machine Learning Research*, 17(153):1–43, 2016.
- Team, K. Kimi k2: Open agentic intelligence, 2025. URL <https://arxiv.org/abs/2507.20534>.
- Touvron, H., Lavril, T., Izacard, G., Martinet, X., Lachaux, M.-A., Lacroix, T., Rozière, B., Goyal, N., Hambro, E., Azhar, F., Rodriguez, A., Joulin, A., Grave, E., and Lample, G. Llama: Open and efficient foundation language models, 2023a. URL <https://arxiv.org/abs/2302.13971>.
- Touvron, H., Martin, L., Stone, K., Albert, P., Almahairi, A., Babaei, Y., Bashlykov, N., Batra, S., Bhargava, P., Bhosale, S., et al. Llama 2: Open foundation and fine-tuned chat models. *arXiv preprint arXiv:2307.09288*, 2023b.
- Vyas, N., Morwani, D., Zhao, R., Shapira, I., Brandfonbrener, D., Janson, L., and Kakade, S. M. SOAP: Improving and stabilizing shampoo using adam for language modeling. In *The Thirteenth International Conference on Learning Representations*, 2025.
- Wang, J., Wang, M., Zhou, Z., Yan, J., E, W., and Wu, L. The sharpness disparity principle in transformers for accelerating language model pre-training. In *Forty-second International Conference on Machine Learning*, 2025a.
- Wang, M. and Wu, L. The noise geometry of stochastic gradient descent: A quantitative and analytical characterization. In *NeurIPS 2023 Workshop on Mathematics of Modern Machine Learning*, 2023.
- Wang, M., Wang, J., He, H., Wang, Z., Huang, G., Xiong, F., Li, Z., E, W., and Wu, L. Improving generalization and convergence by enhancing implicit regularization. In *The Thirty-eighth Annual Conference on Neural Information Processing Systems*, 2024.
- Wang, S., Zhang, F., Li, J., Du, C., Du, C., Pang, T., Yang, Z., Hong, M., and Tan, V. Y. F. Muon outperforms adam in tail-end associative memory learning, 2025b. URL <https://arxiv.org/abs/2509.26030>.

- Wen, K., Li, Z., Wang, J. S., Hall, D. L. W., Liang, P., and Ma, T. Understanding warmup-stable-decay learning rates: A river valley loss landscape view. In *The Thirteenth International Conference on Learning Representations*, 2025.
- Wu, L., Wang, M., and Su, W. J. The alignment property of SGD noise and how it helps select flat minima: A stability analysis. In *Advances in Neural Information Processing Systems*, 2022.
- Xie, T., Luo, H., Tang, H., Hu, Y., Liu, J. K., Ren, Q., Wang, Y., Zhao, W. X., Yan, R., Su, B., Luo, C., and Guo, B. Controlled llm training on spectral sphere, 2026. URL <https://arxiv.org/abs/2601.08393>.
- Xie, X., Zhou, P., Li, H., Lin, Z., and Yan, S. Adan: Adaptive nesterov momentum algorithm for faster optimizing deep models, 2024. URL <https://arxiv.org/abs/2208.06677>.
- Xie, Z., Yin, W., and Wen, Z. Ode-based learning to optimize. *Mathematical Programming*, 2025.
- Yang, A., Yang, B., Hui, B., Zheng, B., Yu, B., Zhou, C., Li, C., Li, C., Liu, D., Huang, F., et al. Qwen2 technical report. *arXiv preprint arXiv:2407.10671*, 2024.
- Yang, Z. and Laaksonen, J. Principal whitened gradient for information geometry. *Neural Networks*, 21(2):232–240, 2008. ISSN 0893-6080.
- Yao, Z., Gholami, A., Keutzer, K., and Mahoney, M. W. Pyhessian: Neural networks through the lens of the hessian. In *2020 IEEE international conference on big data (Big data)*, pp. 581–590. IEEE, 2020.
- Yuan, H., Liu, Y., Wu, S., Xun, Z., and Gu, Q. MARS: Unleashing the power of variance reduction for training large models. In *Forty-second International Conference on Machine Learning*, 2025.
- Zhang, Y., Chen, C., Ding, T., Li, Z., Sun, R., and Luo, Z.-Q. Why transformers need adam: A hessian perspective. In *The Thirty-eighth Annual Conference on Neural Information Processing Systems*, 2024.
- Zhou, P., Feng, J., Ma, C., Xiong, C., Hoi, S. C. H., and E, W. Towards theoretically understanding why sgd generalizes better than adam in deep learning. In *Advances in Neural Information Processing Systems*, volume 33, pp. 21285–21296, 2020.
- Zhou, W., Wang, B., Chen, W., and Cheng, X. Bsfa: Leveraging the subspace dichotomy to accelerate neural network training, 2025. URL <https://arxiv.org/abs/2510.25244>.

# Appendix

---

<b>A</b>	<b>More Related Works</b>	<b>13</b>
<b>B</b>	<b>Algorithm Details</b>	<b>13</b>
B.1	Details of MUON-LITE . . . . .	13
B.2	Details of SOAP-LITE . . . . .	14
<b>C</b>	<b>Experimental Details</b>	<b>15</b>
C.1	Experimental Details in Sections 5.2 . . . . .	16
C.2	Experimental Details in Sections 6 . . . . .	17
<b>D</b>	<b>Additional Experimental Results</b>	<b>18</b>
D.1	Dense Models . . . . .	18
<b>E</b>	<b>Discussions on Momentum Formulations and their Continuous-Time ODE Counterparts</b>	<b>19</b>
E.1	Continuous-Time ODE Formulations . . . . .	19
E.2	Heavy Ball Momentum, Nesterov Momentum, and Hessian Damping . . . . .	19
E.3	Modeling AdEMAMix via a Third-Order ODE . . . . .	21
<b>F</b>	<b>Foundations of Riemannian Geometry</b>	<b>22</b>
F.1	Riemannian Metric . . . . .	22
F.2	The Levi-Civita Connection . . . . .	22
F.3	Riemannian Gradient and Hessian . . . . .	23
<b>G</b>	<b>Transforming the Second Order RISHD (the Riemannian ODE Framework) into a First Order System</b>	<b>24</b>
<b>H</b>	<b>Theoretical Analysis on Quadratic Objectives: An Illustrative Example</b>	<b>25</b>
<b>I</b>	<b>Some Common Adaptive Optimizers for LLM Pre-training</b>	<b>27</b>
I.1	Exact Preconditioner (Riemannian Metrics) Forms for Common Adaptive Optimizers . . . . .	28
<b>J</b>	<b>Proof</b>	<b>29</b>
J.1	Landscape Analysis . . . . .	29
J.2	Dynamics Analysis . . . . .	35
J.3	Useful Lemmas . . . . .	42

## A. More Related Works

**Comparison with methods enhancing dynamics along flat directions.** Recent strategies accelerate LLM pre-training by assigning larger learning rates to flat components. (Wang et al., 2024) adjust learning rates based on an element-wise diagonal Fisher approximation, while (Wang et al., 2025a) apply block-wise learning rates to blocks identified as flat via averaged sharpness. (Zhou et al., 2025) further employs a matrix-level precision subspace detected via a lazy PCA-based estimator. Compared to these methods, LITE identifies flat subspaces with matrix-level precision using highly efficient numerical techniques that introduce no extra optimizer states. Crucially, prior studies focus exclusively on learning rate adjustment, a strategy LITE subsumes by simply setting  $\chi \geq 1$ . In contrast, we **also address the dynamics of momentum** in anisotropic landscapes. We elucidate how momentum and preconditioners jointly influence training dynamics and **enhance momentum evolution** in flat directions by explicitly increasing Hessian damping.

**Comparison with algorithmic frameworks for adaptive optimizers.** Recent works (Pethick et al., 2025; Bernstein & Newhouse, 2024; Xie et al., 2026) interpret the update step of certain adaptive optimizers as the solution to a constrained optimization problem governed by operator norms:

$$U^* = \operatorname{argmin}_{\|U\|_{\text{op}} \leq 1} \langle U, M \rangle, \quad (11)$$

where  $M$  denotes the momentum at the current iterate,  $\langle \cdot, \cdot \rangle$  is the Frobenius inner product, and  $\|\cdot\|_{\text{op}}$  represents a specific operator norm. This formulation formally unifies methods like Muon and Lion, offering insights into their stability (e.g., by controlling the magnitude of activations during propagation). However, a limitation is that the induced geometry is typically independent of the local curvature at the current iterate, making it difficult to encompass methods that decouple momentum and precondition updates like AdamW and SOAP, which rely on iterates-dependent preconditioners. Furthermore, this perspective fails to justify the algorithmic necessity of accumulating momentum before preconditioning. In contrast, our proposed Riemannian ODE framework unifies a broader class of adaptive optimizers. It elucidates the joint role of momentum and preconditioners in shaping training dynamics and extends naturally to complex momentum schemes (see Appendix E.3).

## B. Algorithm Details

### B.1. Details of MUON-LITE

For Muon and MUON-LITE, we adopt the Newton-Schulz (NS) iteration termed Polar Express in (Amsel et al., 2025), and set Newton-Schulz iterations to 6. This approach yields faster convergence to the theoretical optimum than the method in (Jordan et al., 2024).

For the `embedding`, `norm`, `output` blocks, we use the same methods as in SOAP-LITE with  $Q_l = I, Q_r = I$  to estimate the projection  $P_k$  to sharp directions. See more details in Section B.2. Next we introduce how to  $P_k$  for other blocks using MUON-LITE.

**Estimating  $P_k$  via Efficient Composite Newton-Schulz.** To efficiently estimate the sharp subspace projection  $P_k$  at iteration  $k$ , we employ a lightweight composite Newton-Schulz (NS) scheme. The process involves two main steps: constructing a filtering operator and dynamically adjusting the threshold. For any matrix  $A$  with Singular Value Decomposition (SVD)  $A = U\Sigma V^\top$ , We define  $\text{NS}(A) = A(A^\top A)^{-\frac{1}{2}} = UV^\top$ , where the inverse denotes the Moore-Penrose pseudo-inverse.

**1. Construction of the Filtering Operator.** We first define a dynamic threshold  $\tau_k = l_k \|\widetilde{M}_k\|_F$ , where  $l_k$  is a scaling factor. This threshold  $\tau_k$  serves to delineate the sharp subspace: specifically, we select the eigenspace of  $\widetilde{M}_k^\top \widetilde{M}_k$  associated with eigenvalues larger than  $\tau_k$ . The adaptive update mechanism for  $l_k$  (and thus  $\tau_k$ ) will be detailed subsequently. We then compute the filtering operator  $T_k \in \mathbb{R}^{m \times n}$  as:

$$T_k = \frac{1}{2} \text{NS}(\widetilde{M}_k) + \frac{1}{2} \text{NS} \left( \frac{\widetilde{M}_k}{\tau_k} - \text{NS}(\widetilde{M}_k) \right). \quad (12)$$

The projection matrix onto the sharp subspace is subsequently obtained by  $P_k = T_k^\top T_k$ , the rationale for which is detailed in the subsequent parts ((14) and (15)). It is worth noting that this method for estimating  $P_k$  necessitates relatively high

precision from the NS function. Consequently, we employ the Polar Express method (Amsel et al., 2025) rather than the vanilla NS iterations used in (Jordan et al., 2024).

**2. Dynamic Sharp Subspace Dimension Adjustment.** To ensure the rank of the projection  $P_k$  approximates the target dimension  $d_s$ , we update the scaling factor  $l_k$  based on the effective rank (measured by  $\|P_k\|_F^2$ ):

$$l_{k+1} = \begin{cases} 1.05 \cdot l_k, & \text{if } \|P_k\|_F \geq \sqrt{d_s}, \\ 0.95 \cdot l_k, & \text{if } \|P_k\|_F < \sqrt{d_s}. \end{cases} \quad (13)$$

This feedback loop effectively maintains  $\tau_k$  near the  $d_s$ -th largest singular value of  $\widetilde{M}_k$ .

**Theoretical Intuition.** To understand why  $T_k$  acts as a subspace filter, consider the SVD of  $\widetilde{M}_k = U\Sigma V^\top$ . Let the singular values be ordered as  $\sigma_1 \geq \dots \geq \sigma_j > \tau_k > \sigma_{j+1} \geq \dots \geq 0$ . Since the Newton-Schulz iteration converges to the matrix sign function, we have  $\text{NS}(\widetilde{M}_k) = UV^\top$ . Consequently, the input to the second NS term becomes:

$$\frac{\widetilde{M}_k}{\tau_k} - \text{NS}(\widetilde{M}_k) = U \text{diag} \left( \frac{\sigma_1}{\tau_k} - 1, \dots, \frac{\sigma_r}{\tau_k} - 1 \right) V^\top. \quad (14)$$

Applying  $\text{NS}(\cdot)$  to (14) maps positive entries (where  $\sigma_i > \tau_k$ ) to +1 and negative entries (where  $\sigma_i < \tau_k$ ) to -1. Therefore, we have

$$T_k = \frac{1}{2} \text{NS}(\widetilde{M}_k) + \frac{1}{2} \text{NS} \left( \frac{\widetilde{M}_k}{\tau_k} - \text{NS}(\widetilde{M}_k) \right) = U \text{diag}(1, \dots, 1, 0, \dots, 0) V^\top. \quad (15)$$

**Computational Efficiency of MUON-LITE.** Overall, MUON-LITE requires only two additional NS functions per step compared to vanilla Muon, which can be executed in parallel. Since NS iterations constitute a nearly negligible fraction of the computational cost in large-batch pre-training (dominated by gradient computation), this slight overhead is virtually imperceptible in practice. For example, training a LLaMA-1.3B model on the Pile dataset (global batch size 8192, micro batch size 16, sequence length 1024, on  $8 \times$  A800-80GB GPUs) yields a throughput of 100.4k tokens/s for MUON-LITE versus 101.5k tokens/s for Muon. This reflects a throughput drop of only  $\approx 1\%$ . Furthermore, efficiency can be enhanced via system-level optimizations, such as kernel fusion for the NS iterations.

## B.2. Details of SOAP-LITE

In SOAP-LITE, we employ a dynamic thresholding strategy generating a smoothed projection onto the sharp directions to enhance training stability. To avoid the computational latency and memory overhead associated with exact `top-k` operations in PyTorch, especially for large matrices, we approximate the top- $k$  thresholds via adaptive scalar variables, similar to the approach in MUON-LITE. We define  $d_s$  as the target dimension of the sharp subspace, and  $d_{\text{smooth}}$  as the dimension of the transitional subspace bridging the sharp and flat directions. We maintain two dynamic scalars,  $l_k^s$  (controlling the sharp boundary) and  $l_k^{\text{smooth}}$  (controlling the smooth boundary), initialized as  $l_0^s = 1.0$  and  $l_0^{\text{smooth}} = 0.5$ .

At the  $k$ -th iteration, we estimate the thresholds for the top- $d_s$  and top- $(d_s + d_{\text{smooth}})$  elements based on the mean magnitude of the tensor  $V_k$ :  $\tau_k^s = l_k^s \text{mean}(V_k)$  and  $\tau_k^{\text{smooth}} = l_k^{\text{smooth}} \text{mean}(V_k)$ . The smoothed projection matrix  $P_k \in \mathbb{R}^{m \times n}$  is then constructed element-wise as:

$$(P_k)_{i,j} = \begin{cases} 1, & \text{if } (V_k)_{i,j} \geq \tau_k^s, \\ \frac{(V_k)_{i,j} - \tau_k^{\text{smooth}}}{\tau_k^s - \tau_k^{\text{smooth}}}, & \text{if } \tau_k^{\text{smooth}} \leq (V_k)_{i,j} < \tau_k^s, \\ 0, & \text{if } (V_k)_{i,j} \leq \tau_k^{\text{smooth}}. \end{cases} \quad (16)$$

Then we dynamically adjust the coefficients  $l_k^s$  and  $l_k^{\text{smooth}}$  based on the current sparsity levels:

$$l_{k+1}^s = \begin{cases} 1.05 \cdot l_k^s, & |\{V_{i,j} : V_{i,j} > \tau_k^s\}| \geq d_s, \\ 0.95 \cdot l_k^s, & |\{V_{i,j} : V_{i,j} > \tau_k^s\}| < d_s, \end{cases} \quad (17)$$

and

$$l_{k+1}^{\text{smooth}} = \begin{cases} 1.05 \cdot l_k^{\text{smooth}}, & |\{V_{i,j} : V_{i,j} > \tau_k^{\text{smooth}}\}| \geq d_s + d_{\text{smooth}}, \\ 0.95 \cdot l_k^{\text{smooth}}, & |\{V_{i,j} : V_{i,j} > \tau_k^{\text{smooth}}\}| < d_s + d_{\text{smooth}}, \end{cases} \quad (18)$$

where  $|\cdot|$  denotes the cardinality of the set. Finally, we enforce the constraint  $l_{k+1}^{\text{smooth}} \leftarrow \min\{0.95l_{k+1}^s, l_{k+1}^{\text{smooth}}\}$  to ensure that the smoothing threshold remains strictly lower than the sharp threshold ( $l_k^{\text{smooth}} < l_k^s$ ). Our approach eliminates the use of inefficient top- $k$  functions, thereby incurring almost no additional computational or temporal burden.

## C. Experimental Details

**Models.** We utilize two popular classes of LLM models for our pre-training experiments:

- **LLaMA.** LLaMA (Touvron et al., 2023a) is a widely adopted dense decoder-only Transformer architecture. It employs Rotary Positional Embeddings (RoPE) (Su et al., 2024), Swish-Gated Linear Units (SwiGLU), and Root Mean Square Layer Normalization (RMSNorm). In this work, we pre-train LLaMA models with sizes ranging from 130M to 1.3B parameters. Detailed model configurations are provided in Table 2.
- **QwenMoE.** Qwen2MoE (Yang et al., 2024) is a prominent open-source Mixture-of-Experts (MoE) decoder-only Transformer. In contrast to LLaMA, Qwen2MoE integrates a hybrid attention mechanism (combining sliding window and full attention) alongside its MoE architecture. For our experiments, we disable sliding window attention given the relatively short context length. We configure the model to activate 4 experts per token. Auxiliary losses including  $z$ -loss with coefficient 0.001 and load balancing loss with coefficient 0.01 are used to make sure stable training. Refer to Table 3 for comprehensive configuration details.

Table 2. Dense model configurations and optimally-tuned peak learning rates for Muon and SOAP.

Acronym	Size	$d_{\text{model}}$	$d_{\text{FF}}$	n_head	depth	lr_max of Muon	lr_max of SOAP
LLaMA (0.13B)	134M	768	2048	12	12	5e-3 (on C4)	-
LLaMA (0.25B)	247M	768	2560	16	24	3e-3 (on Pile)	3e-3 (on Pile)
LLaMA (0.5B)	518M	1280	3456	20	22	2e-3 (on Pile)	2e-3 (on Pile)
LLaMA (1.3B)	1339M	2048	5461	32	24	1e-3 (on Pile)	-

Table 3. MoE model configurations and optimally-tuned peak learning rates for Muon on Pile.

Acronym	Size	Activated Size	$d_{\text{model}}$	$d_{\text{FF}}$	n_head	depth	n_experts	lr_max
QwenMoE (1B)	1040M	297M	768	3072	12	15	32	2e-3

**Datasets.** We conduct pre-training on the following datasets:

- **C4** (Raffel et al., 2020). The Colossal Clean Crawled Corpus (C4) dataset is employed for our small-to-medium scale pre-training experiments. We use the T5 tokenizer with a vocabulary size of 32,100.
- **The Pile** (Gao et al., 2020). We utilize The Pile for large-scale (or larger-context) pre-training tasks. For this dataset, we adopt the LLaMA-2 tokenizer (Touvron et al., 2023b) with a vocabulary size of 32,000.

**Sequence Packing/Batching.** For the Pile dataset, we employ a standard *sequence packing* strategy: documents are tokenized, concatenated into a continuous stream, and then segmented into fixed-length sequences of size  $L$  (depending on the dataset). This approach minimizes padding overhead and ensures a near-constant number of effective tokens per batch. Training progress is measured in terms of total tokens, with evaluation performed on the official validation splits.

**LR schedulers.** We evaluate two popular learning-rate (LR) scheduling strategies with 1,000 warm-up steps in all pre-training experiments:

- `cos` (cosine scheduler) (Touvron et al., 2023b): a linear warm-up to peak `lr_max`, followed by cosine decay to a terminal LR `lr_min`. Following Hoffmann et al. (2022), we set `lr_min` =  $0.1 \times lr_{max}$ .
- `wsd` (warmup-stable-decay scheduler) (Hu et al., 2024; Hägele et al., 2024): a linear warm-up to `lr_max`, followed by a stable phase keeping LR at `lr_max` (up to 80% of total steps), and then a linear decay to 0 over the final 20% steps.

### C.1. Experimental Details in Sections 5.2

In this subsection, we demonstrate that gradients (first-order information) can effectively approximate the top eigenspaces of the Hessian (second-order information) for matrix block parameters in language models. Similar alignment phenomena have been extensively investigated and verified in simplified models, both theoretically and empirically (Wang & Wu, 2023; Wu et al., 2022). To validate this in our context, we conduct an experiment on a small LLAMA2 model with  $d_{model} = 16$ ,  $d_{model} = 32$ ,  $n_{head} = 4$ ,  $depth = 4$ , vocabulary size = 8, #params = 10,640. The model is trained using AdamW for 100 steps with a token batch size  $8 \times 8 = 64$  and  $lr = 0.001$ . For Q,K,V,O, FFN (up, gate, down) blocks, we compute the Hessian eigenvalue distribution within each block (Figures 2 and 8), test the alignment degree of each row’s Hessian with  $G^\top G$ , and each column’s Hessian with  $GG^\top$  (Figures 2 and 7).

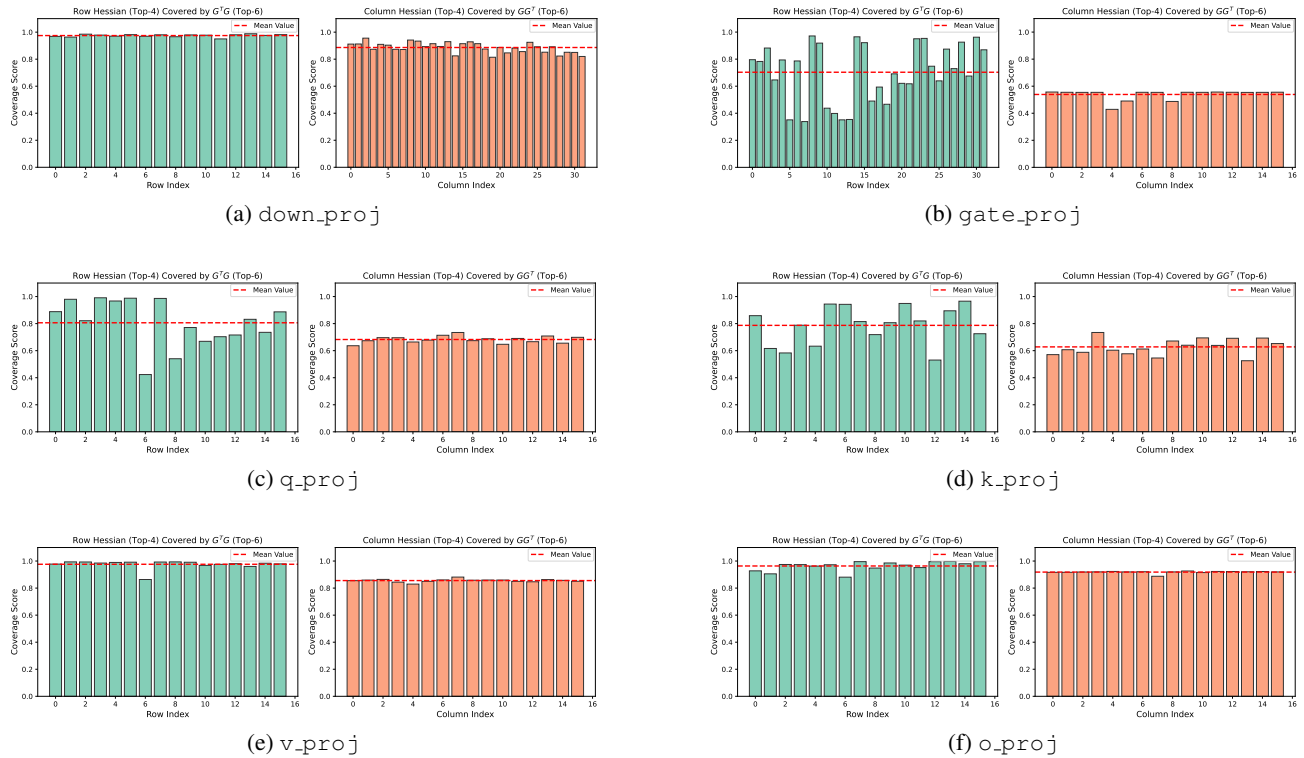


Figure 7. Hessian eigenvalue distribution of different blocks in the toy LLAMA2 model. The results of the `up_proj` are in Figure 2.

**Measure Coverage Degree between Two Subspaces.** Let  $A$  and  $B$  be two linear subspaces of  $\mathbb{R}^d$  with  $\dim(A) \leq \dim(B)$ . Let  $P_A = [u_1, \dots, u_{k_A}] \in \mathbb{R}^{d \times k_A}$  and  $P_B = [v_1, \dots, v_{k_B}] \in \mathbb{R}^{d \times k_B}$  be the matrices consisting of the orthonormal bases of  $A$  and  $B$ , respectively. We define the Coverage Score to quantify the extent to which  $A$  is contained within  $B$ :

$$\text{Coverage Score}(A, B) = \frac{1}{k_A} \|P_A^\top P_B\|_* = \frac{1}{k_A} \sum_{i=1}^{k_A} \cos \theta_i, \quad (19)$$

where  $\|\cdot\|_*$  denotes the nuclear norm, and  $\theta_i$  represent the  $i$ -th principal angle between subspaces  $A$  and  $B$ . By definition, the Coverage Score lies in the interval  $[0, 1]$ . It represents the mean squared norm of the projection of  $A$ ’s basis vectors onto the subspace  $B$ . A score of 1 indicates that  $A \subseteq B$ , while a score of 0 implies that  $A$  is orthogonal to  $B$  ( $A \perp B$ ). A value closer to 1 suggests a higher degree of containment of  $A$  within  $B$ .

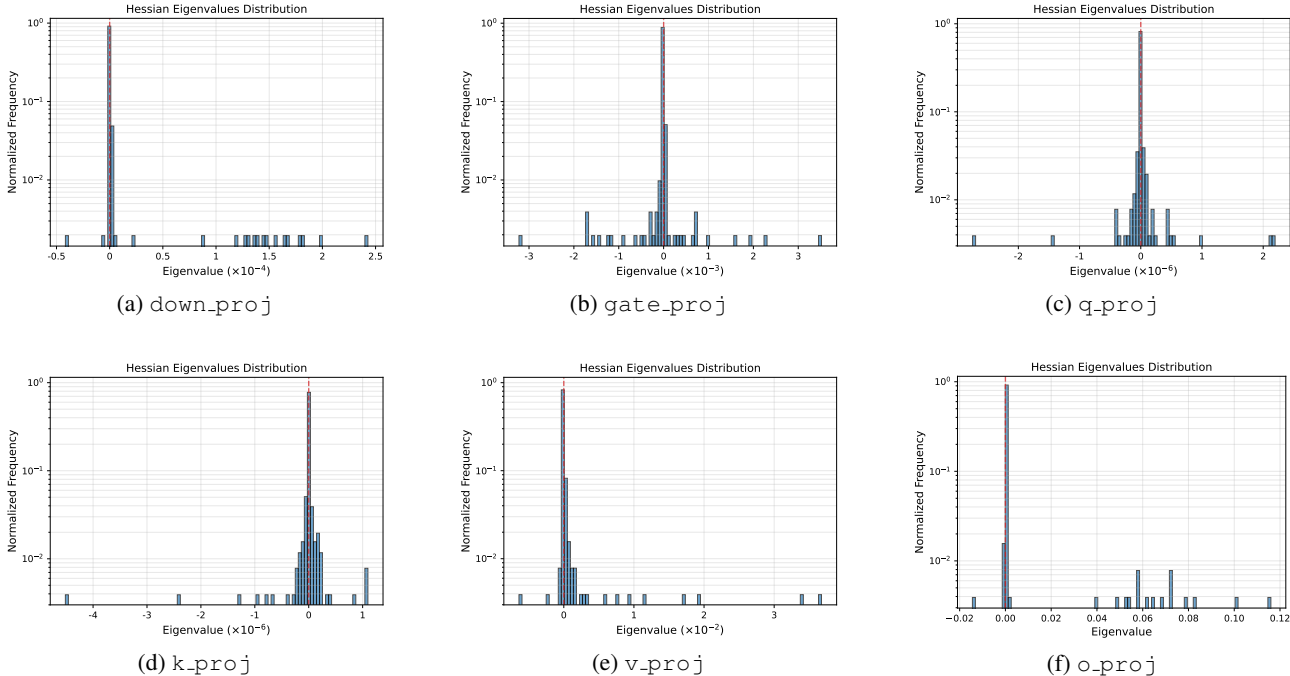


Figure 8. Hessian eigenvalue distribution of different blocks in the toy LLaMA2 model. The results of the up\_proj are in Figure 2.

### C.2. Experimental Details in Sections 6

**Muon Baselines.** We adopt the standard Muon configuration described in (Liu et al., 2025a). Specifically, we apply Muon specifically to 2D matrix blocks within transformer layers, while using AdamW for all other parameters (RMSNorm (norm), Embedding (emb) and the Output (out)). We set the learning rate scaling factor to  $c = 0.2 \max\{m, n\}$  for blocks that use Muon with shape  $\mathbb{R}^{m \times n}$ , ensuring the update RMS norm aligns with that of AdamW. The baseline is configured with Nesterov momentum using a decay coefficient  $\theta_{\text{muon}} = 0.95$ , weight decay  $\lambda = 0.1$ , and a gradient clipping threshold of 1.0.

**SOAP Baselines.** We maintain the same weight decay and gradient clipping settings as in Muon. Following (Vyas et al., 2025), we set the hyper-parameters to  $\theta = 0.95$ ,  $\beta_v = 0.99$ , and  $k = 10$ . regarding the shampoo momentum, although (Vyas et al., 2025) recommends  $\beta_{\text{shampoo}} = 0.99$ , we compared  $\beta_{\text{shampoo}} \in \{0.99, 0.95\}$  and selected 0.95, as it yielded lower validation losses in our experiments.

**Learning Rate Schedules.** For the cos schedule, following Hoffmann et al. (2022), the minimum learning rate lr\_min is set to  $0.1 \times \text{lr}_{\text{max}}$ . For the wsd schedule, we allocate the warmup and stable phases to the first 80% of total iterations, followed by a linear decay to 0 over the remaining 20%. We set the warm-up steps to 1000 for all pre-training experiments.

Additionally,

- **C4 pre-training.** We use a sequence length of 256 and a global batch size of 3,600. The total number of training tokens is set to approximately 80 times the number of model parameters, corresponding to  $4 \times$  the Chinchilla scaling law (Hoffmann et al., 2022). The training process includes 1,000 warm-up steps. We perform a grid search for the maximum learning rate lr\_max over the set  $\{1e-3, 2e-3, 3e-3, 5e-3, 7e-3\}$ . The resulting optimal learning rates for each model are detailed in Table 2.
- **Pile pre-training.** We set the sequence length to 1,024. The batch size is set to 1,024 for the 0.25B and 0.5B models, and 2,048 for the 1.3B model. The total number of training tokens is approximately 40 times the number of model parameters (corresponding to  $4 \times$  the Chinchilla scaling law (Hoffmann et al., 2022)), which includes 1,000 warm-up steps. A grid search for lr\_max is performed over the set  $\{7e-4, 1e-3, 2e-3, 3e-3, 5e-3, 7e-3\}$ . The optimal learning rates for each model are detailed in Tables 2 and 3.

**Hyper-parameter tuning for MUON-LITE.** For LLaMA models, we identified the optimal hyper-parameters  $\{\chi, \beta_1, \beta_2\}$  via grid search on the 250M model (Pile) and applied them uniformly to the 130M (C4), 500M (Pile), and 1.3B (Pile) experiments. Specifically, fixing the base learning rate to Muon’s optimal value, we searched the sharp subspace dimension ration  $r_s \in \{0.1, 0.2\}$ , and set  $d_s = r_s \min\{m, n\}$  for `q`, `k`, `v`, `o`, `ffn` blocks of size  $\mathbb{R}^{m \times n}$ , and  $d_s = r_s mn$  for `emb`, `norm` blocks, with all of them using the same ratio  $r_s$ . The search space for other coefficients is  $\beta_1 \in \{0.0, -0.25\}$ ,  $\beta_2 \in \{0.5, 1.0, 2.0\}$ , and  $\chi \in \{2.0, 4.0\}$ . For AdamW blocks, we set  $\beta_{1,2} = 0.0$  for brevity, and  $d_{\text{smooth}} = 0.1mn$  (the final loss is insensitive to this parameter). Following (Wang et al., 2025a), we exclude the `output` block from LITE (*i.e.* treating the entire block as sharp directions), as accelerating it offers minimal gains and may risk instability. Finally, we selected  $r_s = 0.1$  and the specific settings in LITE variants for LLaMA models are:

- MUON-LITE-H:  $(\beta_1, \beta_2) = (-0.25, 2.0)$ .
- MUON-LITE-L:  $\chi = 4$  for `emb`, `norm` blocks and  $\chi = 2$  for Muon blocks.
- MUON-LITE: Adopts the  $\chi$  settings from MUON-LITE-L and sets  $(\beta_1, \beta_2) = (-0.25, 1.0)$ .

For MUON-LITE in the QwenMoE experiment, we set  $r_s = 0.1$  and  $\beta_1 = 0.0$ . We searched  $\chi \in \{4, 8\}$  for `emb` and `norm` blocks (while maintaining  $\chi = 1$  for others) and  $\beta_2 \in \{1.0, 2.0\}$  for blocks using Muon. The final configuration adopted was  $\chi = 8$  (for `emb/norm`) and  $\beta_2 = 1.0$ .

**Hyper-parameter tuning for SOAP-LITE.** Similar to MUON-LITE, we identified the optimal hyper-parameters  $\{\chi, \beta_1, \beta_2\}$  via grid search on the 250M model (Pile) and applied them to other scenarios. Specifically, fixing the base learning rate to SOAP’s optimal value, we searched the sharp subspace dimension ration  $r_s \in \{0.1, 0.2\}$ , and set  $d_s = r_s mn$  for all blocks, with all of them using the same ratio  $r_s$ . The search space for other coefficients is  $\beta_1 = 0.0$ ,  $\beta_2 \in \{0.25, 0.5, 1.0\}$ , and  $\chi \in \{2.0, 4.0\}$ . We set  $d_{\text{smooth}} = 0.1mn$  uniformly (the final loss is insensitive to this parameter). Following (Wang et al., 2025a), we exclude the `output` block from LITE (*i.e.* treating the entire block as sharp directions), as accelerating it offers minimal gains and may risk instability. Finally, we selected  $r_s = 0.2$  and the specific settings in SOAP-LITE variants for LLaMA models are:

- SOAP-LITE-H:  $(\beta_1, \beta_2) = (0.0, 0.5)$ .
- SOAP-LITE-L:  $\chi = 4$  for `emb`, `norm` blocks and  $\chi = 2$  for Muon blocks.
- SOAP-LITE: Adopts the  $\chi$  settings from SOAP-LITE-L and sets  $(\beta_1, \beta_2) = (0.0, 0.25)$ .

## D. Additional Experimental Results

### D.1. Dense Models

Here we present the supplementary results for the experiments in Section 6.1.

We evaluate the 0-shot performance of the pre-trained LLaMA 1.3B models for 25k steps (Figure 4) in Table 4. MUON-LITE demonstrates consistent improvements over the Muon baseline across the eight evaluated tasks. Notably, MUON-LITE achieves a substantial gain on BoolQ and exhibits strong generalization on reasoning-heavy benchmarks, showing significant margins on ARC-Challenge (+1.79) and MMLU (+1.39). These results indicate that MUON-LITE effectively enhances model performance across diverse domains ranging from common sense reasoning to truthful QA.

Table 4. Evaluation results on downstream tasks (0-shot with lm-evaluation-harness) of LLaMA models (1.3B) pre-trained on Pile using MUON-LITE and Muon. The best scores in each column are bolded. Abbreviations: T\_mc2=TruthfulQA\_mc2, AVG=Average score.

Method	ARC_E	ARC_C	PIQA	HellaSwag	BOOLQ	WinoGrande	MMLU	T_mc2	AVG
Muon	52.99	22.10	67.41	35.30	52.45	53.35	23.76	40.14	43.44
MUON-LITE	<b>54.38</b>	<b>23.89</b>	<b>67.63</b>	<b>36.72</b>	<b>60.52</b>	<b>54.78</b>	<b>25.15</b>	<b>40.83</b>	<b>45.49</b>

## E. Discussions on Momentum Formulations and their Continuous-Time ODE Counterparts

### E.1. Continuous-Time ODE Formulations

In this subsection, we introduce the continuous-time limits of momentum-based algorithms and demonstrate how to derive discrete optimizers from these continuous formulations (modeled as second-order or first-order systems). The derivation proceeds by reducing the second-order dynamics into a first-order system, followed by numerical discretization. This pipeline serves as a foundation for the Riemannian setting (3), which is the primary focus of this work (see Appendix G). We consider the inertial system with Hessian damping (ISHD) mentioned in Section 3.2

$$\ddot{w}_t + \alpha_t \dot{w}_t + \beta_t \nabla^2 f(w_t) \dot{w}_t + \gamma_t \nabla f(w_t) = 0, \quad (20)$$

where  $\alpha_t, \beta_t, \gamma_t \geq 0$  denote the coefficients for momentum decay, Hessian damping, and the gradient driving force, respectively. By introducing an auxiliary momentum variable  $m_t$  to track the velocity  $\dot{w}_t$ , we can reformulate this second-order equation (20) into an equivalent first-order system:

$$\begin{cases} \dot{w}_t = -\gamma_t m_t - \beta_t \nabla f(w_t), \\ \dot{m}_t = -\alpha_t m_t + (1 - \alpha_t \beta_t / \gamma_t - \dot{\beta}_t) \nabla f(w_t). \end{cases} \quad (21)$$

Applying a discretization with step size  $h > 0$  yields the following update rule at the  $k$ -th iteration:

$$\begin{cases} m_k = (1 - \alpha_t h) m_{k-1} + (1 - \alpha_k \beta_k / \gamma_k - \dot{\beta}_k) h \nabla f(w_k), \\ w_{k+1} = w_k - \gamma_k h m_k - \beta_k h \nabla f(w_k). \end{cases} \quad (22)$$

This formulation subsumes various momentum methods, recovering Heavy Ball momentum when  $\beta_k = 0$  and Nesterov-type momentum when  $\beta_k > 0$ . Crucially, the Hessian damping term  $\beta_t \nabla^2 f(w_t) \dot{w}_t$  and its discretized counterpart  $\beta_k \nabla f(w_t)$  serves to enhance standard Heavy Ball momentum by suppressing oscillations. We provide a detailed discussion in Appendix E.2.

### E.2. Heavy Ball Momentum, Nesterov Momentum, and Hessian Damping

In this section, we discuss equivalent formulations of Nesterov-type momentum and Heavy Ball momentum (also known as Polyak momentum). Furthermore, we analyze the acceleration dynamics of Nesterov momentum, highlighting the intrinsic connections between **Hessian damping and gradient correction**. For brevity, we assume the preconditioner is the identity matrix ( $F = I$ ) throughout this discussion.

**Heavy Ball Momentum.** The Heavy Ball momentum update is defined as:

$$\begin{cases} m_k = (1 - \alpha) m_{k-1} + \nabla f(w_k), \\ w_{k+1} = w_k - \eta m_k. \end{cases} \quad (23)$$

This recurrence can be rewritten in a single-variable form equivalent to:

$$w_{k+1} = w_k + (1 - \alpha)(w_k - w_{k-1}) - \eta \nabla f(w_k). \quad (24)$$

This formulation aligns with the momentum schemes adopted in AdamW and many other adaptive optimizers. Note that here, the coefficient  $\alpha$  of the gradient term (typical in EMA-style updates) is absorbed into the effective learning rate  $\eta$ .

**Nesterov Momentum.** Unfortunately, Heavy Ball momentum lacks a theoretical guarantee of globally achieving a faster convergence rate than Gradient Descent, even in deterministic strongly convex settings. In contrast, Nesterov momentum provably achieves acceleration: the convergence rates for Gradient Descent and Nesterov momentum are approximately  $(1 - \frac{1}{\kappa})^k$  and  $(1 - \frac{1}{\sqrt{\kappa}})^k$  respectively, where  $\kappa$  denotes the condition number.

Nesterov momentum with constant coefficients is typically formulated as:

$$\begin{cases} x_k = w_{k-1} - \eta \nabla f(w_{k-1}), \\ w_k = x_k + (1 - \alpha)(x_k - x_{k-1}). \end{cases} \quad (25)$$

Eliminating the auxiliary variable  $x$  or  $w$  yields two equivalent interpretations of (25):

$$x_{k+1} = x_k + (1 - \alpha)(x_k - x_{k-1}) - \underbrace{\eta \nabla f(x_k + (1 - \alpha)(x_k - x_{k-1}))}_{\text{gradient correction}}, \quad (26)$$

and

$$w_{k+1} = w_k + (1 - \alpha)(w_k - w_{k-1}) - \eta \nabla f(w_k) - (1 - \alpha)\eta \underbrace{(\nabla f(w_k) - \nabla f(w_{k-1}))}_{\text{gradient correction}}. \quad (27)$$

**The Gradient Correction (Hessian Damping) Insight.** Comparing (27) with the Heavy Ball form (24), it is evident that Nesterov momentum introduces an additional **gradient correction term**. Using a Taylor expansion, we observe that:

$$\begin{aligned} \nabla f(x_k + (1 - \alpha)(x_k - x_{k-1})) &\approx (1 - \alpha)\nabla^2 f(x_k)(x_k - x_{k-1}), \\ \nabla f(w_k) - \nabla f(w_{k-1}) &\approx \nabla^2 f(w_k)(w_k - w_{k-1}). \end{aligned} \quad (28)$$

This reveals that the gradient correction implicitly incorporates **Hessian information**. This mechanism is the key to the acceleration of Nesterov momentum: it exerts an inertial damping effect (often referred to as Hessian damping) which is proportional to the curvature. Consequently, this term applies stronger damping in directions corresponding to large Hessian eigenvalues, effectively suppressing oscillations.

The formulation in (27) is also mathematically equivalent to:

$$w_{k+1} = w_k + (1 - \alpha)(w_k - w_{k-1}) - \eta_1(1 + \alpha\beta)\nabla f(w_k) - \beta\eta_1(1 - \alpha)\underbrace{(\nabla f(w_k) - \nabla f(w_{k-1}))}_{\text{gradient correction}}. \quad (29)$$

with  $\eta_1 = \eta/(1 + \alpha\beta)$  and  $\beta = 1/(1 - \alpha)$ . Note that (29) can be transformed as:

$$\begin{cases} m_k = (1 - \alpha)m_{k-1} + \nabla f(w_k), \\ w_{k+1} = w_k - \eta_1(m_k + \beta\nabla f(w_k)), \end{cases} \quad (30)$$

which corresponds to the discretized form discussed in Section 3.2.

We can observe that the term  $\beta\nabla f(w_k)$  in (30) (*i.e.* the gradient correction term in (29)) arises from discretizing the Hessian damping term  $\beta\nabla^2 f(w_t)\dot{w}_t$  in Eq. (1).

These insights lead to two key conclusions:

1. **Implicit Hessian Awareness:** Compared with Heavy ball momentum, Nesterov momentum introduces an additional gradient correction term that implicitly encapsulates Hessian information (*i.e.* Hessian damping), which is instrumental in achieving acceleration.
2. **Continuous-Discrete Correspondence:** This gradient correction term naturally arises from the discretization of the Hessian damping term found in the continuous-time limiting flow.

**Further Improving Nesterov momentum** Although Nesterov momentum leverages Hessian damping (via gradient correction) to achieve acceleration, the coefficient  $\beta$  of this term is rigidly constrained by the momentum parameter (*i.e.*  $\beta = 1/(1 - \alpha)$ ). It is therefore natural to relax this constraint and search for an optimal  $\beta$ , a direction supported by recent theoretical results (Attouch et al., 2022; Xie et al., 2025). In this work, we adopt this generalized perspective and incorporate richer second-order information, employing a larger  $\beta$  in flat directions than in sharp directions to further enhance acceleration.

### E.3. Modeling AdEMAMix via a Third-Order ODE

The AdEMAMix optimizer (Pagliardini et al., 2025) builds upon the paradigm of AdamW by incorporating an additional “slow” momentum term. At the  $k$ -th iteration, the parameter update rule is given by:

$$\begin{aligned}
 m_k^{\text{fast}} &= (1 - \alpha_1)m_{k-1}^{\text{fast}} + \alpha_1 g_k, \\
 m_k^{\text{slow}} &= (1 - \alpha_2)m_{k-1}^{\text{slow}} + \alpha_2 g_k, \\
 v_k &= (1 - \beta_{\text{adam}})v_{k-1} + \beta_{\text{adam}} g_k^{\odot 2} \\
 w_{k+1} &= w_k - \eta_k \frac{m_k^{\text{fast}} + \kappa m_k^{\text{slow}}}{v_k},
 \end{aligned} \tag{31}$$

where  $g_k$  denotes the stochastic gradient. For brevity, we omit the weight decay and assume constant momentum hyper-parameters. Typically,  $\alpha_1$  is set to approximately 0.1, while  $\alpha_2$  takes much smaller values, such as  $10^{-4}$ .

To derive its continuous-time version, we first simplify the analysis by omitting the preconditioner  $v_k$  and treating the learning rate  $\eta_k$  as a constant  $\eta$ . This yields the following system of differential equations:

$$\begin{aligned}
 \frac{d}{dt} m_t^{\text{fast}} &= -\alpha_1 m_{k-1}^{\text{fast}} + \alpha_1 \nabla f(w_k), \\
 \frac{d}{dt} m_t^{\text{slow}} &= -\alpha_2 m_{k-1}^{\text{slow}} + \alpha_2 \nabla f(w_k), \\
 \frac{d}{dt} w_t &= -\eta (m_t^{\text{fast}} + \kappa m_t^{\text{slow}}).
 \end{aligned} \tag{32}$$

We note that applying a discretization with step size  $h = 1$  to the above system recovers the update rules in (31). Next, we compute the second and third-order time derivatives of the parameters,  $\frac{d^2}{dt^2} w_t$  and  $\frac{d^3}{dt^3} w_t$ :

$$\begin{aligned}
 \frac{d^2}{dt^2} w_t &= -\eta (-\alpha_1 m_t^{\text{fast}} - \alpha_2 \kappa m_t^{\text{slow}} + (\alpha_1 + \kappa \alpha_2) \nabla f(w_t)), \\
 \frac{d^3}{dt^3} w_t &= -\eta (\alpha_1^2 m_t^{\text{fast}} + \alpha_2^2 \kappa m_t^{\text{slow}} - (\alpha_1^2 + \kappa \alpha_2^2) \nabla f(w_t) + (\alpha_1 + \kappa \alpha_2) \nabla^2 f(w_t) \frac{d}{dt} w_t).
 \end{aligned} \tag{33}$$

By combining (33) with the velocity equation  $\frac{d}{dt} w_t = -\eta (m_t^{\text{fast}} + \kappa m_t^{\text{slow}})$  to eliminate the momentum variables  $m_t^{\text{fast}}$  and  $m_t^{\text{slow}}$ , we arrive at the following third-order ODE :

$$\underbrace{\frac{d^3}{dt^3} w_t}_{\text{jerk}} + (\alpha_1 + \alpha_2) \underbrace{\frac{d^2}{dt^2} w_t}_{\text{accelerated velocity}} + \alpha_1 \alpha_2 \underbrace{\frac{d}{dt} w_t}_{\text{velocity}} + \underbrace{\eta (\alpha_1 + \kappa \alpha_2) \nabla^2 f(w_t) \frac{d}{dt} w_t}_{\text{Hessian damping}} + \underbrace{\eta (1 + \alpha_1 \alpha_2) \nabla f(w_t)}_{\text{gradient}} = 0. \tag{34}$$

Similar to (3), the Riemannian counterpart of (34) can be derived as

$$\nabla_{\dot{w}_t} \nabla_{\dot{w}_t} \dot{w}_t + (\alpha_1 + \alpha_2) \nabla_{\dot{w}_t} \dot{w}_t + \alpha_1 \alpha_2 \frac{d}{dt} \dot{w}_t + \eta (\alpha_1 + \kappa \alpha_2) \frac{d}{dt} \text{grad} f(w_t) + \eta (1 + \alpha_1 \alpha_2) \text{grad} f(w_t) = 0, \tag{35}$$

where we use  $\text{Hess}(w_t) \dot{w}_t = \frac{d}{dt} \text{grad} f(w_t)$ .

**Intuitive Interpretation.** Standard momentum methods (like Heavy Ball) typically correspond to second-order ODEs, describing a particle with mass and friction. In contrast, Eq. (34) reveals that AdEMAMix is governed by a **third-order** dynamics. The term  $\frac{d^3}{dt^3} w_t$  introduces the concept of “jerk” (rate of change of accelerated velocity  $\ddot{w}_t$ ) into the optimization trajectory. The third-order structure with Hessian damping allows the optimizer to regulate not only velocity but also its rate of change across multiple time scales. As a result, transient gradient fluctuations induced by rapidly varying curvature are attenuated before influencing parameter updates, enabling more stable and robust navigation of highly ill-conditioned landscapes.

## F. Foundations of Riemannian Geometry

In this section, we provide a detailed introduction to the foundation for Riemannian Geometry of  $(\mathbb{R}^p, F)$  considered in the main text. The parameter space is the Euclidean space  $\mathbb{R}^p$ , while the metric is the Riemannian metric induced by the preconditioner  $F(w)$ , which is formally denoted as the manifold  $\mathcal{M} = (\mathbb{R}^p, F)$ .

### F.1. Riemannian Metric

The core structure of our framework is based on Riemannian metric, a smooth matrix-value map  $F : \mathcal{M} = \mathbb{R}^p \rightarrow \mathbb{S}_{++}^p$  that assigns an inner product to the tangent space  $T_w\mathcal{M} \cong \mathbb{R}^p$  at each point  $w \in \mathcal{M}$ . For any tangent vectors  $u, v \in T_w\mathcal{M}$ , the inner product is defined as  $\langle u, v \rangle_{F(w)} := u^\top F(w)v$ . This metric induces a norm  $\|u\|_{F(w)} = \sqrt{\langle u, u \rangle_{F(w)}}$  in the tangent space  $T_w\mathcal{M}$ , which measures the magnitude of perturbations  $u$  relative to the local curvature  $F(w)$ .

While the tangent space  $T_w\mathcal{M}$  characterizes velocities or perturbations, its dual, the cotangent space  $T_w^*\mathcal{M}$ , consists of differentials that act linearly on these velocities, naturally representing gradients of functions. Formally,  $T_w^*\mathcal{M}$  is the dual space of  $T_w\mathcal{M}$ , consisting of all linear functionals  $\xi : T_w\mathcal{M} \rightarrow \mathbb{R}$ . It also holds that  $T_w\mathcal{M} \cong \mathbb{R}^p$ . The cotangent space is equipped with the dual norm  $\|u\|_{F(w)^{-1}} = \sqrt{u^\top F(w)^{-1}u}$  for  $u \in T_w^*\mathcal{M}$ . In particular, the Riemannian metric  $F(w)$  induces a natural isomorphism between the tangent and cotangent spaces:

$$F(w) : T_w\mathcal{M} \rightarrow T_w^*\mathcal{M}, \quad F(w)^{-1} : T_w^*\mathcal{M} \rightarrow T_w\mathcal{M}. \quad (36)$$

Under this identification, an element  $\xi \in T_w^*\mathcal{M}$  acts as a linear functional on the tangent space via the Euclidean inner product  $\xi(u) = \xi^\top u$  for  $u \in T_w\mathcal{M}$ . Inner-product structures of  $T_w\mathcal{M}, T_w^*\mathcal{M}$  and between them are  $\langle \cdot, \cdot \rangle_{F(w)}, \langle \cdot, \cdot \rangle_{F(w)^{-1}}, \langle \cdot, \cdot \rangle$  respectively.

Based on the Riemannian metric, we can define the length of a smooth curve  $\gamma : [0, 1] \rightarrow \mathcal{M}$ . The Riemannian length  $L(\gamma)$  is given by integrating the local norm of the velocity vector  $\dot{\gamma}(t)$ :

$$L(\gamma) = \int_0^1 \|\dot{\gamma}(t)\|_{F(\gamma(t))} dt = \int_0^1 \sqrt{\dot{\gamma}(t)^\top F(\gamma(t))\dot{\gamma}(t)} dt. \quad (37)$$

The Riemannian distance (or geodesic distance) between two points  $x, y \in \mathcal{M} = \mathbb{R}^p$  is defined as the infimum of lengths over all piecewise smooth curves connecting them:

$$d_F(x, y) = \inf_{\gamma \in D} L(\gamma), \quad (38)$$

where  $D$  is the set containing all smooth curves  $\gamma$  connecting  $(x, y)$  with  $\gamma(0) = x, \gamma(1) = y$ .

The distance reduces to the Euclidean metric when  $F = I$ . Furthermore, when  $(x, y)$  are sufficiently close locally, we have  $d_F(x, y) \approx \|x - y\|_{F(x)}$ . The Riemannian gradient  $\text{grad } f$  is an example of vector field.

**Smooth Vector Fields and the Tangent Bundle.** With the tangent space  $T_w\mathcal{M}$  defined at each point, we consider the collection of all tangent vectors across the manifold, known as the tangent bundle, denoted by  $T\mathcal{M} := \bigcup_{w \in \mathcal{M}} (\{w\} \times T_w\mathcal{M})$ . The tangent bundle is itself a smooth manifold of dimension  $2p$ . A vector field  $V$  is a mapping (formally called a *section*) that assigns to every point  $w \in \mathcal{M}$  a specific tangent vector  $V(w) \in T_w\mathcal{M}$ . The space of smooth vector fields, denoted by  $\mathcal{C}^\infty(\mathcal{M}, T\mathcal{M})$ , consists of all such fields  $V$  where the assignment varies smoothly with  $w$ . In the global coordinate system of  $\mathcal{M} \cong \mathbb{R}^p$ , any vector field  $V \in \mathcal{C}^\infty(\mathcal{M}, T\mathcal{M})$  can be uniquely expressed as a linear combination of the coordinate basis vectors  $\{\frac{\partial}{\partial w_1}, \dots, \frac{\partial}{\partial w_p}\}$  (which form the standard basis for each  $T_w\mathcal{M}$ ):

$$V(w) = \sum_{i=1}^p v_i(w) \frac{\partial}{\partial w_i}, \quad (39)$$

where each component function  $v_i : \mathcal{M} \rightarrow \mathbb{R}$  is a smooth scalar function. For a function  $f$ ,  $(Vf)|_w := V(w)f(w) = \sum_{i=1}^p v_i(w) \frac{\partial}{\partial w_i} f(w)$  and  $VUf := V(Uf)$  for vector field  $U$ .

### F.2. The Levi-Civita Connection

In Euclidean spaces, comparing vectors at different points is trivial because the tangent spaces are identical. On a curved manifold, tangent spaces  $T_x\mathcal{M}$  and  $T_y\mathcal{M}$  are distinct inner-product spaces. To differentiate vector fields, we require an affine connection  $\nabla$ , which provides a rule for connecting adjacent tangent spaces.

**Definition.** The Levi-Civita connection  $\nabla_{(\cdot)}(\cdot) : \mathcal{C}^\infty(\mathcal{M}, T\mathcal{M}) \times \mathcal{C}^\infty(\mathcal{M}, T\mathcal{M}) \rightarrow \mathcal{C}^\infty(\mathcal{M}, T\mathcal{M})$  is the fundamental connection associated with the metric  $F$ . It is uniquely determined by two geometric conditions:

1. **Torsion-Free:** For any vector fields  $X, Y \in \mathcal{C}^\infty(\mathcal{M}, T\mathcal{M})$ , the connection is symmetric:  $\nabla_X Y - \nabla_Y X = [X, Y]$ , where  $[X, Y]$  is the Lie bracket (in  $\mathbb{R}^p$ , defined by  $[X, Y] = XY - YX$ ).
2. **Metric Compatibility:** The connection preserves the inner product structure. Formally, for vector fields  $X, Y, Z$ :

$$X\langle Y, Z \rangle_F = \langle \nabla_X Y, Z \rangle_F + \langle Y, \nabla_X Z \rangle_F. \quad (40)$$

**Coordinate Representation (Christoffel Symbols).** Since our manifold is globally  $\mathbb{R}^p$ , we can express the covariant derivative explicitly using the standard basis  $\{e_1, \dots, e_p\}$ . Let  $\Gamma_{ij}^k(w)$  denote the Christoffel symbols of the second kind. The covariant derivative of a vector field  $v$  along  $u$  is given component-wise by:

$$(\nabla_u v)_k = \sum_{i=1}^p u_i \frac{\partial v_k}{\partial w_i} + \sum_{i,j \leq p} \Gamma_{ij}^k(w) u_i v_j. \quad (41)$$

The first term captures the standard Euclidean directional derivative, while the second term corrects for the twisting of the coordinate system induced by the metric. The Christoffel symbols are derived from the metric  $F(w)$ :

$$\Gamma_{ij}^k = \frac{1}{2} \sum_l (F^{-1})_{kl} \left( \frac{\partial F_{jl}}{\partial w_i} + \frac{\partial F_{il}}{\partial w_j} - \frac{\partial F_{ij}}{\partial w_l} \right). \quad (42)$$

Here,  $(F^{-1})_{kl}$  denotes the  $(k, l)$ -entry of the inverse metric matrix, and indices denote partial derivatives with respect to coordinates. The Levi-connection would reduce to the Euclidean directional derivative when  $F = I$ , as  $\Gamma_{ij}^k = 0$  in this case.

### F.3. Riemannian Gradient and Hessian

With the metric and connection defined, we can rigorously define the following differential operators.

**Riemannian Gradient.** The Riemannian gradient  $\text{grad}f(w)$  is the unique tangent vector representing the differential  $df(w)$  via the metric:

$$\langle \text{grad}f(w), u \rangle_{F(w)} = df(w)[u] := \lim_{\epsilon \rightarrow 0} \frac{f(w + \epsilon u) - f(w)}{\epsilon} \text{ for any } u \in \mathbb{R}^p. \quad (43)$$

It has the closed form

$$\text{grad}f(w) = F(w)^{-1} \nabla f(w), \quad (44)$$

where  $\nabla f(w)$  is the standard Euclidean gradient. This confirms that the preconditioner  $F^{-1}$  acts as the ‘‘inverse metric’’ mapping cotangent vectors (gradients) to tangent vectors (directions).

**Riemannian Hessian.** The Riemannian Hessian is a linear operator on the tangent space, defined as the covariant derivative of the gradient vector field:

$$\text{Hess}f(w)[u] = \nabla_u \text{grad}f(w), \quad \forall u \in T_w \mathcal{M}. \quad (45)$$

Unlike the Euclidean Hessian  $\nabla^2 f(w)$ , the Riemannian Hessian accounts for the curvature of the manifold. Explicitly:

$$\text{Hess}f(w) = F(w)^{-1} (\nabla^2 f(w) - \mathcal{K}(w)), \quad (46)$$

where

$$[\mathcal{K}(w)]_{ij} = \sum_{k=1}^p \Gamma_{ij}^k(w) \frac{\partial f}{\partial w_k}(w).$$

When  $F(w)$  changes slowly with  $w$ , we have  $\Gamma_{ij}^k \approx 0$  and  $\text{Hess}f(w) \approx F(w)^{-1} \nabla^2 f(w)$ .

## G. Transforming the Second Order RISHD (the Riemannian ODE Framework) into a First Order System

**Lemma G.1.** *Let  $\mathcal{M} = \mathbb{R}^p$  be endowed with a Riemannian metric tensor  $F(w) \succ 0$ . For any vector fields  $u, v \in \mathcal{C}^\infty(\mathcal{M}, T\mathcal{M})$ , we have the following expression for the Levi-Civita connection:*

$$\nabla_u v = \underbrace{\partial_u v}_{\text{Euclidean derivative}} + \underbrace{\frac{1}{2}F^{-1}[(\partial_u F)v + (\partial_v F)u - \nabla_w(u^\top Fv)]}_{\text{Geometric correction}}. \quad (47)$$

*Proof.* By Koszul formula (Corollary 5.11 in (Lee, 2018)), we have

$$2\langle \nabla_u v, h \rangle_F = \partial_u \langle v, h \rangle_F + \partial_v \langle u, h \rangle_F - \partial_h \langle u, v \rangle_F + \langle [u, v], h \rangle_F - \langle [u, h], v \rangle_F - \langle [v, h], u \rangle_F. \quad (48)$$

Substituting

$$\begin{aligned} \partial_u(v^\top Fh) &= (\partial_u v)^\top Fh + v^\top (\partial_u F)h + v^\top F(\partial_u h), \\ \partial_v(u^\top Fh) &= (\partial_v u)^\top Fh + u^\top (\partial_v F)h + u^\top F(\partial_v h), \\ -\partial_h(u^\top Fv) &= -(\partial_h u)^\top Fv - u^\top (\partial_h F)v - u^\top F(\partial_h v), \\ [u, v] &= \partial_u v - \partial_v u, \\ [u, h] &= \partial_u h - \partial_h u, \\ [v, h] &= \partial_v h - \partial_h v, \end{aligned} \quad (49)$$

into (48) yields

$$2h^\top F\nabla_u v = h^\top [2F\partial_u v + (\partial_u F)v + (\partial_v F)u - \nabla_w(u^\top Fv)]. \quad (50)$$

We get the conclusion.  $\square$

**Proposition G.2.** *Let  $\mathcal{M} = \mathbb{R}^d$  be endowed with a Riemannian metric tensor  $F(w) \succ 0$ . Then the RISHD*

$$\nabla_{\dot{w}_t} \dot{w}_t + \alpha_t \dot{w}_t + \beta_t \nabla_{\dot{w}_t} \text{grad} f(w_t) + \gamma_t \text{grad} f(w_t) = 0. \quad (51)$$

with  $\alpha_t = \alpha - \dot{\eta}_t/\eta_t$ ,  $\beta_t = \beta\eta_t$ ,  $\gamma_t = \eta_t(\alpha\beta + 1)$  is equivalent to the following first order system:

$$\begin{cases} \dot{w}_t = -\eta_t F(w_t)^{-1}(m_t + \beta \nabla f(w_t)), \\ \dot{m}_t = -\alpha m_t + \nabla f(w_t) + R_t, \end{cases} \quad (52)$$

where we define  $u_t = m_t + \beta \nabla f(w_t)$  and

$$\begin{aligned} R_t &= -\frac{\eta_t}{2} \nabla_w(u_t^\top F(w_t)u_t) + \frac{\beta\eta_t}{2} (\nabla F(w_t)[F^{-1}(w_t)u_t]F^{-1}(w_t)\nabla f(w_t) - \nabla F(w_t)[F^{-1}(w_t)\nabla f(w_t)]F^{-1}(w_t)u_t) \\ &\quad + \frac{\beta\eta_t}{2} \nabla F(w_t)[F^{-1}(w_t)u_t]F^{-1}(w_t)\nabla f(w_t). \end{aligned} \quad (53)$$

*Remark G.3.* (53) is equivalent to (3) as  $\nabla_{\dot{w}_t} \text{grad} f(w_t) = \text{Hess}(w_t)\dot{w}_t$ .

*Proof.* First, we let  $m_t = -F(w_t)\dot{w}_t/\eta_t - \beta \nabla f(w_t)$  and get

$$\begin{aligned} \dot{w}_t &= -\eta_t F(w_t)^{-1}(m_t + \beta \nabla f(w_t)), \\ \dot{w}_t &= -\dot{\eta}_t F(w_t)^{-1}(m_t + \beta \nabla f(w_t)) - \eta_t \frac{d}{dt} F(w_t)^{-1}(m_t + \beta \nabla f(w_t)) - \eta_t F(w_t)^{-1}(\dot{m}_t + \beta \nabla^2 f(w_t)\dot{w}_t). \end{aligned} \quad (54)$$

By Lemma G.1, we have

$$\nabla_{\dot{w}_t} \dot{w}_t = \ddot{w}_t + F(w_t)^{-1} \dot{F}(w_t) \dot{w}_t - \frac{1}{2} F^{-1}(w_t) \nabla_w (\dot{w}_t^\top F(w) \dot{w}_t)|_{w=w_t}, \quad (55)$$

and

$$\begin{aligned}
 \nabla_{\dot{w}_t} \text{grad } f(w_t) &= \nabla_{\dot{w}_t} (F^{-1}(w_t) \nabla f(w_t)) \\
 &= \frac{d}{dt} (F^{-1}(w_t)) \nabla f(w_t) + F^{-1}(w_t) \nabla^2 f(w_t) \dot{w}_t + \frac{1}{2} F^{-1}(w_t) \frac{d}{dt} F(w_t) F^{-1}(w_t) \nabla f(w_t) \\
 &\quad + \frac{1}{2} F^{-1}(w_t) \nabla F(w_t) [F^{-1}(w_t) \nabla f(w_t)] \dot{w}_t - \frac{1}{2} F^{-1}(w_t) \nabla_w (\dot{w}_t^\top F(w) F^{-1}(w_t) \nabla f(w_t))|_{w=w_t} \\
 &= F^{-1}(w_t) \nabla^2 f(w_t) \dot{w}_t - \frac{1}{2} F^{-1}(w_t) \frac{d}{dt} F(w_t) F^{-1}(w_t) \nabla f(w_t) \\
 &\quad + \frac{1}{2} F^{-1}(w_t) \nabla F(w_t) [F^{-1}(w_t) \nabla f(w_t)] \dot{w}_t - \frac{1}{2} F^{-1}(w_t) \nabla_w (\dot{w}_t^\top F(w) F^{-1}(w_t) \nabla f(w_t))|_{w=w_t}.
 \end{aligned} \tag{56}$$

Substituting them into (51) yields

$$\begin{aligned}
 \dot{m}_t &= -\alpha m_t + \nabla f(w_t) - \frac{\eta_t}{2} \nabla_w (u_t^\top F(w_t) u_t) - \frac{\beta}{2} \nabla F(w_t) [\dot{w}_t] F^{-1}(w_t) \nabla f(w_t) + \frac{\beta}{2} \nabla F(w_t) [F^{-1}(w_t) \nabla f(w_t)] \dot{w}_t \\
 &\quad - \frac{\beta}{2} \nabla F(w_t) [\dot{w}_t] F^{-1}(w_t) \nabla f(w_t).
 \end{aligned} \tag{57}$$

We get the conclusion.  $\square$

*Remark G.4.* In general, we assume that  $F(w)$  varies slowly with respect to  $w$  to ensure the stability of the preconditioner. This assumption is practically justified by the common use of Exponential Moving Average (EMA) with a decay coefficient close to 1, which enforces a smooth evolution of the estimated preconditioner. Consequently, based on the expression of  $R_t$  in (53), this term is typically negligible relative to  $m_t$  and  $\nabla f(w_t)$ , as it scales with the small step size  $\eta_t$  and the limited variation  $\|\nabla F(w)\|_{\text{op}}$ .

## H. Theoretical Analysis on Quadratic Objectives: An Illustrative Example

To elucidate the acceleration mechanism of LITE, we analyze the discrete-time dynamics of the update rule (2), which corresponds to non-accelerated adaptive optimizers, on a quadratic objective function:

$$f(w) = \frac{1}{2} \sum_{i=1}^p \lambda_i w_i^2 + b^\top w. \tag{58}$$

We assume the eigenvalues are sorted as  $\lambda_1 > \dots > \lambda_k > 0 \geq \dots \geq \lambda_p$ , representing an anisotropic landscape where negative  $\lambda_i$  correspond to local nonconvex directions. For simplicity, we set the step size  $h = 1$  and the preconditioner  $F(w) = I_p$ . Since the Hessian is diagonal, the dynamics decouple across coordinates.

Let  $w_\star = -[b_1/\lambda_1, \dots, b_p/\lambda_p]^\top$  denote the stationary point. To characterize the trajectory of the error term  $e_k = w_k - w_\star$ , we eliminate the auxiliary momentum variable  $m_k$ . From (2) with  $F = I_p$ , the  $i$ -th coordinate of  $m_k$  can be expressed in terms of  $e_k$  as:

$$\eta(m_k)_i = (1 - \eta\beta\lambda_i)(e_k)_i - (e_{k+1})_i, \quad 1 \leq i \leq p. \tag{59}$$

Applying a time shift to (59), we obtain:

$$\eta(m_{k-1})_i = (1 - \eta\beta\lambda_i)(e_{k-1})_i - (e_k)_i. \tag{60}$$

Combining these relations leads to a homogeneous second-order linear recurrence:

$$(e_{k+1})_i - 2T_i(e_k)_i + D_i(e_{k-1})_i = 0, \tag{61}$$

where the coefficients are defined as:

$$T_i = T(\lambda_i) := 1 - \frac{\alpha + \eta\lambda_i(\beta + 1)}{2}, \quad D_i = D(\lambda_i) := (1 - \alpha)(1 - \eta\beta\lambda_i). \tag{62}$$

The characteristic equation is given by  $r^2 - 2T_i r + D_i = 0$ , with roots:

$$r_{i,1,2} = T_i \pm \sqrt{T_i^2 - D_i}. \quad (63)$$

Based on the discriminant  $\Delta_i = T_i^2 - D_i$ , the dynamics fall into three regimes, yielding the following closed-form solutions ( $c_{i,1}, c_{i,2}$  are constants determined by initialization):

$$w_{k,i} = -\frac{b_i}{\lambda_i} + \begin{cases} c_{i,1}r_{i,1}^k + c_{i,2}r_{i,2}^k, & \Delta_i > 0 \text{ (Overdamped)}, \\ (c_{i,1} + c_{i,2}k)D_i^{k/2}, & \Delta_i = 0 \text{ (Critically damped)}, \\ D_i^{k/2} [c_{i,1} \cos(k\theta_i) + c_{i,2} \sin(k\theta_i)], & \Delta_i < 0 \text{ (Underdamped)}, \end{cases} \quad (64)$$

where  $\theta_i = \arccos(T_i/\sqrt{D_i})$ .

**Stability Analysis.** Convergence in convex directions requires the magnitude of all characteristic roots to be at most 1. According to the Jury Stability Criterion, the necessary and sufficient conditions are  $|P_i(0)| \leq 1$ ,  $P_i(1) \geq 0$ , and  $P_i(-1) \geq 0$ , where  $P_i(z) = z^2 - 2T_i z + D_i$ . Solving these inequalities yields the stability bound:

$$\eta \leq \frac{2(2 - \alpha)}{\lambda_1 \max\{1 + 2\beta - \alpha\beta, 2\beta(1 - \alpha)\}}. \quad (65)$$

Ideally, this condition confirms that the maximum allowable step size is governed by the sharpest direction  $\lambda_1$ .

**Regime Classification.** We next analyze how the curvature  $\lambda_i$  determines the dynamic regime. The equation  $T(\lambda)^2 = D(\lambda)$  with respect to  $\lambda$ :

$$\left(1 - \frac{\alpha + \eta\lambda(\beta + 1)}{2}\right)^2 = (1 - \alpha)(1 - \eta\beta\lambda) \quad (66)$$

possesses two real positive roots, denoted  $\tilde{\lambda}_1 < \tilde{\lambda}_2$ . By the properties of quadratic functions, we refer eigenvalues  $\lambda$  satisfying  $\lambda < \tilde{\lambda}_1$  to *flat directions (parts)*, which fall into the **overdamped regime**. Conversely, eigenvalues  $\lambda \geq \tilde{\lambda}_1$  correspond to *sharp directions*, whose dynamic regimes depend on the specific magnitude of the curvature (typically transitioning into the underdamped regime).

**Acceleration Mechanism of LITE.** Here we suppose that the stability condition (65) holds. Since LITE explicitly increases  $\eta$  and  $\beta$  in flat directions, we focus our analysis on the regime  $\lambda_i < \tilde{\lambda}_1$ . In this regime, the dynamics are overdamped, and dominated by the larger root  $r_1 = T + \sqrt{T^2 - D}$ . We demonstrate that our parameter adjustment modifies  $r_1$  to facilitate escape from nonconvex regions and foster convergence in convex regions.

We analyze the sensitivity of  $r_1$  to  $\beta$  and  $\eta$  case by case:

- **Case 1: Flat Nonconvex Directions** ( $\lambda < 0$ ). The coefficients become  $T = 1 - \frac{\alpha}{2} + \frac{\eta|\lambda|(\beta+1)}{2}$  and  $D = (1 - \alpha)(1 + \eta\beta|\lambda|)$ . Clearly,  $T > 1 - \alpha$ , and both  $T$  and  $D$  are strictly increasing functions of  $\beta$  and  $\eta$ . Consider the partial derivatives:

$$\frac{\partial r_1}{\partial \beta} = \frac{\partial T}{\partial \beta} + \frac{1}{2\sqrt{T^2 - D}} \left(2T \frac{\partial T}{\partial \beta} - \frac{\partial D}{\partial \beta}\right). \quad (67)$$

Since  $T > 0$ , and noting that:

$$2T \frac{\partial T}{\partial \beta} - \frac{\partial D}{\partial \beta} = T\eta|\lambda| - (1 - \alpha)\eta|\lambda| > 0, \quad (68)$$

(and similarly for  $\eta$ ), we conclude that increasing  $\beta$  or  $\eta$  yields a strictly larger  $r_1$  (with  $r_1 > 1$ ). This increases the exponential divergence rate along negative curvature directions, thereby facilitating rapid escape.

- **Case 2: Flat Convex Directions** ( $0 < \lambda < \tilde{\lambda}_1$ ). In this regime, the convergence rate is governed by how quickly  $r_1$  decays to zero. To accelerate convergence, we must **minimize**  $r_1$ . The coefficients are  $T = 1 - \frac{\alpha + \eta\lambda(\beta+1)}{2}$  and  $D = (1 - \alpha)(1 - \eta\beta\lambda)$ . Observing the monotonicity:

$$\frac{\partial T}{\partial \beta} < 0, \quad \frac{\partial D}{\partial \beta} < 0 \quad (\text{and similarly for } \eta). \quad (69)$$

Both  $T$  and  $D$  decrease monotonically as  $\beta$  or  $\eta$  increases. Since  $r_1$  is strictly increasing with respect to  $T$  and  $D$ , the dominant root  $r_1$  decreases when  $\beta$  (or  $\eta$ ) increases. This reduction in the spectral radius directly fosters faster convergence.

## I. Some Common Adaptive Optimizers for LLM Pre-training

Here we list some common optimizers in LLM pre-training. They can be subsumed by discretizing the ODE framework (2). We omit gradient clipping and AdamW-type bias correction coefficient  $\frac{1-\theta^t}{\sqrt{1-\beta_v^t}}$  for notational brevity.

---

### Algorithm 2 AdamW

---

**Require:** Hyper-parameters:  $\theta, \beta_v, \epsilon, \{\eta_t\}, \lambda$   
 Initialize  $m = 0, v = 0, t = 0$   
**for**  $t = 1, 2, \dots$  **do**  
     Compute stochastic gradient  $g_t$  at current parameters  $w_t$ .  
      $m_t = \theta m_{t-1} + (1 - \theta)g_t$   
      $v_t = \beta_v v_{t-1} + (1 - \beta_v)g_t^{\odot 2}$   
      $w_{t+1} = w_t - \eta_t \left( \frac{m_t}{\sqrt{v_t + \epsilon}} + \lambda w_t \right)$   
**end for**

---



---

### Algorithm 3 Lion

---

**Require:**  $\theta, \beta_v, \{\eta_t\}, \epsilon, \lambda$   
 Initialize  $m = 0$   
**for**  $t = 1, 2, \dots$  **do**  
     Compute gradient  $g_t$  at current parameters  $w_t$   
      $u_t = \theta m_{t-1} + (1 - \theta)g_t$   
      $m_t = \beta_v m_{t-1} + (1 - \beta_v)g_t$   
      $w_{t+1} = w_t - \eta_t \text{sign}(u_t) - \eta_t \lambda w_t$   
**end for**

---



---

### Algorithm 4 MARS

---

**Require:**  $\theta, \beta_v, \gamma, \epsilon, \{\eta_t\}, \lambda$   
 Initialize  $m = 0, v = 0, g_0 = 0$   
**for**  $t = 1, 2, \dots$  **do**  
     Compute stochastic gradient  $g_t$  at current parameters  $w_t$   
      $c_t = g_t + \gamma \frac{\theta}{1 - \theta} (g_t - g_{t-1})$   
      $m_t = \theta m_{t-1} + (1 - \theta)c_t$   
      $v_t = \beta_v v_{t-1} + (1 - \beta_v)c_t^{\odot 2}$   
      $w_{t+1} = w_t - \eta_t \frac{m_t}{\sqrt{v_t + \epsilon}} - \eta_t \lambda w_t$   
**end for**

---

*Remark I.1.* In MARS, the momentum term is updated as:

$$m_t = \theta m_{t-1} + (1 - \theta)g_t + \gamma \theta (g_t - g_{t-1}). \quad (70)$$

It can be transformer to the formulation in (2) as:

$$s_t = \theta s_{t-1} + g_t, \quad \tilde{m}_t = s_t + \frac{\gamma}{(1 - \gamma)(1 - \theta)} g_t, \quad (71)$$

with  $m_t = (1 - \gamma)(1 - \theta)\tilde{m}_t$ . Note that  $\gamma \neq 1$ ; otherwise, (70) would reduce to  $m_t = \theta m_{t-1} + \theta g_{t-1}$ , thereby completely discarding the current gradient information  $g_t$ .

**Algorithm 5** Muon

---

**Require:**  $\theta_{\text{muon}}, \eta, \epsilon, \theta_{\text{adamw}}, \beta_v, \{\eta_t\}, \lambda$   
 Initialize state  $m$   
**for**  $t = 1, 2, \dots$  **do**  
     **For weights in Output, Embedding, and Norm layers:**  
         Update using AdamW with hyper-parameters  $\theta_{\text{adamw}}, \beta_v, \epsilon, \eta_t, \lambda$ .  
     **For weight matrices in transformer layers:**  
         Compute stochastic gradient  $g_t$  at current parameters  $w_t$   
          $m_t = \theta_{\text{muon}}m_{t-1} + g_t$   
          $u_t = \theta_{\text{muon}}m_t + g_t$   
          $w_{t+1} = w_t - \text{scale} \cdot \eta_t \text{NS}(u_t) - \eta_t \lambda w_t$ , where  $\text{scale} = 0.2\sqrt{\max\{m, n\}}$  for  $w \in \mathbb{R}^{m \times n}$ .  
**end for**

---

**Algorithm 6** SOAP

---

**Require:**  $\theta, \beta_v, \beta_{\text{shampoo}}, k, \epsilon, \lambda$   
 Initialize state:  $m = 0, v = 0, L = 0, R = 0, Q_l, Q_r$   
**for**  $t = 1, 2, \dots$  **do**  
     **For weights in Output, Embedding, and Norm layers:**  
         Update using AdamW with hyper-parameters  $\beta_1, \beta_2, \epsilon, \eta_t, \lambda$ .  
     **for weight matrices in transformer layers: do**  
         Compute stochastic gradient  $G_t$  at current parameters  $W_t$   
          $G_t^{\text{rot}} = Q_l^\top G_t Q_r$   
          $M_t = \theta M_{t-1} + (1 - \theta)G_t$   
          $V_t = \beta_v V_{t-1} + (1 - \beta_v)(G_t^{\text{rot}})^{\odot 2}$   
          $W_{t+1} = W_t - \eta_t Q_l \left( \frac{Q_l^\top M_t Q_r}{\sqrt{V_t} + \epsilon} \right) Q_r^\top - \eta_t \lambda W_t$   
          $L_t = \beta_{\text{shampoo}} L_{t-1} + (1 - \beta_{\text{shampoo}})G_t G_t^\top$   
          $R_t = \beta_{\text{shampoo}} R_{t-1} + (1 - \beta_{\text{shampoo}})G_t^\top G_t$   
         **if**  $t \bmod k = 0$  **then**  
              $Q_l \leftarrow \text{QR}(L_t Q_l)$  {QR decomposition}  
              $Q_r \leftarrow \text{QR}(R_t Q_r)$   
         **end if**  
     **end for**  
**end for**

---

**1.1. Exact Preconditioner (Riemannian Metrics) Forms for Common Adaptive Optimizers**

In this section, we analyze the implicit metric structure  $F$  induced by the preconditioner estimation (update) scheme for each parameter block, and compare the way in approximating  $\hat{F}(w) = (\mathbb{E}[gg^\top])^{1/2}$  in Section 4.1.

Let  $G \in \mathbb{R}^{m \times n}$  denote the stochastic gradient in matrix form, and let  $g = \text{vec}(G) \in \mathbb{R}^{mn}$  be its vectorized counterpart. The Fisher-type metric  $\hat{F}(w) = (\mathbb{E}[gg^\top])^{1/2} \in \mathbb{R}^{mn \times mn}$  is often referred to the Whitening metric (Yang & Laaksonen, 2008; Frans et al., 2025), which has demonstrated efficient and stable performance in neural network training. Below, we demonstrate how practical inverse preconditioners  $F_k$  in common adaptive optimizers approximate their corresponding deterministic forms  $F(w_k)$ , which in turn serve as approximations of  $\hat{F}(w_k)$ . Throughout, we utilize the identity  $\text{vec}(ABC) = (C^\top \otimes A) \text{vec}(B)$ .

**EMA-based Preconditioners.** AdamW employs an Exponential Moving Average (EMA) to update its preconditioner  $F_k^{-1}$  via  $F_k = \text{diag } v_k^{1/2}$  with  $v_k = \beta_v v_{k-1} + (1 - \beta_v)g_k \odot g_k$ . This expands to  $v_k = (1 - \beta_v) \sum_{i=0}^k \beta_v^{k-i} g_i \odot g_i$ , where  $\beta_v$  is typically close to 1. Observing that  $(1 - \beta_v) \sum_{i=k-t}^k \beta_v^{k-i} \approx 1$  for a large window  $t$ , and assuming that the stochastic gradients  $g_i$  are approximately independent samples while  $\hat{F}(w)$  changes slowly with respect to  $w$ , we can deduce that  $v_k^{1/2}$  provides a stable and efficient approximation of  $F^{\text{adam}}(w) = \text{diag } \hat{F}(w)$ . This approximation logic can directly extend to

other optimizers that accumulate preconditioners via EMA, such as SOAP. Specifically, for SOAP, from Algorithm 6 we have

$$F_k = (Q_r \otimes Q_l) (\text{diag vec}(V_k))^{\frac{1}{2}} (Q_r \otimes Q_l)^\top, \text{ with } V_k = \beta_v V_{k-1} + (1 - \beta_v)(G_k^{\text{rot}})^{\odot 2}, \quad (72)$$

where  $Q_l, Q_r$  are updated in a lazy fashion, and  $G_k^{\text{rot}} = Q_l^\top G_k Q_r$ . This gives

$$F^{\text{soap}}(w) = (Q_r \otimes Q_l) (\text{diag } \mathbb{E}[g_{\text{rot}} g_{\text{rot}}^\top])^{\frac{1}{2}} (Q_r \otimes Q_l)^\top, \quad (73)$$

where  $Q_l$  and  $Q_r$  are the eigenvectors of  $\mathbb{E}[GG^\top]$  and  $\mathbb{E}[G^\top G]$ , respectively, and  $g_{\text{rot}} = \text{vec}(Q_l^\top G Q_r)$ . Thus,  $F^{\text{soap}}(w)$  approximates  $\hat{F}(w)$  via a structured, two-sided Kronecker factorization.

**Momentum-based Preconditioners.** We take Muon as a representative example. At the  $k$ -th iteration, the momentum is updated as  $M_k = \theta_{\text{muon}} M_{k-1} + G_k$ , where  $G_k \in \mathbb{R}^{m \times n}$  (assuming  $m \geq n$ ). We have  $F_k = (M_k^\top M_k)^{1/2} \otimes I_m$  (or replacing  $M_k$  with its Nesterov-accelerated version). Expanding this recurrence yields  $M_k = \sum_{i=0}^k \theta_{\text{muon}}^{k-i} G_i$ . Analyzing the second moment, we have:

$$\mathbb{E}[M_k^\top M_k] = \sum_{i,j \leq k} \theta_{\text{muon}}^{2k-(i+j)} \mathbb{E}[G_i^\top G_j] \approx \sum_{i=0}^k \theta_{\text{muon}}^{2(k-i)} \mathbb{E}[G_i^\top G_i]. \quad (74)$$

Here, we assume that in the middle to late stages of training, the deterministic gradient component is negligible compared to the stochastic noise (or second moment magnitude), and that gradient noise is approximately independent across different steps  $i, j$  ( $i \neq j$ ). Applying the same EMA perspective as used for AdamW,  $M_k^\top M_k$  serves as a stable estimator of  $\frac{1}{1-\theta_{\text{muon}}^2} \mathbb{E}[G^\top G]$ . Similarly, for the Nesterov-corrected momentum  $\tilde{M}_k = M_k + G_k/(1 - \theta_{\text{muon}})$ , we can similarly get that  $\tilde{M}_k^\top \tilde{M}_k$  approximates  $c \mathbb{E}[G^\top G]$  for some constant scaling factor  $c$ . Consequently, the implicit metric for Muon can be characterized as  $F^{\text{muon}}(w) \propto (\mathbb{E}[G^\top G])^{\frac{1}{2}} \otimes I_m$ , representing a single-sided Kronecker-factored approximation of  $\hat{F}(w)$ . This derivation extends naturally to element-wise operations on momentum; for instance, Lion's update rule implies a metric  $F^{\text{lion}}(w) \propto \text{diag}(\hat{F}(w))$ .

## J. Proof

**Notations** A map is said to be smooth if it is infinitely differentiable. For notational brevity, we define  $F_s(w) = P_s(w)F(w)P_s(w)$ ,  $F_f(w) = P_f(w)F(w)P_f(w)$  and the corresponding pseudo inverse  $F_s^\dagger(w) = P_s(w)F^{-1}(w)P_s(w)$ ,  $F_f^\dagger(w) = P_f(w)F^{-1}(w)P_f(w)$ . Denote  $\kappa_{F_s} := \rho/\lambda_{F_s}$ ,  $\kappa_F := \rho/\lambda_F$ . The full version of Assumption 7.2.2 concerning the operator norm bounds on  $\nabla P_s$  and  $\nabla F$  is as follows. For any  $u, v, w \in \mathbb{R}^p$ , we have

$$\begin{aligned} \|\nabla P_s(w)[u]v\|_{F(w)} &\leq \frac{\delta}{G} \|u\|_{F(w)} \|v\|_{F(w)}, \\ \|\nabla F(w)[u]v\|_{F^{-1}(w)} &\leq \frac{\delta_F}{G} \|u\|_{F(w)} \|v\|_{F(w)}. \end{aligned} \quad (75)$$

### J.1. Landscape Analysis

In this subsection we mainly focus on properties of  $\Phi$  and  $\mathcal{R}$ .

**Lemma J.1.** *Suppose that Assumptions 7.2 holds. Define  $\delta_{F_s} = 2\delta + \delta_F$ . Then we have*

$$\max\{\|\nabla F_s^\dagger(w)[u]v\|_{F(w)}, \|\nabla F_f^\dagger(w)[u]v\|_{F(w)}\} \leq \frac{\delta_{F_s}}{G} \|u\|_{F(w)} \|v\|_{F^{-1}(w)}, \quad (76)$$

$$\max\{\|\nabla F_s(w)[u]v\|_{F(w)}, \|\nabla F_f(w)[u]v\|_{F(w)}\} \leq \frac{\delta_{F_f}}{G} \|u\|_{F(w)} \|v\|_{F(w)}. \quad (77)$$

*Proof.* By (75), we have

$$\begin{aligned}
 v^\top \nabla (P_s F^{-1} P_s)(w)[u]v &= 2v^\top \nabla P_s(w)[u]F^{-1}(w)P_s(w)v + v^\top P_s(w)\nabla(F^{-1})(w)[u]P_s(w)v \\
 &\leq 2\|v\|_{F(w)^{-1}}\|\nabla P_s(w)[u]F(w)^{-1}P_s(w)v\|_{F(w)} \\
 &\quad + \|P_s(w)F(w)^{-1}v\|_{F(w)}\|\nabla F(w)[u]F(w)^{-1}P_s(w)v\|_{F(w)^{-1}} \\
 &\leq \frac{\delta_{F_s}}{\|\nabla f(w)\|_{F(w)^{-1}}}\|v\|_{F(w)^{-1}}\|v\|_{F_s^\dagger(w)}\|u\|_{F(w)},
 \end{aligned} \tag{78}$$

where the first inequality uses  $\nabla(F^{-1})(w)[u] = -F^{-1}(w)\nabla F(w)[u]F^{-1}(w)$ .

Similarly, for any  $p$ ,

$$\begin{aligned}
 &p^\top \nabla (P_s F P_s)(w)[u]v \\
 &= p^\top \nabla P_s(w)[u]F(w)P_s(w)v + p^\top P_s(w)F(w)\nabla P_s(w)[u]v + p^\top P_s(w)\nabla F(w)[u]P_s(w)v \\
 &\leq \|\nabla P_s(w)[u]v\|_{F(w)}\|F(w)P_s(w)p\|_{F(w)^{-1}} + \|\nabla P_s(w)[u]p\|_{F(w)}\|F(w)P_s(w)v\|_{F(w)^{-1}} \\
 &\quad + \|P_s(w)p\|_{F(w)}\|\nabla F(w)[u]P_s(w)v\|_{F(w)^{-1}} \\
 &\leq \frac{\delta(\|v\|_{F_s(w)}\|p\|_{F(w)} + \|v\|_{F(w)}\|p\|_{F_s(w)}) + \delta_F\|v\|_{F_s(w)}\|p\|_{F_s(w)}}{\|\nabla f(w)\|_{F(w)^{-1}}}\|u\|_{F(w)}.
 \end{aligned} \tag{79}$$

□

Using  $\nabla P_f = -\nabla P_s$ , we can similarly get

$$v^\top \nabla (P_f F^{-1} P_f)(w)[u]v \leq \frac{\delta_{F_s}}{\|\nabla f(w)\|_{F(w)^{-1}}}\|v\|_{F(w)^{-1}}\|v\|_{F_f^\dagger(w)}\|u\|_{F(w)}, \tag{80}$$

and

$$v^\top \nabla (P_f F P_f)(w)[u]v \leq \frac{\delta_{F_s}}{\|\nabla f(w)\|_{F(w)^{-1}}}\|v\|_{F(w)}\|v\|_{F_f(w)}\|u\|_{F(w)}. \tag{81}$$

**Lemma J.2.** *Suppose Assumptions 7.1 and 7.2 hold. For any  $w \in U$ , we have*

$$\nabla \Phi(w)P_s(w)F^{-1}(w)\nabla f(w) = 0, \tag{82}$$

and  $\text{Range } \nabla \Phi(w) \subset T_{\Phi(w)}\mathcal{R}$ . Especially, if we further assume that  $\max\{\delta_F, \delta\} < \frac{1}{3}\lambda_{H_{F,s}}$ , then for any  $z \in \mathcal{R}$ ,  $\nabla \Phi(z)$  is the oblique projection onto  $T_z\mathcal{R}$  in the direct sum decomposition  $\mathbb{R}^p = T_z\mathcal{R} \oplus \text{Range } P_s(z)$ .

*Proof.* First, note that  $\Phi(w) = \lim_{n \rightarrow \infty} \phi_1^{(n)}(w)$ , where  $\phi_1(w) := \psi_t(w)|_{t=1}$  denotes the time-1 map of the flow. Since  $F$  and  $f$  are smooth,  $\phi_1$  is smooth. Then the smoothness of  $\Phi$  follows immediately from Theorem 5.1 in (Falconer, 1983). For any  $w \in U$ , noting that

$$-\nabla \Phi(w)P_s(w)F^{-1}(w)\nabla f(w) = \frac{d}{dt}\Phi(\psi_t(w))|_{t=0} = \frac{d}{dt}\Phi(w)|_{t=0} = 0, \tag{83}$$

we get (82). Besides,  $\text{Range } \nabla \Phi(w) \subset T_{\Phi(w)}\mathcal{R}$  is due to  $\Phi(w) \in \mathcal{R}$ .

It follows that for any  $z \in \mathcal{R}$  and any  $v \in \mathbb{R}^p$ , we have

$$\begin{aligned}
 0 &= \nabla (\nabla \Phi F_s^\dagger \nabla f)(z)[v] \\
 &= \nabla^2 \Phi(z)[v] \underbrace{F_s^\dagger(z)\nabla f(z)}_{=0} + \nabla \Phi(z)\nabla F_s^\dagger(z)[v]\nabla f(z) + \nabla \Phi(z)F_s^\dagger(z)\nabla^2 f(z)[v] \\
 &= \nabla \Phi(z) (\nabla F_s^\dagger(z)[v]\nabla f(z) + F_s^\dagger(z)\nabla^2 f(z)[v]).
 \end{aligned} \tag{84}$$

Define the linear map  $T_z$  as  $T_z(v) = \nabla F_s^\dagger(z)[v]\nabla f(z) + F_s^\dagger(z)\nabla^2 f(z)v$ . Noting that

$$\begin{aligned}
 \nabla F_s^\dagger(z)[v]\nabla f(z) &= \nabla P_s(z)[v]F^{-1}(z)P_s(z)\nabla f(z) + P_s(z)\nabla F^{-1}(z)[v]P_s(z)\nabla f(z) + P_s(z)F^{-1}(z)\nabla P_s(z)[v]\nabla f(z) \\
 &= P_s(z)F^{-1}(z)\nabla P_s(z)[v]\nabla f(z),
 \end{aligned} \tag{85}$$

the range of  $T_z$  is a subspace of  $\text{Range } P_s(z)$ . By Lemma J.1 and Assumption 7.2, for  $v$  satisfying  $P_s(z)v = v$ ,

$$\|T_z(v)\|_{F(z)^{-1}} \geq \lambda_{H_{F,s}} \|v\|_{F(z)} - \frac{\delta_{F_s}}{G} \|\nabla f(z)\|_{F^{-1}(z)} \|v\|_{F(z)} \geq (\lambda_{H_{F,s}} - \delta_{F_s}) \|v\|_{F(z)}. \quad (86)$$

This implies that  $T_z|_{\text{Range } P_s(z)} : \text{Range } P_s(z) \rightarrow \text{Range } P_s(z)$  is a linear isomorphism. Therefore, by (84), we get that  $\text{Range } P_s(z) \subset \text{Null } \nabla \Phi(z)$ , and  $\dim(\text{Null } \nabla \Phi(z)) \geq \dim(\text{Range } P_s(z))$ .

On the other hand, for any smoothed curve  $\tilde{z}_t$  on  $\mathcal{R}$ ,  $\nabla \Phi(\tilde{z}_t) \dot{\tilde{z}}_t = \frac{d}{dt} \Phi(\tilde{z}_t) = \dot{\tilde{z}}_t$ . Thus  $\nabla \Phi(z)|_{T_z \mathcal{R}} = id$  for any  $z \in \mathcal{R}$ . It yields  $p = \dim(\text{Range } \nabla \Phi(z)) + \dim(\text{Null } \nabla \Phi(z)) \geq \dim(T_z \mathcal{R}) + \dim(\text{Range } P_s(z)) \geq p$ , implying that  $\text{Range } P_s(z) = \text{Null } \nabla \Phi(z)$ . We get the conclusion.  $\square$

By definition,  $f$  exhibits strong convexity along the sharp directions, and consequently inherits certain properties of strongly convex functions. We first present this characteristic (as well as  $L$ -smoothness) in Lemmas J.3 and J.4.

**Lemma J.3.** *Suppose Assumptions 7.1 and 7.2 hold. Denote  $\gamma = \lambda_{H_{F,s}} - \frac{\delta_{F_s}}{2}$ ,  $\ell = L_{H_{F,s}} + \frac{\delta_{F_s}}{2}$ . Then for any  $w \in U$  the following inequality hold*

$$\|P_s(\psi_t(w))F(\psi_t(w))^{-1}\nabla f(\psi_t(w))\|_{F(\psi_t(w))} \leq \exp(-\gamma t) \|P_s(w)F(w)^{-1}\nabla f(w)\|_{F(w)}, \quad (87)$$

and

$$\|P_s(\psi_t(w))F(\psi_t(w))^{-1}\nabla f(\psi_t(w))\|_{F(\psi_t(w))} \geq \exp(-\ell t) \|P_s(w)F(w)^{-1}\nabla f(w)\|_{F(w)}. \quad (88)$$

*Proof.*

$$\begin{aligned} \frac{d}{dt} \|P_s F^{-1} \nabla f\|_F^2 &= 2\partial_t \psi_t(w)^\top \nabla^2 f P_s F^{-1} \nabla f + \nabla f^\top \partial_t (P_s F^{-1} P_s) \nabla f \\ &= -2\nabla f^\top F^{-1} P_s \nabla^2 f P_s F^{-1} \nabla f + \nabla f^\top \nabla (F_s^\dagger) [-F_s^\dagger \nabla f] \nabla f \\ &\stackrel{(78)}{\leq} -2\lambda_{H_{F,s}} \|P_s F^{-1} \nabla f\|_F^2 + \delta_{F_s} \|P_s F^{-1} \nabla f\|_F^2. \end{aligned} \quad (89)$$

Using Gronwall's inequality (Lemma J.16) gives

$$\|P_s(\psi_t(w))F(\psi_t(w))^{-1}\nabla f(\psi_t(w))\|_{F(\psi_t(w))}^2 \leq \exp(-2\gamma t) \|P_s(w)F(w)^{-1}\nabla f(w)\|_{F(w)}^2. \quad (90)$$

On the other hand, we have

$$\begin{aligned} \frac{d}{dt} \|P_s F^{-1} \nabla f\|_F^2 &= -2\nabla f^\top F^{-1} P_s \nabla^2 f P_s F^{-1} \nabla f + \nabla f^\top \nabla (F_s^\dagger) [-F_s^\dagger \nabla f] \nabla f \\ &\stackrel{(78)}{\geq} -2L_{H_{F,s}} \|P_s F^{-1} \nabla f\|_F^2 - \delta_{F_s} \|P_s F^{-1} \nabla f\|_F^2. \end{aligned} \quad (91)$$

Similarly, we get

$$\|P_s(\psi_t(w))F(\psi_t(w))^{-1}\nabla f(\psi_t(w))\|_{F(\psi_t(w))}^2 \geq \exp(-2\ell t) \|P_s(w)F(w)^{-1}\nabla f(w)\|_{F(w)}^2. \quad (92)$$

$\square$

**Lemma J.4.** *Suppose Assumptions 7.1 and 7.2 hold. Then for any  $w \in U$  we have*

$$\frac{\gamma \lambda_{F_s}}{2} \|w - \Phi(w)\|_2^2 \leq f(w) - f(\Phi(w)), \quad (93)$$

and

$$\frac{1}{2\ell} \|P_s(w)F(w)^{-1}\nabla f(w)\|_{F(w)}^2 \leq f(w) - f(\Phi(w)) \leq \frac{1}{2\gamma} \|P_s(w)F(w)^{-1}\nabla f(w)\|_{F(w)}^2. \quad (94)$$

*Proof.* Given  $w$ , define  $a_t = \|P_s(\psi_t(w))F(\psi_t(w))^{-1}\nabla f(\psi_t(w))\|_{F(\psi_t(w))}$ . Then Lemma J.3 implies that for any  $t, s > 0$ ,  $a_{t+s} \leq e^{-\gamma s}a_t$ . Note that  $f(w) - f(\Phi(w)) = \int_0^\infty \nabla f(\psi_t(w))^\top P_s(\psi_t(w))F(\psi_t(w))^{-1}\nabla f(\psi_t(w))dt = \int_0^\infty a_t^2 dt$ ,  $\|w - \Phi(w)\|_2 = \|\int_0^\infty P_s(\psi_t(w))F(\psi_t(w))^{-1}\nabla f(\psi_t(w))dt\|_2 \leq \lambda_{F_s}^{-1/2} \int_0^\infty a_t dt$ . We have

$$\begin{aligned} \lambda_{F_s} \|w - \Phi(w)\|_2^2 &\leq \left(\int_0^\infty a_t dt\right)^2 = \int_0^\infty \int_0^\infty a_s a_t ds dt = 2 \int_0^\infty dt \int_t^\infty a_s a_t ds \\ &\leq 2 \int_0^\infty a_t^2 \left(\int_t^\infty e^{-\gamma(s-t)} ds\right) dt = \frac{2}{\gamma} \int_0^\infty a_t^2 dt. \end{aligned} \quad (95)$$

On the other hand, by Lemma J.3, it holds that

$$\begin{aligned} f(w) - f(\Phi(w)) &= \int_0^\infty \|P_s(\psi_t(w))F(\psi_t(w))^{-1}\nabla f(\psi_t(w))\|_{F(\psi_t(w))}^2 dt \\ &\leq \int_0^\infty \exp(-2\gamma t) \|P_s(w)F(w)^{-1}\nabla f(w)\|_{F(w)}^2 dt \\ &= \frac{1}{2\gamma} \|P_s(w)F(w)^{-1}\nabla f(w)\|_{F(w)}^2, \end{aligned} \quad (96)$$

and

$$\begin{aligned} f(w) - f(\Phi(w)) &= \int_0^\infty \|P_s(\psi_t(w))F(\psi_t(w))^{-1}\nabla f(\psi_t(w))\|_{F(\psi_t(w))}^2 dt \\ &\geq \int_0^\infty \exp(-2\ell t) \|P_s(w)F(w)^{-1}\nabla f(w)\|_{F(w)}^2 dt \\ &= \frac{1}{2\ell} \|P_s(w)F(w)^{-1}\nabla f(w)\|_{F(w)}^2. \end{aligned} \quad (97)$$

□

The following lemma elucidates the property of  $\nabla\Phi$ : it approximates the projection to the flat subspace.

**Lemma J.5.** *Suppose Assumptions 7.1 and 7.2 hold, and*

$$\mu_1 := \lambda_{H_{F,s}} - \frac{3}{2}\delta_{F_s} \geq 0, \quad 2\delta\lambda_{F_s}^{-1} \frac{1}{\gamma} \left(1 + \frac{\delta_{F_s}}{2\mu_1}\right) \leq \frac{1}{2\rho}. \quad (98)$$

Define

$$\epsilon_\Phi = \frac{4\delta\kappa_{F_s}}{\gamma + \mu_1} + \frac{4\kappa_{F_s}^2\delta}{\gamma} \left(1 + \frac{\delta_{F_s}}{2\mu_1}\right) \left(1 + \frac{2\delta}{\gamma + \mu_1}\right) + \frac{2\delta_{F_s}\kappa_{F_s}}{\mu_1} \left(1 + \frac{2\delta}{\gamma + \mu_1}\right). \quad (99)$$

Then for any  $w \in U$  and any vector  $v \in \mathbb{R}^p$ , we have

$$\|P_s(\Phi(w))\nabla\Phi(w)v\|_{F(\Phi(w))} \leq \frac{\epsilon_\Phi}{2} \|v\|_{F(\Phi(w))}, \quad (100)$$

$$\|P_f(\Phi(w))\nabla\Phi(w)v - P_f(w)v\|_{F(\Phi(w))} \leq \frac{\epsilon_\Phi}{2} \|v\|_{F(\Phi(w))}. \quad (101)$$

Thus

$$\|\nabla\Phi(w)v - P_f(w)v\|_{F(\Phi(w))} \leq \epsilon_\Phi \|v\|_{F(\Phi(w))}. \quad (102)$$

*Proof.* Define

$$h_t = P_s(\psi_t(w))\partial_w\psi_t(w)[v], \quad r_t = P_f(\psi_t(w))\partial_w\psi_t(w)[v]. \quad (103)$$

It implies that  $h_t + r_t = \partial_w\psi_t(w)[v]$ ,  $h_0 + r_0 = v$  and  $\lim_{t \rightarrow \infty} h_t + \lim_{t \rightarrow \infty} r_t = \nabla\Phi(w)[v]$ .

We compute the time derivative of  $\|h_t\|_F^2$ :

$$\begin{aligned} \frac{d}{dt} \|h_t\|_{F(\psi_t(w))}^2 &= \frac{d}{dt} (v^\top \partial_w \psi_t(w)^\top F_s(\psi_t(w)) \partial_w \psi_t(w) v) \\ &= \underbrace{v^\top \partial_w \psi_t(w)^\top \nabla F_s(\psi_t(w)) [\partial_t \psi_t(w)] \partial_w \psi_t(w) v}_A + 2 \underbrace{v^\top \partial_w \psi_t(w)^\top F_s(\psi_t(w)) \partial_t \partial_w \psi_t(w) v}_B. \end{aligned} \quad (104)$$

$$\begin{aligned} A &= -v^\top \partial_w \psi_t(w)^\top \nabla F_s(\psi_t(w)) [F_s^\dagger(\psi_t(w)) \nabla f(\psi_t(w))] \partial_w \psi_t(w) v \\ &\stackrel{(79)}{\leq} \delta_{F_s} \|\partial_w \psi_t(w) v\|_{F_s} \|\partial_w \psi_t(w) v\|_F. \end{aligned} \quad (105)$$

$$\begin{aligned} B &= -h_t^\top F_s(\psi_t(w)) \partial_w (F_s^\dagger(\psi_t(w)) \nabla f(\psi_t(w))) v \\ &= -h_t^\top F_s(\psi_t(w)) \partial_w (F_s^\dagger(\psi_t(w))) [v] \nabla f(\psi_t(w)) - h_t^\top \nabla^2 f(\psi_t(w)) h_t \\ &= -h_t^\top F_s \nabla F_s^\dagger [\partial_w \psi_t(w) [v]] \nabla f - h_t^\top P_s \nabla^2 f P_s h_t \\ &\stackrel{(78)}{\leq} \delta_{F_s} \|F_s h_t\|_{F^{-1}} \|\partial_w \psi_t(w) [v]\|_F - \lambda_{H_{F,s}} \|h_t\|_F^2, \end{aligned} \quad (106)$$

Substituting (105) and (106) into (104) yields

$$\begin{aligned} \frac{d}{dt} \|h_t\|_{F(\psi_t(w))}^2 &\leq 3\delta_{F_s} \|h_t\|_{F(\psi_t(w))} \|h_t + r_t\|_{F(\psi_t(w))} - 2\lambda_{H_{F,s}} \|h_t\|_{F(\psi_t(w))}^2 \\ &\leq -2 \underbrace{\left( \lambda_{H_{F,s}} - \frac{3}{2} \delta_{F_s} \right)}_{:=\mu_1} \|h_t\|_{F(\psi_t(w))}^2 + \delta_{F_s} \|h_t\|_{F(\psi_t(w))} \|r_t\|_{F(\psi_t(w))}. \end{aligned} \quad (107)$$

Next we consider the time derivative for  $r_t$ . Directly computing  $\frac{d}{dt} r_t$  gives:

$$\frac{d}{dt} r_t = \underbrace{\nabla P_f(\psi_t(w)) [\partial_t \psi_t(w)] \partial_w \psi_t(w) v}_c + \underbrace{P_f(\psi_t(w)) \partial_t \partial_w \psi_t(w) v}_d. \quad (108)$$

For the term  $c$ :

$$\begin{aligned} \|c\|_{F(\psi_t(w))} &= \|\nabla P_f(\psi_t(w)) [F_s^\dagger(\psi_t(w)) \nabla f(\psi_t(w))] \partial_w \psi_t(w) v\|_{F(\psi_t(w))} \\ &\stackrel{(75)}{\leq} \frac{\delta}{\|F_s^\dagger(\psi_0(w)) \nabla f(\psi_0(w))\|_{F(\psi_0(w))}} \|\partial_w \psi_t(w) v\|_{F(\psi_t(w))} \|F_s^\dagger(\psi_t(w)) \nabla f(\psi_t(w))\|_{F(\psi_t(w))} \\ &\stackrel{(J.3)}{\leq} \delta e^{-\gamma t} \|\partial_w \psi_t(w) v\|_{F(\psi_t(w))}. \end{aligned} \quad (109)$$

where the first inequality also uses  $\nabla P_s + \nabla P_f = \nabla I = 0$ .

Note that for any vector  $p$ ,

$$\begin{aligned} P_f(w) \nabla (F_s^\dagger)(w) [p] &= P_f(w) [\nabla P_s(w) [p] F^{-1} P_s + P_s \nabla (F^{-1})(w) [p] P_s + P_s F^{-1} \nabla P_s [p]] \\ &= P_f(w) \nabla (P_s)(w) [p] F^{-1}(w) P_s(w). \end{aligned} \quad (110)$$

Thus

$$\begin{aligned} \|d\|_{F(\psi_t(w))} &= \|P_f(\psi_t(w)) \partial_w (F_s^\dagger(\psi_t(w)) \nabla f(\psi_t(w))) v\|_{F(\psi_t(w))} \\ &\leq \|P_f(\psi_t(w)) \partial_w (F_s^\dagger(\psi_t(w))) [v] \nabla f(\psi_t(w))\|_{F(\psi_t(w))} \\ &\quad + \|P_f(\psi_t(w)) F_s^\dagger(\psi_t(w)) \nabla^2 f(\psi_t(w)) \partial_w \psi_t(w) v\|_{F(\psi_t(w))} \\ &\stackrel{(110)}{=} \|P_f(\psi_t(w)) \nabla P_s(\psi_t(w)) [\partial_w \psi_t(w) v] F_s^\dagger(\psi_t(w)) \nabla f(\psi_t(w))\|_{F(\psi_t(w))} \\ &\stackrel{(75)}{\leq} \frac{\delta}{\|F_s^\dagger(\psi_0(w)) \nabla f(\psi_0(w))\|_{F(\psi_0(w))}} \|\partial_w \psi_t(w) [v]\|_{F(\psi_t(w))} \|F_s^\dagger(\psi_t(w)) \nabla f(\psi_t(w))\|_{F(\psi_t(w))} \\ &\stackrel{(87)}{\leq} \delta e^{-\gamma t} \|\partial_w \psi_t(w) [v]\|_{F(\psi_t(w))}. \end{aligned} \quad (111)$$

Substituting (109) and (111) into (108) yields

$$\left\| \frac{d}{dt} r_t \right\|_{F(\psi_t(w))} \leq 2\delta e^{-\gamma t} \|h_t + r_t\|_{F(\psi_t(w))}. \quad (112)$$

Now we combine (107) and (112) to get respective bounds. Denote  $M_t = \sup_{0 \leq s \leq t} \|r_s\|_{F(\psi_s(w))}$ . Using Lemma J.14 to (107) gives

$$\|h_t\|_{F(\psi_t(w))} \leq e^{-\mu_1 t} \|h_0\|_{F(\psi_0(w))} + \frac{1}{2} \delta_{F_s} e^{-\mu_1 t} \int_0^t e^{\mu_1 s} \|r_s\|_{F(\psi_s(w))} ds \quad (113)$$

$$\leq e^{-\mu_1 t} \|h_0\|_{F(\psi_0(w))} + \frac{\delta_{F_s}}{2\mu_1} M_t. \quad (114)$$

Thus for any  $t \geq 0$ ,

$$\|r_t - r_0\|_2 \leq \int_0^t \left\| \frac{d}{dr} r_s \right\|_2 ds \leq \lambda_{F_s}^{-1} \int_0^t \left\| \frac{d}{dr} r_s \right\|_{F(\psi_s(w))} ds \quad (115)$$

$$\stackrel{(112)}{\leq} \lambda_{F_s}^{-1} \int_0^t 2\delta e^{-\gamma s} (\|h_s\|_{F(\psi_s(w))} + \|r_s\|_{F(\psi_s(w))}) ds \quad (116)$$

$$\stackrel{(114)}{\leq} 2\delta \lambda_{F_s}^{-1} \int_0^t e^{-\gamma s} \left( e^{-\mu_1 s} \|h_0\|_{F(w)} + \left(1 + \frac{\delta_{F_s}}{2\mu_1}\right) M_t \right) ds \quad (117)$$

$$\leq 2\delta \lambda_{F_s}^{-1} \left( \frac{\|h_0\|_{F(w)}}{\gamma + \mu_1} + \frac{1}{\gamma} \left(1 + \frac{\delta_{F_s}}{2\mu_1}\right) M_t \right). \quad (118)$$

Using  $M_t \leq \rho(\|r_0\|_2 + \sup_{0 \leq s \leq t} \|r_s - r_0\|_2)$  and  $2\delta \lambda_{F_s}^{-1} \frac{1}{\gamma} \left(1 + \frac{\delta_{F_s}}{2\mu_1}\right) \leq \frac{1}{2\rho}$ , we get for any  $t \geq 0$ ,

$$M_t \leq 2\kappa_{F_s} \left( \|r_0\|_{F(w)} + 2\delta \frac{\|h_0\|_{F(w)}}{\gamma + \mu_1} \right). \quad (119)$$

Substituting it into (114) and (118) respectively, we get

$$\begin{aligned} \|h_t\|_{F(\psi_t(w))} &\leq e^{-\mu_1 t} \|h_0\|_{F(\psi_0(w))} + \frac{\delta_{F_s}}{\mu_1} \kappa_{F_s} \left( \|r_0\|_{F(w)} + 2\delta \frac{\|h_0\|_{F(w)}}{\gamma + \mu_1} \right) \\ &\leq e^{-\mu_1 t} \|h_0\|_{F(\psi_0(w))} + \frac{1}{2} \epsilon_\Phi \|v\|_{F(w)}, \end{aligned} \quad (120)$$

and

$$\begin{aligned} \|r_t - r_0\|_2 &\leq 2\delta \lambda_{F_s}^{-1} \frac{\|h_0\|_{F(w)}}{\gamma + \mu_1} + \frac{4\kappa_{F_s}^2 \delta}{\gamma \rho} \left(1 + \frac{\delta_{F_s}}{2\mu_1}\right) \left( \|r_0\|_{F(w)} + 2\delta \frac{\|h_0\|_{F(w)}}{\gamma + \mu_1} \right) \\ &\leq \frac{1}{2} \epsilon_\Phi \frac{\|v\|_{F(w)}}{\rho}. \end{aligned} \quad (121)$$

Noting that  $\lim_{t \rightarrow \infty} h_t = P_s(\Phi(w)) \nabla \Phi(w) v$  and  $\lim_{t \rightarrow \infty} (r_t - r_0) = P_f(\Phi(w)) \nabla \Phi(w) v - P_f(w) v$ , we get the conclusion.  $\square$

## J.2. Dynamics Analysis

**Lemma J.6.** *Suppose Assumptions 7.1 and 7.2 hold, and*

$$\epsilon_\Phi \leq \frac{1}{10} \min\{1, \alpha\beta_1\}, \quad \delta_{F_s} \leq \frac{1}{10} \lambda_{H_{F,s}}, \quad \eta_0 \delta_{F_s} \chi \left( \frac{1}{\alpha \kappa_F^{1/2}} + \beta_2 \right) \leq \frac{1}{5} \alpha. \quad (122)$$

Let  $\iota_t = \min\{\frac{1}{2}\alpha, \lambda_{H_{F,s}}\beta_1\eta_t\}$ . We have

$$\begin{aligned} \|w_t - \Phi(w_t)\|_2^2 + \eta_t \|m_t\|_{F_s^\dagger(w_t)}^2 &\lesssim \exp\left(-\int_0^t \iota_s ds\right) \\ &+ \varepsilon \int_0^t \exp\left(-\int_s^t \iota_\tau d\tau\right) (\|\nabla f(w_s)\|_{F_f^\dagger(w_s)}^2 + \|m_s\|_{F_f^\dagger(w_s)}^2) ds \end{aligned} \quad (123)$$

Especially, taking  $\alpha = 2\eta_0 \lambda_{H_{F,s}}^{\frac{1}{2}}$  and  $\beta_1 = \lambda_{H_{F,s}}^{-\frac{1}{2}}$  gives

$$\begin{aligned} \|w_t - \Phi(w_t)\|_2^2 + \eta_t \|m_t\|_{F_s^\dagger(w_t)}^2 &\lesssim \exp\left(-\lambda_{H_{F,s}}^{\frac{1}{2}} \int_0^t \eta_s ds\right) \\ &+ \varepsilon \int_0^t \exp\left(-\lambda_{H_{F,s}}^{\frac{1}{2}} \int_s^t \eta_\tau d\tau\right) (\|\nabla f(w_s)\|_{F_f^\dagger(w_s)}^2 + \|m_s\|_{F_f^\dagger(w_s)}^2) ds. \end{aligned} \quad (124)$$

*Remark J.7.* Such choices of  $\alpha$  and  $\beta_1$  yield fast convergence in the (strongly convex) sharp directions of the ill-conditioned landscape. The rate  $\exp\left(-\lambda_{H_{F,s}}^{\frac{1}{2}} \int_0^t \eta_s ds\right)$  matches the results in (Attouch et al., 2022).

*Proof.* We first consider general hyper-parameters  $\alpha$ ,  $\beta_1$  and  $\eta_t$ . Recall that  $\dot{w}_t = -\eta_t F_s(w_t)^{-1}(m_t + \beta_1 \nabla f(w_t)) - \eta_t \chi F_f(w_t)^{-1}(m_t + \beta_2 \nabla f(w_t))$ . We begin by bounding  $\|\dot{w}_t\|_{F(w_t)}$ . Using  $\dot{m}_t = -\alpha m_t + \nabla f(w_t)$ , we have  $m_t = e^{-\alpha t} \int_0^t e^{\alpha s} \nabla f(w_s) ds$ . It yields

$$\begin{aligned} \|\dot{w}_t\|_{F(w_t)} &\leq \eta_t (\chi \|m_t\|_{F^{-1}(w_t)} + \beta_2 \|\nabla f(w_t)\|_{F^{-1}(w_t)}) \\ &\leq \eta_t \chi \left( \lambda_F^{-\frac{1}{2}} \int_0^t e^{\alpha-(t-s)} \|\nabla f(w_s)\|_2 ds + \beta_2 \|\nabla f(w_t)\|_{F^{-1}(w_t)} \right) \\ &\leq \eta_t \chi \underbrace{\left( \frac{1}{\alpha \kappa_F^{1/2}} + \beta_2 \right)}_{:=C_w} G. \end{aligned} \quad (125)$$

Now consider the Lyapunov function:

$$V_t = (f(w_t) - f(\Phi(w_t))) + \frac{\eta_t}{2} \|m_t\|_{F_s^\dagger(w_t)}^2. \quad (126)$$

For notational brevity, we define  $\tilde{m}_t = m_t + \beta_1 \nabla f(w_t)$ , and

$$\begin{aligned} \Delta_1 &= \langle \nabla f(w_t), (P_f(w_t) - \nabla \Phi(w_t)) \dot{w}_t \rangle, \quad \Delta_2 = \frac{\dot{\eta}_t}{2} \|m_t\|_{F_s^\dagger(w_t)}^2, \\ \Delta_3 &= m_t^\top \nabla F_s^\dagger(w_t) [\dot{w}_t] m_t. \end{aligned} \quad (127)$$

For  $\Delta_1$  We have

$$\begin{aligned}
 \Delta_1 &= \langle \nabla f(w_t), (P_f(w_t) - \nabla \Phi(w_t))P_f(w_t)\dot{w}_t \rangle + \langle \nabla f(w_t), (P_f(w_t) - \nabla \Phi(w_t))P_s(w_t)\dot{w}_t \rangle \\
 &\stackrel{(102)}{\leq} \epsilon_{\Phi}\eta_t \|\nabla f(w_t)\|_{F^{-1}(w_t)} \left( \|m_t + \beta_1 \nabla f(w_t)\|_{F_s^\dagger(w_t)} + \chi \|m_t + \beta_2 \nabla f(w_t)\|_{F_f^\dagger(w_t)} \right) \\
 &\leq \epsilon_{\Phi}\eta_t (\|\nabla f(w_t)\|_{F_s^\dagger(w_t)} + \|\nabla f(w_t)\|_{F_f^\dagger(w_t)}) \left( \|m_t\|_{F_s^\dagger(w_t)} + \beta_1 \|\nabla f(w_t)\|_{F_s^\dagger(w_t)} \right) \\
 &\quad + \epsilon_{\Phi}\eta_t (\|\nabla f(w_t)\|_{F_s^\dagger(w_t)} + \|\nabla f(w_t)\|_{F_f^\dagger(w_t)}) \left( \chi \|m_t\|_{F_f^\dagger(w_t)} + \chi\beta_2 \|\nabla f(w_t)\|_{F_f^\dagger(w_t)} \right) \\
 &\leq 2\epsilon_{\Phi} \left( \frac{1}{\alpha} + \beta_1 \right) \eta_t \|\nabla f(w_t)\|_{F_s^\dagger(w_t)}^2 + \epsilon_{\Phi} \left( \frac{1}{\alpha} + \frac{\beta_1}{2} + \chi\beta_2 + \frac{\chi^2\beta_2^2\alpha}{2} \right) \eta_t \|\nabla f(w_t)\|_{F_f^\dagger(w_t)}^2 + \frac{\epsilon_{\Phi}\alpha}{2} \eta_t \|m_t\|_{F_s^\dagger(w_t)}^2 \\
 &\quad + \frac{\epsilon_{\Phi}\alpha}{2} \eta_t \chi^2 \|m_t\|_{F_f^\dagger(w_t)}^2.
 \end{aligned} \tag{128}$$

where the last inequality uses AM-GM inequality.

For  $\Delta_2$ ,

$$\begin{aligned}
 |\Delta_3| &\stackrel{(78)}{\leq} \eta_t \delta_{F_s} C_w \|m_t\|_{F_s^\dagger(w_t)} \|m_t\|_{F^{-1}(w_t)} \\
 &\leq \eta_t \delta_{F_s} C_w \|m_t\|_{F_s^\dagger(w_t)}^2 + \eta_t \delta_{F_s} C_w \|m_t\|_{F_s^\dagger(w_t)} \|m_t\|_{F_f^\dagger(w_t)} \\
 &\leq \frac{3}{2} \eta_t \delta_{F_s} C_w \|m_t\|_{F_s^\dagger(w_t)}^2 + \frac{1}{2} \eta_t \delta_{F_s} C_w \|m_t\|_{F_f^\dagger(w_t)}^2,
 \end{aligned} \tag{129}$$

where the second inequality uses  $\|m_t\|_{F^{-1}(w_t)} \leq \|m_t\|_{F_s^\dagger(w_t)} + \|m_t\|_{F_f^\dagger(w_t)}$  and the last inequality uses Cauchy inequality.

Directly computing the time derivative yields

$$\begin{aligned}
 \frac{d}{dt} V_t + \iota_t V_t &= \Delta_1 + \Delta_2 + \frac{\eta_t}{2} \Delta_3 - \alpha \eta_t \|m_t\|_{F_s^\dagger(w_t)}^2 - \beta_1 \eta_t \|\nabla f(w_t)\|_{F_s^\dagger(w_t)}^2 + \iota_t (f(w_t) - f(\Phi(w_t))) + \frac{\eta_t \iota_t}{2} \|m_t\|_{F_s^\dagger(w_t)}^2 \\
 &\leq \left( -\beta_1 \eta_t + \frac{\iota_t}{2\gamma} + 2\epsilon_{\Phi} \left( \frac{1}{\alpha} + \beta_1 \right) \eta_t \right) \|\nabla f(w_t)\|_{F_s^\dagger(w_t)}^2 + \left( -\alpha \eta_t + \frac{\eta_t \iota_t}{2} + \frac{1}{2} \epsilon_{\Phi} \alpha \eta_t + \eta_t^2 \delta_{F_s} C_w \right) \|m_t\|_{F_s^\dagger(w_t)}^2 \\
 &\quad + \epsilon_{\Phi} \left( \frac{1}{\alpha} + \frac{\beta_1}{2} + \chi\beta_2 + \frac{\chi^2\beta_2^2\alpha}{2} \right) \eta_t \|\nabla f(w_t)\|_{F_f^\dagger(w_t)}^2 + \left( \frac{1}{4} \eta_t^2 \delta_{F_s} C_w + \frac{\epsilon_{\Phi}\alpha}{2} \eta_t \chi^2 \right) \|m_t\|_{F_f^\dagger(w_t)}^2,
 \end{aligned} \tag{130}$$

where the inequality uses  $\dot{\eta}_t \leq 0$ , (94), (128) and (129).

Now set  $\epsilon_u = \epsilon_{\Phi} \left( \frac{1}{\alpha} + \frac{\beta_1}{2} + \chi\beta_2 + \frac{\chi^2\beta_2^2\alpha}{2} \right) \eta_t + \left( \frac{1}{4} \eta_t^2 \delta_{F_s} C_w + \frac{\epsilon_{\Phi}\alpha}{2} \eta_t \chi^2 \right)$  and  $U_t = \|\nabla f(w_t)\|_{F_f^\dagger(w_t)}^2 + \|m_t\|_{F_f^\dagger(w_t)}^2$ .

Then by conditions in (122), we have

$$\frac{d}{dt} V_t + \iota_t V_t \leq \epsilon_u U_t. \tag{131}$$

Integrating  $\frac{d}{dt} (e^{\int_0^t \iota_s ds} V_t)$  yields

$$e^{\int_0^t \iota_s ds} V_t \leq V_0 + \epsilon_u \int_0^t e^{\int_0^s \iota_\tau d\tau} U_s ds. \tag{132}$$

By (93) in Lemma J.4, we obtain

$$\begin{aligned}
 \|w_t - \Phi(w_t)\|_2^2 + \eta_t \|m_t\|_{F_s^\dagger(w_t)}^2 &\lesssim \exp \left( - \int_0^t \iota_s ds \right) \\
 &\quad + \varepsilon \int_0^t \exp \left( - \int_s^t \iota_\tau d\tau \right) (\|\nabla f(w_s)\|_{F_f^\dagger(w_s)}^2 + \|m_s\|_{F_f^\dagger(w_s)}^2) ds.
 \end{aligned} \tag{133}$$

If we further take  $\alpha = 2\eta_0 \lambda_{H_{F,s}}^{\frac{1}{2}}$  and  $\beta_1 = \lambda_{H_{F,s}}^{-\frac{1}{2}}$ , then  $\iota_t = \eta_t \lambda_{H_{F,s}}^{\frac{1}{2}}$ , and we finally get

$$\begin{aligned} \|w_t - \Phi(w_t)\|_2^2 + \eta_t \|m_t\|_{F_s^\dagger(w_t)}^2 &\lesssim \exp\left(-\lambda_{H_{F,s}}^{\frac{1}{2}} \int_0^t \eta_s ds\right) \\ &+ \varepsilon \int_0^t \exp\left(-\lambda_{H_{F,s}}^{\frac{1}{2}} \int_s^t \eta_\tau d\tau\right) (\|\nabla f(w_s)\|_{F_f^\dagger(w_s)}^2 + \|m_s\|_{F_f^\dagger(w_s)}^2) ds. \end{aligned} \quad (134)$$

□

**Lemma J.8.** *Suppose Assumptions 7.1 and 7.2 hold. For any  $z \in \mathcal{R}$ , we have*

$$\|P_{\mathcal{R}}(z)v - P_f(z)v\|_{F(z)} \leq \frac{\delta_{F_s}}{\lambda_{H_{F,s}}} \|v\|_{F(z)}. \quad (135)$$

*Proof.* We first compute the closed form of  $P_{\mathcal{R}}$ . Let  $\mathbf{0}^p$  denote the  $p$  dimensional all zero vector. Note that the  $p - k$  dimensional manifold  $\mathcal{R}$  is defined by  $\mathcal{R} = \{w : P_s(w)\nabla f(w) = \mathbf{0}^p\} = \{w : F_s^\dagger(w)\nabla f(w) = \mathbf{0}^p\}$ . Define  $N(w) = F_s^\dagger(w)\nabla f(w)$ . Thus the tangent space is  $T_z\mathcal{R} = \{v : \nabla N(z)v = \mathbf{0}^p\}$ . The projection to  $T_z\mathcal{R}$  is given by

$$P_{\mathcal{R}}(z)v = \operatorname{argmin}_{u \in \mathbb{R}^p} \|v - u\|_{F(z)}^2, \quad \text{s.t. } \nabla N(z)u = \mathbf{0}^p. \quad (136)$$

Directly computing  $\nabla N$  gives  $\nabla N(z)u = \nabla F_s^\dagger(w)[u]\nabla f(w) + F_s^\dagger(w)\nabla f^2(w)u$ .

Noting that  $\|v - u\|_{F(z)}^2 = \|F(z)^{\frac{1}{2}}v - F(z)^{\frac{1}{2}}u\|_2^2$  and  $\nabla N(z)u = \nabla N(z)F(z)^{-\frac{1}{2}}F(z)^{\frac{1}{2}}u$ , We have

$$F(z)^{\frac{1}{2}}P_{\mathcal{R}}(z)v = \underbrace{(I - F(z)^{-\frac{1}{2}}\nabla N(z)^\top(\nabla N(z)F(z)^{-1}\nabla N(z)^\top)^\dagger\nabla N(z)F(z)^{-\frac{1}{2}})}_{K(z)} F(z)^{\frac{1}{2}}v. \quad (137)$$

For notational brevity, we define  $J = F(z)^{-\frac{1}{2}}P_s(z)\nabla^2 f(z)P_s(z)F(z)^{-\frac{1}{2}}$ , and  $\Delta J \in \mathbb{R}^{k \times p}$  satisfying  $\Delta Jq = F(z)^{\frac{1}{2}}\nabla F_s^\dagger(w)[F(z)^{-\frac{1}{2}}q]^\top \nabla f(z)$  for any  $q \in \mathbb{R}^p$ .

Note that  $K(z)$  is the Euclidean projection to the kernel subspace:

$$\ker\left(\nabla N(z)F(z)^{-\frac{1}{2}}\right) = \ker\left(F(z)^{\frac{1}{2}}\nabla N(z)F(z)^{-\frac{1}{2}}\right) = \ker(J + \Delta J), \quad (138)$$

and  $P_f(z)$  is the Euclidean projection to  $\ker J$ . Using Wedin  $\sin(\Theta)$  Theorem (Lemma J.17) to  $J$  and  $J + \Delta J$ , we get

$$\|K(z) - P_f(z)\|_2 \leq \frac{\|\Delta J\|_2}{\lambda_{H_{F,s}}}. \quad (139)$$

It follows that

$$\begin{aligned} \|F(z)^{\frac{1}{2}}P_{\mathcal{R}}(z)v - F(z)^{\frac{1}{2}}P_f(z)v\|_2 &= \|K(z)F(z)^{\frac{1}{2}}v - P_f(z)F(z)^{\frac{1}{2}}v\|_2 \\ &\leq \frac{\|\Delta J\|_2}{\lambda_{H_{F,s}}} \|F(z)^{\frac{1}{2}}v\|_2. \end{aligned} \quad (140)$$

Note that

$$\|\Delta Jq\|_2 = \|\nabla F_s^\dagger(w)[F(z)^{-\frac{1}{2}}q]^\top \nabla f(z)\|_{F(z)} \stackrel{(78)}{\leq} \delta_{F_s} \|q\|_2. \quad (141)$$

Substituting it into (140) yields

$$\|P_{\mathcal{R}}(z)v - P_f(z)v\|_{F(z)} = \|F(z)^{\frac{1}{2}}P_{\mathcal{R}}(z)v - F(z)^{\frac{1}{2}}P_f(z)v\|_2 \leq \frac{\delta_{F_s}}{\lambda_{H_{F,s}}} \|v\|_{F(z)}. \quad (142)$$

□

**Lemma J.9.** Suppose Assumptions 7.1 and 7.2 hold. For any  $x, y \in U$  and  $v \in \mathbb{R}^p$ , we have

$$\|F_s^\dagger(x)v - F_s^\dagger(y)v\|_2 \leq \frac{\delta_{F_s}}{G} \kappa_F^{\frac{1}{2}} \lambda_F^{-\frac{1}{2}} \|x - y\|_2 \|v\|_2, \quad (143)$$

$$\|F_f^\dagger(x)v - F_f^\dagger(y)v\|_2 \leq \frac{\delta_{F_s}}{G} \kappa_F^{\frac{1}{2}} \lambda_F^{-\frac{1}{2}} \|x - y\|_2 \|v\|_2, \quad (144)$$

$$\|P_f(x)v - P_f(y)v\|_2 \leq \frac{\delta}{G} \kappa_F^{\frac{1}{2}} \lambda_F^{-\frac{1}{2}} \|x - y\|_2 \|v\|_2. \quad (145)$$

*Proof.* By Assumption 7.2,

$$\|F_s^\dagger(x)v - F_s^\dagger(y)v\|_2 = \left\| \int_0^1 \nabla F_s^\dagger(x + (y-x)t)[x-y]v dt \right\|_2 \stackrel{(78)}{\leq} \frac{\delta_{F_s}}{G} \kappa_F^{\frac{1}{2}} \lambda_F^{-\frac{1}{2}} \|x - y\|_2 \|v\|_2 \quad (146)$$

We can similarly prove (144) by (81). On the other hand, using  $\nabla P_f + \nabla P_s = 0$ , we get

$$\|P_f(x)v - P_f(y)v\|_2 = \left\| \int_0^1 \nabla P_s(x + (y-x)t)[x-y]v dt \right\|_2 \leq \frac{\delta}{G} \kappa_F^{\frac{1}{2}} \lambda_F^{-\frac{1}{2}} \|x - y\|_2 \|v\|_2. \quad (147)$$

□

**Lemma J.10.** Suppose Assumptions 7.1 and 7.2 hold. The dynamics of  $z_t = \Phi(w_t)$  satisfies

$$\begin{cases} \dot{z}_t = -\eta_t \chi P_{\mathcal{R}}(z_t) F(z_t)^{-1} (s_t + \beta_2 \nabla f(z_t)) + \eta_t \epsilon_{z,t}, \\ \dot{s}_t = -\alpha s_t + \nabla f(z_t), \end{cases} \quad (148)$$

where  $s_0 = 0$  and

$$\|\epsilon_{z,t}\|_2 \lesssim \int_0^t e^{-\alpha(t-s)} \|w_s - \Phi(w_s)\|_2 ds + \|w_t - \Phi(w_t)\|_2 + \varepsilon \|m_t\|_{F_s^\dagger(w_t)} + \varepsilon \|F_f^\dagger(z_t)(s_t + \beta_2 \nabla f(z_t))\|_2 \quad (149)$$

*Proof.* By (82), the dynamics of  $z_t = \Phi(w_t)$  satisfies

$$\dot{z}_t = -\eta_t \nabla \Phi(w_t) \left( F_s^\dagger(w_t) m_t + \chi F_f^\dagger(w_t) (m_t + \beta_2 \nabla f(w_t)) \right). \quad (150)$$

Define  $s_t$  satisfying  $\dot{s}_t = -\alpha s_t + \nabla f(z_t)$  and  $s_0 = 0$ . Then

$$\|s_t - m_t\|_2 = \left\| \int_0^t e^{-\alpha(t-s)} (\nabla f(z_s) - \nabla f(w_s)) ds \right\|_2 \leq L \int_0^t e^{-\alpha(t-s)} \|w_s - \Phi(w_s)\|_2 ds \quad (151)$$

and

$$\max\{\|s_t\|_2, \|m_t\|_2\} \leq \int_0^t e^{-\alpha(t-s)} \max\{\|\nabla f(w_s)\|_2, \|\nabla f(z_s)\|_2\} ds \leq \int_0^t e^{-\alpha(t-s)} \lambda_F^{-\frac{1}{2}} G ds \leq \frac{\lambda_F^{-\frac{1}{2}}}{\alpha} G. \quad (152)$$

On the other hand,

$$\begin{aligned} \|F_s^\dagger(w_t)m_t - F_s^\dagger(z_t)s_t\|_2 &\leq \|F_s^\dagger(w_t)(m_t - s_t)\|_2 + \|F_s^\dagger(w_t)s_t - F_s^\dagger(z_t)s_t\|_2 \\ &\stackrel{(143)}{\leq} \lambda_{F_s}^{-1} \|m_t - s_t\|_2 + \frac{\delta_{F_s}}{G} \kappa_F^{\frac{1}{2}} \lambda_F^{-\frac{1}{2}} \|s_t\|_2 \|w_t - \Phi(w_t)\|_2 \\ &\stackrel{(152)}{\leq} \lambda_{F_s}^{-1} \|m_t - s_t\|_2 + \frac{\delta_{F_s}}{\alpha} \kappa_F^{\frac{1}{2}} \lambda_F^{-1} \|w_t - \Phi(w_t)\|_2 \end{aligned} \quad (153)$$

Similarly

$$\begin{aligned}
 \|F_f^\dagger(w_t)m_t - F_f^\dagger(z_t)s_t\|_2 &\leq \|F_f^\dagger(w_t)(m_t - s_t)\|_2 + \|F_f^\dagger(w_t)s_t - F_f^\dagger(z_t)s_t\|_2 \\
 &\stackrel{(144)}{\leq} \lambda_F^{-1} \|m_t - s_t\|_2 + \frac{\delta_{F_s}}{G} \kappa_F^{\frac{1}{2}} \lambda_F^{-\frac{1}{2}} \|s_t\|_2 \|w_t - \Phi(w_t)\|_2 \\
 &\stackrel{(152)}{\leq} \lambda_{F_s}^{-1} \|m_t - s_t\|_2 + \frac{\delta_{F_s}}{\alpha} \kappa_F^{\frac{1}{2}} \lambda_F^{-1} \|w_t - \Phi(w_t)\|_2,
 \end{aligned} \tag{154}$$

and

$$\begin{aligned}
 \|F_f^\dagger(w_t)\nabla f(w_t) - F_f^\dagger(z_t)\nabla f(z_t)\|_2 &\leq \|F_f^\dagger(w_t)(\nabla f(w_t) - \nabla f(z_t))\|_2 + \|F_f^\dagger(w_t)\nabla f(z_t) - F_f^\dagger(z_t)\nabla f(z_t)\|_2 \\
 &\stackrel{(144)}{\leq} \lambda_F^{-1} L \|w_t - \Phi(w_t)\|_2 + \delta_{F_s} \kappa_F^{\frac{1}{2}} \lambda_F^{-1} \|w_t - \Phi(w_t)\|_2.
 \end{aligned} \tag{155}$$

Now we rewrite (150) as

$$\dot{z}_t = -\eta_t P_{\mathcal{R}}(z_t) \left( F_s^\dagger(z_t)s_t + \chi F_f^\dagger(z_t)(s_t + \beta_2 \nabla f(z_t)) \right) + \eta_t \epsilon_{z,t}, \tag{156}$$

where

$$\begin{aligned}
 \epsilon_{z,t} &= - \underbrace{P_{\mathcal{R}}(z_t) \left( F_s^\dagger(w_t)m_t - F_s^\dagger(z_t)s_t \right)}_a \\
 &\quad - \underbrace{(\nabla \Phi(w_t) - P_{\mathcal{R}}(z_t)) \left( F_s^\dagger(w_t)m_t + \chi F_f^\dagger(z_t)(s_t + \beta_2 \nabla f(z_t)) \right)}_b \\
 &\quad - \underbrace{\chi \nabla \Phi(w_t) \left( F_f^\dagger(w_t)(m_t + \beta_2 \nabla f(w_t)) - F_f^\dagger(z_t)(s_t + \beta_2 \nabla f(z_t)) \right)}_c.
 \end{aligned} \tag{157}$$

By (137), we have

$$\begin{aligned}
 \|a\|_2 &\leq \lambda_F^{-\frac{1}{2}} \|a\|_{F(z_t)} \leq \lambda_F^{-\frac{1}{2}} \|F_s^\dagger(w_t)m_t - F_s^\dagger(z_t)s_t\|_{F(z_t)} \leq \kappa_F^{\frac{1}{2}} \|F_s^\dagger(w_t)m_t - F_s^\dagger(z_t)s_t\|_2 \\
 &\stackrel{(153)}{\leq} \kappa_F^{\frac{1}{2}} \lambda_{F_s}^{-1} \|m_t - s_t\|_2 + \kappa_F^{\frac{1}{2}} \frac{\delta_{F_s}}{\alpha} \kappa_F^{\frac{1}{2}} \lambda_F^{-1} \|w_t - \Phi(w_t)\|_2.
 \end{aligned} \tag{158}$$

For any  $v$ ,

$$\begin{aligned}
 &\|\nabla \Phi(w_t)v - P_{\mathcal{R}}(z_t)v\|_2 \\
 &\leq \|\nabla \Phi(w_t)v - P_f(w_t)v\|_2 + \|P_f(w_t)v - P_f(z_t)v\|_2 + \|P_f(z_t)v - P_{\mathcal{R}}(z_t)v\|_2 \\
 &\leq \lambda_F^{-\frac{1}{2}} \|\nabla \Phi(w_t)v - P_f(w_t)v\|_{F(w_t)} + \|P_f(w_t)v - P_f(z_t)v\|_2 + \lambda_F^{-\frac{1}{2}} \|P_f(z_t)v - P_{\mathcal{R}}(z_t)v\|_{F(w_t)} \\
 &\leq \rho^{\frac{1}{2}} \lambda_F^{-\frac{1}{2}} (\epsilon_\Phi + \frac{\delta_{F_s}}{\lambda_{H_{F,s}}}) \|v\|_2 + \frac{\delta}{G} \kappa_F^{\frac{1}{2}} \lambda_F^{-\frac{1}{2}} \|w_t - \Phi(w_t)\|_2 \|v\|_2,
 \end{aligned} \tag{159}$$

where the last inequality uses (145), Lemma (J.8) and (102). It follows that

$$\begin{aligned}
 \|b\|_2 &\leq \kappa_F^{\frac{1}{2}} (\epsilon_\Phi + \frac{\delta_{F_s}}{\lambda_{H_{F,s}}}) \|F_s^\dagger(w_t)m_t + \chi F_f^\dagger(z_t)(s_t + \beta_2 \nabla f(z_t))\|_2 \\
 &\quad + \frac{\delta}{G} \kappa_F^{\frac{1}{2}} \lambda_F^{-\frac{1}{2}} \|w_t - \Phi(w_t)\|_2 \|F_s^\dagger(w_t)m_t + \chi F_f^\dagger(z_t)(s_t + \beta_2 \nabla f(z_t))\|_2 \\
 &\stackrel{(152)}{\leq} \kappa_F^{\frac{1}{2}} (\epsilon_\Phi + \frac{\delta_{F_s}}{\lambda_{H_{F,s}}}) \|F_s^\dagger(w_t)m_t\|_2 + \chi \kappa_F^{\frac{1}{2}} (\epsilon_\Phi + \frac{\delta_{F_s}}{\lambda_{H_{F,s}}}) \|F_f^\dagger(z_t)(s_t + \beta_2 \nabla f(z_t))\|_2 \\
 &\quad + 2\chi \delta \kappa_F^{\frac{1}{2}} \lambda_F^{-1} (\frac{1}{\alpha} + \beta_2) \|w_t - \Phi(w_t)\|_2.
 \end{aligned} \tag{160}$$

By (102) we have  $\|\nabla \Phi(w_t)\|_2 \leq \|\nabla \Phi(w_t) - P_f(w_t)\|_2 + \|P_f(w_t)\|_2 \leq 1 + \epsilon_\Phi \kappa_F$ . Thus

$$\begin{aligned}
 \|c\|_2 &\leq \chi(1 + \epsilon_{\Phi} \kappa_F) \|F_f^\dagger(w_t)(m_t + \beta_2 \nabla f(w_t)) - F_f^\dagger(z_t)(s_t + \beta_2 \nabla f(z_t))\|_2 \\
 &\stackrel{(154),(155)}{\leq} \chi(1 + \epsilon_{\Phi} \kappa_F) \lambda_{F_s}^{-1} \|m_t - s_t\|_2 + \chi(1 + \epsilon_{\Phi} \kappa_F) \left( \frac{\delta_{F_s}}{\alpha} \kappa_{\frac{1}{2}} \lambda_F^{-1} + \beta_2 \lambda_F^{-1} L + \beta_2 \delta_{F_s} \kappa_{\frac{1}{2}} \lambda_F^{-1} \right) \|w_t - \Phi(w_t)\|_2.
 \end{aligned} \tag{161}$$

Combining (158), (160) and (161), we get

$$\|a + b + c\|_2 = \mathcal{O}(\|m_t - s_t\|_2 + \|w_t - \Phi(w_t)\|_2 + \varepsilon \|m_t\|_{F_s^\dagger(w_t)} + \varepsilon \|F_f^\dagger(z_t)(s_t + \beta_2 \nabla f(z_t))\|_2) \tag{162}$$

Then using (151) gives the conclusion.  $\square$

**Lemma J.11.** *Suppose Assumptions 7.1 and 7.2 hold. Then there exist a constant  $\varepsilon_0 > 0$  depending on  $f$  and  $\alpha, \beta, \{\eta_t\}_t, \chi, \beta_2$  such that for any  $\varepsilon < \varepsilon_0$ , we have*

$$\|\epsilon_{z,t}\|_2^2 \lesssim e^{-\Pi_t} + \varepsilon \int_0^t \exp(\Pi_\tau - \Pi_t) \left( \|\nabla f(z_\tau)\|_{F_f^\dagger(z_t)}^2 + \|s_\tau\|_{F_f^\dagger(z_t)}^2 \right) d\tau + \varepsilon^2 \|s_t + \beta_2 \nabla f(z_t)\|_{F_f^\dagger(z_t)}^2. \tag{163}$$

*Proof.* Define  $\Pi_s = \int_0^s \iota_\tau d\tau$ ,  $D_t = \|w_t - \Phi(w_t)\|_2 + \eta_t^{1/2} \|m_t\|_{F_s^\dagger(w_t)}$  and  $E_t = \|\nabla f(z_t)\|_{F_f^\dagger(z_t)}^2 + \|s_t\|_{F_f^\dagger(z_t)}^2$  for notational brevity. By (123) we have

$$\begin{aligned}
 D_t^2 &\lesssim \exp(-\Pi_t) + \varepsilon \int_0^t \exp(\Pi_s - \Pi_t) (\|\nabla f(w_s) - \nabla f(z_s)\|_{F_f^\dagger(z_t)}^2 + \|m_s - z_s\|_{F_f^\dagger(z_t)}^2 + E_s) ds \\
 &\stackrel{(151)}{\lesssim} \exp(-\Pi_t) + \varepsilon \int_0^t \exp(\Pi_s - \Pi_t) (D_s^2 + \int_0^s e^{-\alpha(s-\tau)} D_\tau^2 d\tau + E_s) ds \\
 &\leq \exp(-\Pi_t) + \varepsilon \int_0^t \exp(\Pi_s - \Pi_t) (D_s^2 + E_s) ds,
 \end{aligned} \tag{164}$$

where we also use  $(\int_0^s e^{-\alpha(s-\tau)} D_\tau d\tau)^2 \leq \int_0^s e^{-\alpha(s-\tau)} D_\tau^2 d\tau \int_0^s e^{-\alpha(s-\tau)} d\tau \lesssim \int_0^s e^{-\alpha(s-\tau)} D_\tau^2 d\tau$  in the second inequality, and

$$\begin{aligned}
 \int_0^t \exp(\Pi_s - \Pi_t) \int_0^s e^{-\alpha(s-\tau)} D_\tau^2 d\tau ds &= \int_0^t \exp(\Pi_\tau - \Pi_t) D_\tau^2 d\tau \int_\tau^t e^{\alpha\tau - \alpha s} \underbrace{\exp(\Pi_s - \Pi_\tau)}_{\leq (s-\tau)\iota_\tau} ds \\
 &\leq \frac{1}{\alpha - \eta_t} \int_0^t \exp(\Pi_\tau - \Pi_t) D_\tau^2 d\tau.
 \end{aligned} \tag{165}$$

in the third inequality. Then by using Gronwall's inequality in Lemma J.16 to  $e^{\Pi_t} D_t^2$ , we get

$$\exp(\Pi_t) D_t^2 \lesssim \exp(\mathcal{O}(\varepsilon t)) \left( 1 + \varepsilon \int_0^t \exp(\Pi_s) E_s ds \right). \tag{166}$$

Substituting it into (151) yields

$$\begin{aligned}
 &\left( \int_0^t e^{-\alpha(t-s)} \|w_s - \Phi(w_s)\|_2 ds \right)^2 \\
 &\leq \int_0^t e^{-\alpha(t-s)} ds \int_0^t e^{-\alpha(t-s)} \|w_s - \Phi(w_s)\|_2^2 ds \\
 &\lesssim \int_0^t e^{-\alpha(t-s)} \exp(-\Pi_s) ds + \varepsilon \int_0^t e^{-\alpha(t-s)} ds \int_0^s \exp(\Pi_\tau - \Pi_s) E_\tau d\tau.
 \end{aligned} \tag{167}$$

To bound the right hand side, we first note that for any fixed  $0 \leq \tau < t$ ,  $\frac{\alpha}{2} \geq \frac{\Pi_s - \Pi_\tau}{s - \tau} \geq \frac{\Pi_t - \Pi_\tau}{t - \tau} := \bar{l}$  since  $\iota_t$  is non-decreasing. This gives

$$\int_\tau^t e^{-\alpha(t-s)} \exp(\Pi_\tau - \Pi_s) ds \leq \int_\tau^t e^{-\alpha(t-s)} e^{-\bar{l}(s-\tau)} ds \leq \frac{1}{\alpha - \bar{l}} e^{-\bar{l}(t-\tau)} \leq \frac{2}{\alpha} e^{\Pi_\tau - \Pi_t}. \quad (168)$$

Thus for the first term in (167), we have

$$\int_0^t e^{-\alpha(t-s)} \exp(-\Pi_s) ds \leq \frac{2}{\alpha} e^{-\Pi_t}. \quad (169)$$

For the second term in (167),

$$\begin{aligned} \int_0^t e^{-\alpha(t-s)} ds \int_0^s \exp(\Pi_\tau - \Pi_s) E_\tau d\tau &= \int_0^t E_\tau d\tau \int_\tau^t e^{-\alpha(t-s)} \exp(\Pi_\tau - \Pi_s) ds \\ &\stackrel{(168)}{\leq} \frac{2}{\alpha} \int_0^t \exp(\Pi_\tau - \Pi_t) E_\tau d\tau. \end{aligned} \quad (170)$$

Substituting (169) and (170) into (167), we get

$$\left( \int_0^t e^{-\alpha(t-s)} \|w_s - \Phi(w_s)\|_2 ds \right)^2 \lesssim e^{-\Pi_t} + \varepsilon \int_0^t \exp(\Pi_\tau - \Pi_t) E_\tau d\tau. \quad (171)$$

Substituting it and (166) into (149) gives

$$\|\epsilon_{z,t}\|_2^2 \lesssim e^{-\Pi_t} + \varepsilon \int_0^t \exp(\Pi_\tau - \Pi_t) \left( \|\nabla f(z_\tau)\|_{F_f^\dagger(z_\tau)}^2 + \|s_\tau\|_{F_f^\dagger(z_\tau)}^2 \right) d\tau + \varepsilon^2 \|s_t + \beta_2 \nabla f(z_t)\|_{F_f^\dagger(z_t)}^2. \quad (172)$$

Note that a sufficiently small  $\varepsilon$  can satisfy the constraints on  $\delta, \delta_F$  in all preceding lemmas. Then, by applying Lemma J.8, we get the conclusion.  $\square$

**Lemma J.12.** *Suppose Assumptions 7.1 and 7.2 hold, and*

$$\delta_{F_s} \leq \min \left\{ \frac{\alpha\beta_2\lambda_{H_{F,s}}}{2}, \frac{\lambda_{H_{F,s}}}{4}, \frac{\alpha}{2\chi\eta_{\min}} \left( \frac{1}{\alpha\kappa_F^{1/2}} + \beta_2 \right)^{-1} \right\}. \quad (173)$$

Then the trajectory  $z_t$  in

$$\begin{cases} \dot{z}_t = -\eta_t \chi P_{\mathcal{R}}(z_t) F(z_t)^{-1} (s_t + \beta_2 \nabla f(z_t)), \\ \dot{s}_t = -\alpha s_t + \nabla f(z_t), \end{cases} \quad (174)$$

starting from  $z_t|_{t=0} = z_0$  and  $s_0 = 0$  satisfies

$$\int_0^t \eta_t \|P_{\mathcal{R}}(z_t) F(z_t)^{-1} \nabla f(z_t)\|_{F(z_t)}^2 \leq \frac{2(f(z_0) - \inf f)}{\chi\beta_2}, \quad \int_0^t \eta_t \|s_t\|_{F(z_t)}^2 \leq \frac{2(f(z_0) - \inf f)}{\chi\alpha}. \quad (175)$$

*Proof.* Consider the Lyapunov function  $W_t = f(z_t) - \inf f + \frac{1}{2}\eta_t\chi\|s_t\|_{F^{-1}(z_t)}^2$ . Then taking the time derivative gives

$$\begin{aligned} \frac{d}{dt} W_t &= \underbrace{-\eta_t \chi \langle (P_{\mathcal{R}}(z_t) - I) F(z_t)^{-1} \nabla f(z_t), s_t \rangle}_{A} - \eta_t \chi \beta_2 \|P_{\mathcal{R}}(z_t) F(z_t)^{-1} \nabla f(z_t)\|_{F(z_t)}^2 \\ &\quad - \eta_t \chi \alpha \|s_t\|_{F^{-1}(z_t)}^2 + \frac{1}{2} \eta_t \chi s_t^\top \nabla F^{-1}(z_t) [\dot{z}_t] s_t + \frac{1}{2} \dot{\eta}_t \chi \|s_t\|_{F^{-1}(z_t)}^2. \end{aligned} \quad (176)$$

By using  $F(z_t)^{-1}\nabla f(z_t) = P_f(z_t)F(z_t)^{-1}\nabla f(z_t)$  and Lemma J.8, we have

$$\|(P_{\mathcal{R}}(z_t) - I)F(z_t)^{-1}\nabla f(z_t)\|_{F(z_t)}^2 = \|(P_{\mathcal{R}}(z_t) - P_f(z_t))F(z_t)^{-1}\nabla f(z_t)\|_{F(z_t)}^2 \leq \frac{\delta_{F_s}^2}{\lambda_{H_{F,s}}^2} \|F(z_t)^{-1}\nabla f(z_t)\|_{F(z_t)}^2. \quad (177)$$

Since  $\|(P_{\mathcal{R}}(z_t) - I)F(z_t)^{-1}\nabla f(z_t)\|_{F(z_t)}^2 + \|P_{\mathcal{R}}F(z_t)^{-1}\nabla f(z_t)\|_{F(z_t)}^2 = \|F(z_t)^{-1}\nabla f(z_t)\|_{F(z_t)}^2$ , we have

$$\|(P_{\mathcal{R}}(z_t) - I)F(z_t)^{-1}\nabla f(z_t)\|_{F(z_t)}^2 \leq \frac{\frac{\delta_{F_s}^2}{\lambda_{H_{F,s}}^2}}{1 - \frac{\delta_{F_s}^2}{\lambda_{H_{F,s}}^2}} \|P_{\mathcal{R}}F(z_t)^{-1}\nabla f(z_t)\|_{F(z_t)}^2. \quad (178)$$

Thus

$$\begin{aligned} A &\stackrel{(173)}{\leq} 2 \frac{\delta_{F_s}}{\lambda_{H_{F,s}}} \eta_t \chi \|P_{\mathcal{R}}(z_t)F(z_t)^{-1}\nabla f(z_t)\|_{F(z_t)} \|s_t\|_{F^{-1}(z_t)} \\ &\leq \frac{\delta_{F_s}}{\alpha \lambda_{H_{F,s}}} \eta_t \chi \|P_{\mathcal{R}}(z_t)F(z_t)^{-1}\nabla f(z_t)\|_{F(z_t)}^2 + \frac{\delta_{F_s} \alpha}{\lambda_{H_{F,s}}} \eta_t \chi \|s_t\|_{F^{-1}(z_t)}^2. \end{aligned} \quad (179)$$

On the other hand, similar to (125), we have

$$\begin{aligned} \|\dot{z}_t\|_{F(z_t)} &\leq \eta_t \chi (\|s_t\|_{F^{-1}(z_t)} + \beta_2 \|\nabla f(z_t)\|_{F^{-1}(z_t)}) \\ &\leq \eta_t \chi \left( \lambda_F^{-\frac{1}{2}} \int_0^t e^{\alpha-(t-s)} \|\nabla f(z_s)\|_2 ds + \beta_2 \|\nabla f(z_t)\|_{F^{-1}(z_t)} \right) \\ &\leq \eta_t \chi \underbrace{\left( \frac{1}{\alpha \kappa_F^{1/2}} + \beta_2 \right)}_{:=C_w} G. \end{aligned} \quad (180)$$

This gives

$$\eta_t \chi s_t^\top \nabla F^{-1}(z_t) [\dot{z}_t] s_t \leq \eta_t^2 \chi \delta_{F_s} C_w \|s_t\|_{F^{-1}(z_t)}^2 \stackrel{(173)}{\leq} \frac{1}{2} \eta_t \chi \alpha \|s_t\|_{F^{-1}(z_t)}^2. \quad (181)$$

Substituting (179) and (181) into (176) yields

$$\frac{d}{dt} W_t = -\frac{1}{2} \eta_t \chi \beta_2 \|P_{\mathcal{R}}(z_t)F(z_t)^{-1}\nabla f(z_t)\|_{F(z_t)}^2 - \frac{1}{2} \eta_t \chi \alpha \|s_t\|_{F^{-1}(z_t)}^2. \quad (182)$$

where we also uses  $\dot{\eta}_t \leq 0$ . Finally, integrating both sides of (182) from 0 to  $t$  yields the conclusion.  $\square$

### J.3. Useful Lemmas

**Lemma J.13 (Cauchy's Inequality).** For any vector  $u, v$  and positive semi-definite matrices  $A$  and  $F$ , by using  $u^\top A v \leq \|A^{\frac{1}{2}} u\|_2 \|A^{\frac{1}{2}} v\|_2 \leq \|A\|_2 \|u\|_2 \|v\|_2$ , we have

$$u^\top A v = u^\top F^{\frac{1}{2}} F^{-\frac{1}{2}} A F^{-\frac{1}{2}} F^{\frac{1}{2}} v \leq \|F^{-\frac{1}{2}} A F^{-\frac{1}{2}}\|_2 \|u\|_2 \|v\|_2. \quad (183)$$

**Lemma J.14.** Let  $a_t, b_t \geq 0$  be real-valued functions defined for  $t \geq 0$ . Suppose  $a_t$  is continuously differentiable and  $b_t$  is continuous with respect to  $t$ . If there exists a constant  $\lambda > 0$  such that

$$\frac{d}{dt} a_t \leq -\lambda a_t + \sqrt{a_t} \sqrt{b_t}, \quad (184)$$

then for all  $t \geq 0$ ,

$$\sqrt{a_t} \leq e^{-\frac{\lambda}{2}t} \sqrt{a_0} + \frac{1}{2} \int_0^t e^{-\frac{\lambda}{2}(t-s)} \sqrt{b_s} ds. \quad (185)$$

*Proof.* Let  $\delta > 0$  be an arbitrary small constant. Define a perturbed variable  $y_t$  as  $y_t = \sqrt{a_t + \delta}$ . Since  $a_t \geq 0$ , we have  $y_t \geq \sqrt{\delta} > 0$  for all  $t$ . Thus,  $y_t$  is continuously differentiable. Substituting  $\frac{d}{dt}y_t$  into (184) gives

$$\frac{d}{dt}y_t \leq -\frac{\lambda}{2}y_t + \frac{\lambda\delta}{2y_t} + \frac{\sqrt{b_t}\sqrt{y_t^2 - \delta}}{2y_t} \leq -\frac{\lambda}{2}y_t + \frac{\sqrt{b_t}}{2} + \frac{\lambda\sqrt{\delta}}{2}. \quad (186)$$

It follows that

$$\frac{d}{dt}\left(e^{\frac{\lambda}{2}t}y_t\right) \leq e^{\frac{\lambda}{2}t}\left(\frac{\sqrt{b_t}}{2} + \frac{\lambda\sqrt{\delta}}{2}\right). \quad (187)$$

Integrating from 0 to  $t$  yields:

$$y_t \leq e^{-\frac{\lambda}{2}t}y_0 + \frac{1}{2}\int_0^t e^{-\frac{\lambda}{2}(t-s)}\sqrt{b_s}ds + \frac{\lambda\sqrt{\delta}}{2}\int_0^t e^{-\frac{\lambda}{2}(t-s)}ds. \quad (188)$$

Take the limit as  $\delta \rightarrow 0$ , we get the conclusion. □

*Remark J.15.* It seems natural to divide the inequality (184) by  $\sqrt{a_t}$  and consider  $\frac{d}{dt}\sqrt{a_t}$ . However, direct differentiation of  $\sqrt{a_t}$  is not well-defined when  $a_t = 0$ . To handle this singularity strictly, we introduce a regularization term  $\delta$ .

**Lemma J.16** (Gronwall's Inequality). *Let  $u_t, \alpha_t$  and  $\beta_t \geq 0$  be continuous functions for  $t \geq 0$ . If*

$$u_t \leq \alpha_t + \int_0^t \beta_s u_s ds, \quad (189)$$

then

$$u_t \leq \alpha_t + \int_0^t \alpha_s \beta_s \exp\left(\int_s^t \beta_\tau d\tau\right) ds. \quad (190)$$

Additionally, of  $\alpha_t$  is non-decreasing, then

$$u_t \leq \alpha_t \exp\left(\int_0^t \beta_\tau d\tau\right). \quad (191)$$

**Lemma J.17** (Wedin  $\sin(\Theta)$  Theorem). *Let  $M$  and  $N$  be two matrices with singular values  $\sigma_1, \dots, \sigma_n$  and  $\tilde{\sigma}_1, \dots, \tilde{\sigma}_n$ , respectively. Denote by  $U_M, V_M$  the first  $k$  left and right singular vectors of  $M$ , and by  $U_N, V_N$  those of  $N$ . Suppose there exists  $\alpha > 0$  such that*

$$\alpha \leq \min_{1 \leq i \leq k} \sigma_i - \max_{k+1 \leq r \leq n} \tilde{\sigma}_r.$$

Then

$$\max\{\|U_M - U_N\|_2, \|V_M - V_N\|_2\} \leq \frac{\|M - N\|_2}{\alpha}.$$